PNAS RESEARCH ARTICLE | EARTH, ATMOSPHERIC, AND PLANETARY SCIENCES OPEN ACCESS

A new view on abrupt climate changes and the bipolar seesaw based on paleotemperatures from Iberian Margin sediments

Nina Davtian[a,1,2] and Edouard Bard[a,2]

Contributed by Edouard Bard; received June 2, 2022; accepted February 2, 2023; reviewed by Jerry F. McManus, Eelco J. Rohling, and Thomas F. Stocker

The last glacial cycle provides the opportunity to investigate large changes in the Atlantic Meridional Overturning Circulation (AMOC) beyond the small fluctuations evidenced from direct measurements. Paleotemperature records from Greenland and the North Atlantic show an abrupt variability, called Dansgaard–Oeschger (DO) events, which is associated with abrupt changes of the AMOC. These DO events also have Southern Hemisphere counterparts via the thermal bipolar seesaw, a concept describing the meridional heat transport leading to asynchronous temperature changes between both hemispheres. However, temperature records from the North Atlantic show more pronounced DO cooling events during massive releases of icebergs known as Heinrich (H) events, contrary to ice-core–based temperature records from Greenland. Here, we present high-resolution temperature records from the Iberian Margin and a Bipolar Seesaw Index to discriminate DO cooling events with and without H events. We show that the thermal bipolar seesaw model generates synthetic Southern Hemisphere temperature records that best resemble Antarctic temperature records when using temperature records from the Iberian Margin as inputs. Our data-model comparison emphasizes the role of the thermal bipolar seesaw in the abrupt temperature variability of both hemispheres with a clear enhancement during DO cooling events with H events, implying a relationship that is more complex than a simple flip-flop between two climate states linked to a tipping point threshold.

bipolar seesaw | abrupt climate changes | paleotemperature | paleoceanography

Significance

The evolution of the Atlantic Meridional Overturning Circulation remains difficult to constrain from direct measurements. During the last glacial cycle, the strength of this circulation covaried with temperature in the North Atlantic, itself connected to Southern Hemisphere temperature. However, this interhemispheric connection was mostly studied using Greenland and Antarctic ice cores, resulting in an incomplete picture of the thermal bipolar seesaw. Using new temperature records from the Iberian Margin, a new Bipolar Seesaw Index, and Southern Hemisphere temperature simulations, we discriminate Northern Hemisphere cold events with and without massive iceberg discharges into the North Atlantic. Our data-model comparison implies a relationship that is more complex than a simple flip-flop between two climate states linked to a tipping point threshold.

Evidence has been growing for systematic changes of the Atlantic Meridional Overturning Circulation (AMOC) over the past decades (1, 2). An AMOC decreasing shift may contribute to the "warming hole" observed in the surface temperature of the North Atlantic, a feature in data and model simulations that has been interpreted as a complex oceanic response to rising CO_2 in the atmosphere (2, 3). Projections based on numerical models show that AMOC weakening will continue to accompany global warming due to the forthcoming emissions of anthropogenic CO_2 (4). Nevertheless, the existence and amplitude of the long-term trend in recent observations remain a subject of debate due to large high-frequency AMOC variability (1, 5). In addition, the future evolution of the AMOC and its dependence on the overall amplitude and rapidity of future scenarios of anthropogenic forcing are still very uncertain (4, 6).

Geochemical studies of deep-sea cores have shown that the AMOC was particularly variable during the last glacial cycle, in apparent synchrony with the temperature record in the same North Atlantic sediments (7–12) and in Greenland ice cores (13, 14). Several cold events of the abrupt Dansgaard–Oeschger (DO) variations, named DO stadials (15–17), also correspond to massive releases of icebergs into the North Atlantic—Heinrich (H) events—as testified by layers of ice-rafted debris (IRD) found in deep-sea cores (14, 18). Indeed, the H and DO events provide the best record for studying large changes of the AMOC on time scales from decades to millennia.

Decades of work have strengthened the knowledge of H and DO variations in the North Atlantic and surrounding continents, including Greenland with its highly detailed paleotemperature records based on the water and gas isotopes measured in ice cores (Figs. 1 *A* and *B* and 2*A*; see *SI Appendix*, Text S1 for details). Nevertheless, there is an important contrast between the shapes of North Atlantic sea surface temperature (SST) and Greenland temperature records during some abrupt climate changes, namely the difference in relative amplitude of coolings during DO stadials with and without H events (19).

A clear illustration of the amplitude difference between Greenland and Atlantic records is provided by the youngest and best-known Heinrich event 1 (H1). Indeed, during H1 the oxygen isotope composition of ice—$\delta^{18}O_{ice}$, an index positively correlated with atmospheric temperature—is even higher than during other DO stadials and the last glacial cold spell called the Younger Dryas event, both in the GRIP and GISP2 Greenland Summit cores and in earlier cores from other sites such as Dye 3 and Camp Century (34, 35).

Author contributions: E.B. designed research; N.D. and E.B. performed research; N.D. analyzed data; and N.D. and E.B. wrote the paper.

Reviewers: J.F.M., Columbia University; E.J.R., Australian National University; and T.F.S., Universitat Bern.

The authors declare no competing interest.

Copyright © 2023 the Author(s). Published by PNAS. This open access article is distributed under Creative Commons Attribution-NonCommercial-NoDerivatives License 4.0 (CC BY-NC-ND).

[1]Present address: Institut de Ciència i Tecnologia Ambientals, Universitat Autònoma de Barcelona, Cerdanyola del Vallès, Barcelona 08193, Spain.

[2]To whom correspondence may be addressed. Email: Nina.Davtian@uab.cat or bard@cerege.fr.

This article contains supporting information online at https://www.pnas.org/lookup/suppl/doi:10.1073/pnas.2209558120/-/DCSupplemental.

Published March 13, 2023.

Downloaded from https://www.pnas.org by 86.216.178.75 on March 13, 2023 from IP address 86.216.178.75.

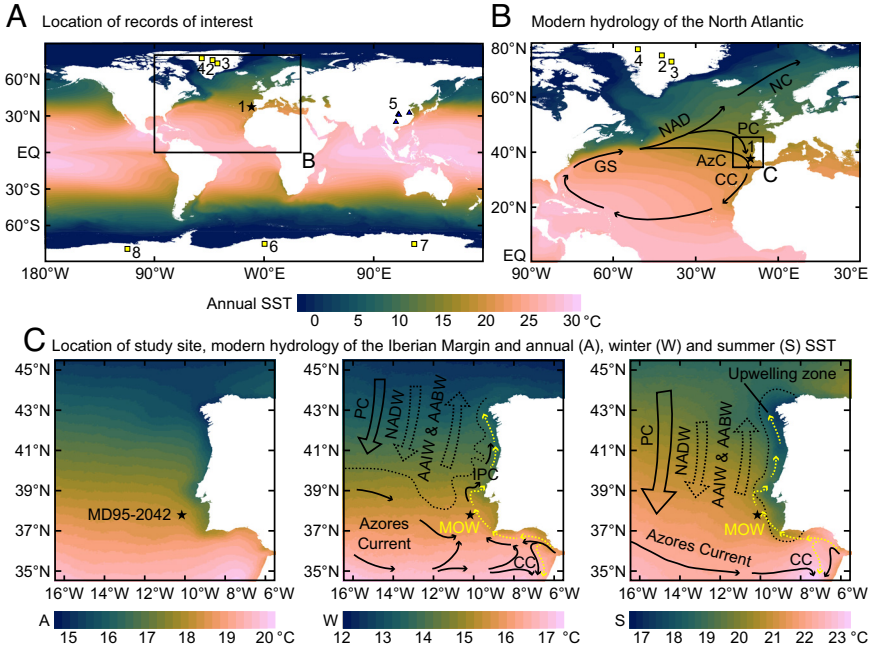

Fig. 1. Location and modern hydrology of the core MD95-2042 site in the Iberian Margin. (*A*) Location of records mentioned in the text. (1) Core MD95-2042, (2) NGRIP, (3) GISP2, (4) NEEM, (5) Chinese speleothems, (6) EDML, (7) EDC, and (8) WD. The Chinese speleothem records indicated are those compiled by ref. 20. (*B*) North Atlantic. (*C*) Iberian Margin and core MD95-2042. Solid arrows represent surface currents, whereas dotted arrows represent deep currents. GS, Gulf Stream; NAD, North Atlantic Drift; NC, Norwegian Current; PC, Portugal Current; AzC, Azores Current; CC, Canary Current; IPC, Iberian Poleward Current; MOW, Mediterranean Outflow Waters; NADW, North Atlantic Deep Waters; AAIW, Antarctic Intermediate Waters; and AABW, Antarctic Deep Waters. The colored SST gradients represent Pathfinder SST V5 climatology at 4-km resolution (21, 22). Modified from ref. 23.

Moreover, quantitative paleotemperature reconstructions based on $\delta^{15}N$ in Greenland ice confirm this lack of enhanced cooling during DO stadials with H events—named H stadials hereafter—when compared to other DO stadials (25) (Fig. 2*A*).

Previous modeling work indicates that Greenland may have been insulated from further cooling during H stadials due to a southward shift of North Atlantic Deep Water formation zones (36) and to the presence of sea ice surrounding Greenland (37–39). More recent modeling studies suggest that the lack of response in Greenland may be due to seasonal effects on the $\delta^{18}O_{ice}$ proxy (40). None of these effects are mutually exclusive and any of them could have acted in concert to bias the Greenland record but not the Iberian Margin record which has probably captured the true regional signal of the North Atlantic.

Numerical models perturbed by freshwater input into the North Atlantic have been used to mimic the massive iceberg release during H events (19, 36, 41–44). This usually leads to a strong AMOC decrease or even a collapse, with global impacts on surface temperatures, notably an intense cooling in the North Atlantic and surrounding continents and a moderate warming in the Southern Hemisphere. The robust behavior of these numerical models of varying complexity (19, 36, 41–44) has led to the notion of the thermal bipolar seesaw, which has been simplified as a thermal system that couples a southern heat reservoir with the Atlantic Ocean and which links both hemispheres (45).

The thermal bipolar seesaw model was used to study amplitude differences between paleotemperature records reconstructed from Greenland and Antarctic ice cores (46). This comparison led to the discovery of a one-to-one coupling between Antarctic warm events, named Antarctic Isotope Maximum (AIM) events, and Greenland cold events (30, 31, 47–51), with a strong correlation between the amplitude of Antarctic warmings (ΔT_s) and the duration of Greenland coolings (Δt_n) (30).

Nevertheless, the comparison between Greenland and Antarctic temperature records, by means of the ΔT_s versus Δt_n diagram and the thermal bipolar seesaw model, is not fully satisfactory because the northern component of the thermal seesaw should be represented with North Atlantic temperatures, rather than with those over Greenland, whose record is truncated during H stadials (Fig. 2*A*). Indeed, the sole use of the DO stadial duration (Δt_n) in the correlation diagram implicitly assumes that amplitude changes of northern DO stadials (ΔT_n) are negligible or irrelevant, which is not true for North Atlantic SST records (19). A possible impact of the enhanced cooling during H stadials on the thermal bipolar seesaw has been tested in several studies, but inconclusive and conflicting results were obtained (52–54).

In order to revisit this question, we reconstruct a North Atlantic SST record over the entire last glacial cycle by reanalyzing at high resolution the well-known core MD95-2042 from the Iberian Margin (see location in Fig. 1 and *Materials and Methods*) with the Ring Index of hydroxylated tetraethers with OH-GDGT-0 (RI-OH′) paleothermometric proxy (Fig. 2*B*), in comparison with the unsaturation index of alkenones (U^{K}_{37}) record (Fig. 2*C*) measured in the very same samples (*Materials and Methods*) and the ice-volume–corrected planktic foraminiferal $\delta^{18}O$ record (*SI Appendix*, Fig. S1*B*)—see *SI Appendix*, Text S1 and Figs. S1 and S2 for details and motivations concerning our selection of Iberian Margin SST records. We also update the chronology of core MD95-2042 by considering the most recent geochronological improvements over the last glacial cycle—e.g., the IntCal20 calibration over the ^{14}C range (55) (*SI Appendix*, Table S1 and *Materials and Methods*).

Our study follows two complementary approaches. First, our SST records from the Iberian Margin have a temporal resolution suitable for the detection of H and DO stadials and for use as input curves for the thermal bipolar seesaw model, in complement to Greenland ice-core records. We thus revisit the classical ΔT_s versus Δt_n diagram and the thermal bipolar seesaw model using better-dated and better-resolved SST records from the

Downloaded from https://www.pnas.org by 86.216.178.75 on March 13, 2023 from IP address 86.216.178.75.

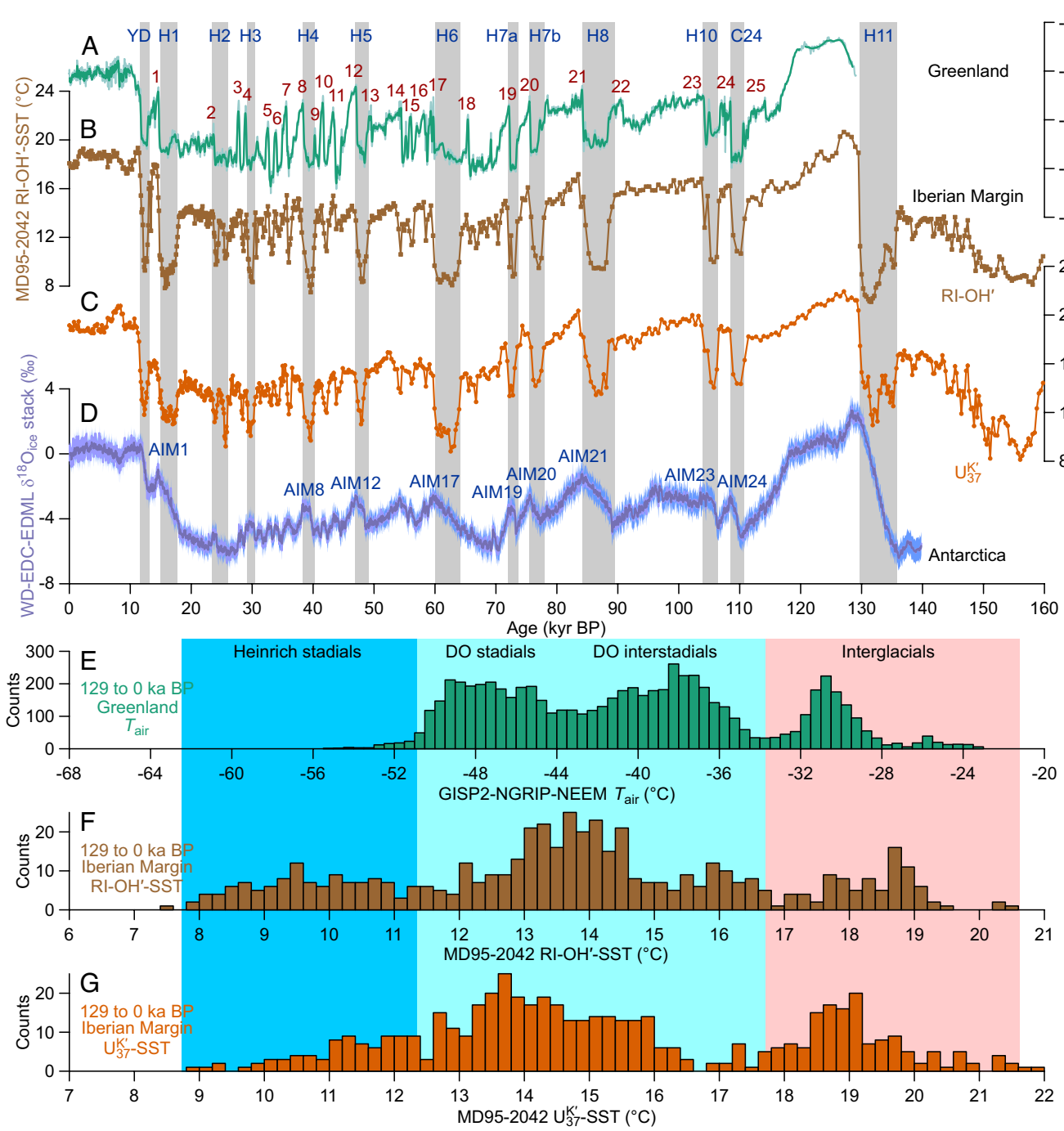

Fig. 2. The separation between Heinrich stadials and other Dansgaard–Oeschger stadials during the last climatic cycle. (*A*) Greenland T_{air} records from the GISP2 (24), NGRIP (25), and NEEM (26) ice cores. NEEM T_{air} values were obtained by adding –31 °C to published anomalies. (*B*) RI-OH′-SST record from core MD95-2042 (*Materials and Methods*; partly published in ref. 23). (*C*) $U^{K'}_{37}$-SST record from core MD95-2042 (23, 27). See also *Materials and Methods*. (*D*) Antarctic stack of the $\delta^{18}O_{ice}$ records from EDC (28, 29), EDML (28, 30), and WD (31–33) over the 140 to 0 ka BP period with its 2σ confidence interval (CI) (*Materials and Methods*). See Fig. 1 for record locations and *Materials and Methods* for chronologies. (*E*–*G*) Histograms of Greenland T_{air} and core MD95-2042 RI-OH′-SST and $U^{K'}_{37}$-SST values, respectively, over the 129 to 0 ka BP period. For the GISP2 portion of the Greenland T_{air} record, subsampled 10-point averages were used instead of published values to limit overrepresentation of the Holocene. Gray bars with labels in *A*–*D* indicate the Younger Dryas and Heinrich and Heinrich-like stadials. Numbers in *A* indicate Dansgaard–Oeschger events. Labels in *D* indicate Antarctic Isotope Maximum events occurring during Heinrich and Heinrich-like stadials.

Iberian Margin and paleothermometric records from ice cores in Greenland and Antarctica. Second, we revisit relationships between DO stadials and AIM events by considering two Southern versus Northern Hemisphere diagrams extended from the classical ΔT_s versus Δt_n diagram. This extension allows us to introduce a climatic index useful to differentiate and highlight the thermal bipolar seesaw impact for different types of DO stadials.

Results and Discussion

Iberian Margin RI-OH′ SST Record from Core MD95-2042. Core MD95-2042 (37°45′N, 10°10′W, 3,146 m water depth; Fig. 1) was retrieved from the distal part of the Iberian Margin continental slope during the IMAGES I (1995) cruise of R/V Marion Dufresne using a Calypso corer. The coring site was chosen to replicate and extend the shorter piston core SU8118 (37°46′N, 10°11′W, 3,135 m water

Downloaded from https://www.pnas.org by 86.216.178.75 on March 13, 2023 from IP address 86.216.178.75.

depth) used in previous studies (56, 57). The core MD95-2042 site is located at the edge of the upwelling area, roughly 150 km from the modern coastline—see *SI Appendix*, Text S1 for details on the environmental context. The sediment core is 3,140 cm long, covers the last 160 ky, and mainly consists of calcareous silty clay. Here, we extend the core MD95-2042 tetraether-based records acquired by ref. 23, including the RI-OH′ record on which we focus so that they cover the last 160 ky (*Materials and Methods*).

Our Iberian Margin RI-OH′ SST record faithfully shows DO events with contrasting cooling amplitudes between H stadials and other DO stadials (Fig. 2*B*), independently from established SST proxies such as $U^{K'}_{37}$—see *SI Appendix*, Text S2 and Figs. S3–S5 for a discussion on the independence of RI-OH′ as an SST proxy. Contrary to the Greenland atmospheric temperature (T_{air}) record (Fig. 2 *A* and *E*), the Iberian Margin RI-OH′ record gives cooler SSTs during H stadials than during other DO stadials (Fig. 2 *B* and *F*), as is the case for the Iberian Margin $U^{K'}_{37}$ record from the same core (Fig. 2 *C* and *G*). These patterns further strengthen a previous validation of RI-OH′ as an SST proxy in the Iberian Margin (23). The increased temporal resolution of the biomarker-based Iberian Margin SST records and their faithful capture of enhanced cooling during H stadials thus support further analysis of the thermal bipolar seesaw using these Iberian Margin SST records, including the RI-OH′ SST record.

General Approach. We group DO stadials into three categories for all studied Southern versus Northern hemisphere diagrams: 1) H stadials with an IRD layer in core MD95-2042 and other North Atlantic sediments, 2) H stadials without an IRD layer in core MD95-2042 sediments, named H-like events by ref. 58 and H-like stadials hereafter, and 3) other DO stadials. We provide further details on the nomenclature in *Materials and Methods*.

We essentially compare SST records from the Iberian Margin with ice-core paleothermometric records from Antarctica to revisit the thermal bipolar seesaw—we also consider and discuss SST records from the Southern Ocean in *SI Appendix*, Text S3 and Fig. S6. In parallel, we compare ice-core records from Greenland and Antarctica (*Materials and Methods*). We mainly use normalized temperature records expressed in unit standard deviation (SD) over the 129 to 0 thousand years before present (ka BP, where 0 ka BP is 1950 CE) period (*Materials and Methods*)—see *SI Appendix*, Text S5 and Fig. S10 for a test using nonnormalized temperature records and other motivations of our temperature record normalizations. We thus focus on the shapes of temperature records, i.e., relative changes rather than actual temperature values, which depend on uncertain calibrations for the various proxies (23, 25, 59, 60). Our analysis thus relies on the assumption of monotonous proxy-temperature relationships.

For all studied Southern versus Northern hemisphere diagrams, we calculate Pearson's *r* coefficients for comparison with previous thermal bipolar seesaw studies (30, 47, 48, 54) and Kendall's τ rank coefficients for robust correlation tests, notably for nonnormally distributed input values. We use the 95% level—$P < 0.05$—as the significance criterion for interhemispheric relationships. We follow a Monte Carlo method modified from ref. 54 to assess the influence of nonsystematic temperature uncertainties on our results (*Materials and Methods*)—we do not include chronological uncertainties, given their multiple and archive-dependent sources, as discussed in detail in *SI Appendix*, Text S6. We also follow a bootstrapping method to compare absolute correlation coefficient values between Greenland and Iberian Margin temperature records as Northern Hemisphere components (*Materials and Methods*).

For all applications of the thermal bipolar seesaw model (*Materials and Methods*, ref. 46), we use three goodness-of-fit metrics for model versus data comparisons: Pearson's *r* coefficient for comparison with previous thermal bipolar seesaw studies (46, 52), Kendall's τ rank coefficient for robust correlation tests, notably for input values with nonnormal distributions, and mean squared error (MSE) to take advantage of residuals with normal distributions. We express the records in unit SD over the 115 to 12 ka BP period to concentrate on the shape of changes, as for Southern versus Northern Hemisphere diagrams. Similarly, we assess the influence of nonsystematic temperature uncertainties on model versus data comparisons using a Monte Carlo method modified from ref. 54 without chronological uncertainties for simplicity (*Materials and Methods* and *SI Appendix*, Text S6). We outline all statistical and uncertainty results from this study in *SI Appendix*, Table S2.

Classical Southern versus Northern Hemisphere Diagram. We reevaluate the classical ΔT_s versus Δt_n relationship between DO stadials and AIM events using our Iberian Margin RI-OH′ SST record as the Northern Hemisphere component and a $\delta^{18}O_{ice}$ stack from Antarctic ice cores as the Southern Hemisphere component (*Materials and Methods*)—see *SI Appendix*, Table S3 for results from other Southern and Northern Hemisphere paleothermometric records. Our Antarctic $\delta^{18}O_{ice}$ stack and Iberian Margin RI-OH′ SST record give a strong ΔT_s versus Δt_n relationship when all Dansgaard–Oeschger stadial-Antarctic Isotope Maximum (DO-AIM) pairs are considered—$r = 0.73$ and $\tau = 0.51$, $P < 0.001$ for both correlation tests (Fig. 3*A*; see also *SI Appendix*, Text S7 and Tables S4, S5, and S15 for comparisons of classical ΔT_s versus Δt_n relationships). Most DO-AIM pairs follow a linear ΔT_s versus Δt_n relationship close to a regression line through the origin which considers errors in both coordinates (Fig. 3*A*)—the thermal bipolar seesaw model (46) motivates regression lines with intercepts forced to 0 for all Southern versus Northern Hemisphere diagrams.

We assess how well DO-AIM pairs follow our linear ΔT_s versus Δt_n relationship. The DO-AIM pairs 2b and 18 deviate from our linear ΔT_s versus Δt_n relationship (Fig. 3*A*), similarly to the DO-AIM pairs 2 and 18 in ref. 48 which deviate from the original ΔT_s versus Δt_n relationship by ref. 30—ref. 48 did not include the DO-AIM pairs 14 and 17 which deviate from our linear ΔT_s versus Δt_n relationship (Fig. 3*A*). Conversely, the DO-AIM pair 21 follows our linear ΔT_s versus Δt_n relationship (Fig. 3*A*), contrary to the same DO-AIM pair in refs. 47 and 48 which deviates from the original ΔT_s versus Δt_n relationship by ref. 30. Yet, the DO-AIM pair 21 deviates from most other DO-AIM pairs when considering the Greenland record rather than our Iberian Margin record (*SI Appendix*, Fig. S11). Similarly, our regression line misfits with most DO-AIM pairs when considering the Greenland record rather than our Iberian Margin record, although the DO-AIM pair 21 deviates little from our regression line in both cases (*SI Appendix*, Fig. S11). While the linear regression in ref. 30—established using the ordinary least squares method—captures most DO-AIM pairs in refs. 47 and 48, our regression method better supports the linear ΔT_s versus Δt_n relationship when considering our Iberian Margin record than when considering the Greenland record (Fig. 3*A* and *SI Appendix*, Fig. S11). Therefore, our Iberian Margin SST record provides a stronger confirmation of the thermal bipolar seesaw than does the Greenland T_{air} record.

Thermal Bipolar Seesaw Model Simulations. We use both biomarker-based Iberian Margin SST records (RI-OH′ and $U^{K'}_{37}$) and the Greenland T_{air} (25) and $\delta^{18}O_{ice}$ (13) records as inputs for the thermal bipolar seesaw model (*Materials and Methods*, ref.

Downloaded from https://www.pnas.org by 86.216.178.75 on March 13, 2023 from IP address 86.216.178.75.

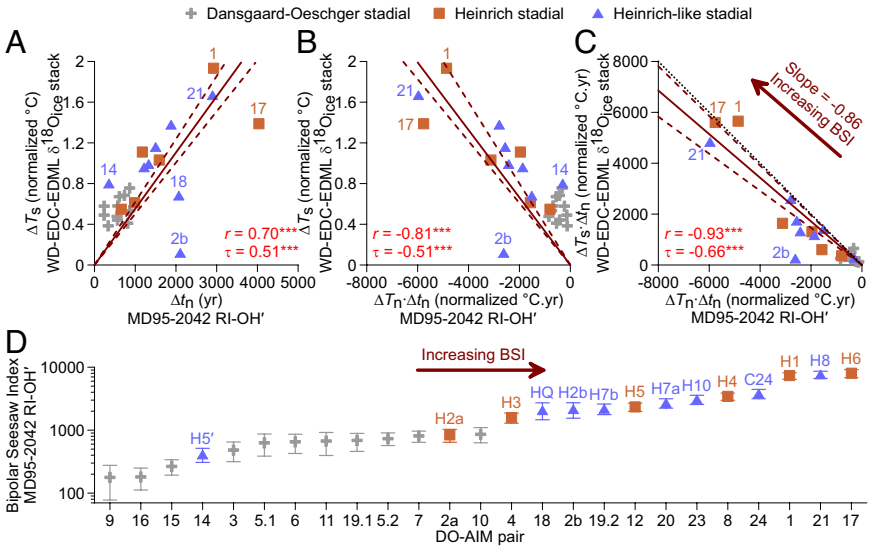

Fig. 3. The relationship between Southern and Northern Hemisphere climate events from the perspective of the Iberian Margin RI-OH′ SST record. (*A*) Classical ΔT_s versus Δt_n diagram. (*B*) Extended ΔT_s versus $\Delta T_n \bullet \Delta t_n$ diagram. (*C*) Extended $\Delta T_s \bullet \Delta t_n$ versus $\Delta T_n \bullet \Delta t_n$ diagram (*Materials and Methods*). Only the end-member scenario that best depicts the thermal bipolar seesaw (Scenario 1; see *SI Appendix*, Text S8) is shown here. The Southern Hemisphere record used in all cases is an Antarctic stack of the $\delta^{18}O_{ice}$ records from EDC (28, 29), EDML (28, 30), and WD (31–33) over the 140 to 0 ka BP period (*Materials and Methods*). Both Southern and Northern Hemisphere have been centered to zero means and normalized to unit SDs over the 129 to 0 ka BP period. Labels indicate a few Dansgaard–Oeschger stadial-Antarctic Isotope Maximum (DO-AIM) pairs, as per refs. 30, 47, and 48—see *SI Appendix*, Fig. S11 for the identification of all DO-AIM pairs. Antarctic Isotope Maximum events with Heinrich and Heinrich-like stadials are distinguished from Antarctic Isotope Maximum events with other Dansgaard–Oeschger stadials. Solid lines represent regression lines with intercepts forced to 0 and which considers errors in both coordinates (*Materials and Methods*). Dashed lines represent 95% CIs of regression slopes from 1,000 Monte Carlo iterations (*Materials and Methods*). The dotted line in *C* represents the –1:1 line. For the sake of readability, error bars for individual data points in *A*–*C* are omitted here and shown in *SI Appendix*, Fig. S12. Pearson's *r* coefficients and Kendall's τ rank coefficients are also shown in *A*–*C*, with their 99.9% significance levels coded as ***. (*D*) Bipolar Seesaw Index (BSI) values (*Materials and Methods*). Given the wide amplitude between the highest and lowest BSI values, the *y* axis has a logarithmic scale. Each DO-AIM pair has the same symbol as in *A*–*C*. Colored labels indicate Heinrich and Heinrich-like stadials.

46). We then compare each bipolar seesaw output (BSO) using our Antarctic $\delta^{18}O_{ice}$ stack as the Southern Hemisphere reference record (*SI Appendix*, Texts S10–S13). To circumvent uncertainties due to partially independent ice-core and core MD95-2042 chronologies—see *SI Appendix*, Text S6 for details—we also compare the BSOs from the three Iberian Margin SST records (RI-OH′, $U^{K'}_{37}$, and ice-volume–corrected planktic foraminiferal $\delta^{18}O$) with the ice-volume–corrected benthic foraminiferal $\delta^{18}O$ record from the same Iberian Margin sediment core—see *SI Appendix*, Text S14 for details.

All BSO records for the 115 to 12 ka BP period are visually and statistically in good agreement with the Southern Hemisphere reference record (Fig. 4*A* and *SI Appendix*, Table S16)—e.g., *r* values between 0.52 and 0.63 and τ values between 0.33 and 0.44 over the 115 to 12 ka BP period (*SI Appendix*, Table S16). Visually, the BSOs from Iberian Margin SST records also better

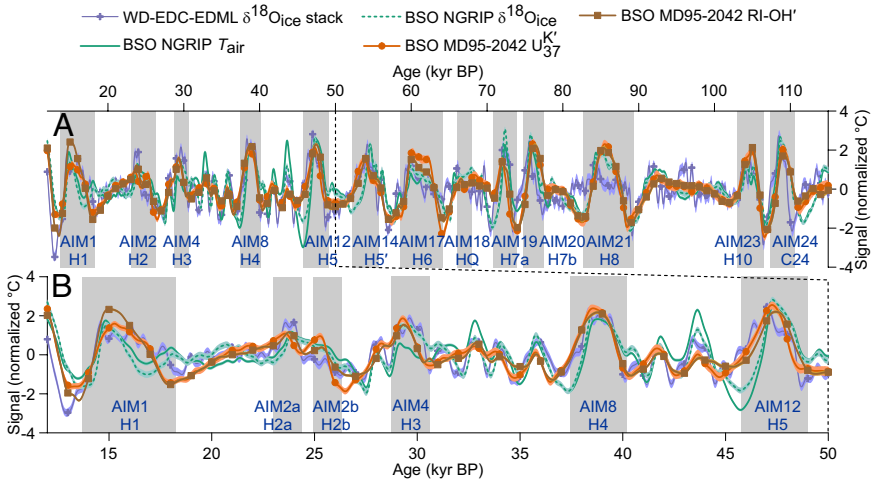

Fig. 4. Comparison between bipolar seesaw model outputs from several Northern Hemisphere temperature records and a Southern Hemisphere reference record. (*A*) 115- to 12-ka BP period using a band-pass filter with a 500- to 10,000-y window. (*B*) Close up of the 50- to 12-ka BP period. Each bipolar seesaw output (BSO) and reference record has been centered to zero means and normalized to unit SDs over the 115 to 12 ka BP period in *A* and over the 50 to 12 ka BP period in *B* to facilitate the comparison (*Materials and Methods*). Shading around BSO and reference records in both *A* and *B* represents their 95% CIs from 1,000 Monte Carlo iterations (*Materials and Methods*). The Southern Hemisphere reference record is an Antarctic stack of the $\delta^{18}O_{ice}$ records from EDC (28, 29), EDML (28, 30), and WD (31–33) over the 140 to 0 ka BP period (*Materials and Methods*). Gray bars with labels indicate Antarctic Isotope Maximum events with Heinrich and Heinrich-like stadials.

Downloaded from https://www.pnas.org by 86.216.178.75 on March 13, 2023 from IP address 86.216.178.75.

agree with the Southern Hemisphere reference record than do the BSOs from Greenland paleothermometric records, especially for the second half of the last glacial cycle (Fig. 4*B*). Indeed, Iberian Margin BSOs mostly show significantly better fits (Pearson's r, Kendall's τ, and MSE) than Greenland BSOs do at the 95% level (*SI Appendix*, Fig. S13, Table S17, and Text S11).

Reference SST records for the North Atlantic are based on $U^{K'}_{37}$, the most established organic paleothermometer off the southern Iberian Margin (23, 27, 57, 61, 62) (Fig. 2*C*). The recent RI-OH′ organic paleothermometer further confirms that the southern Iberian Margin is an ideal place to investigate North Atlantic SSTs (23) (Fig. 2*B*). The BSO from the RI-OH′ record even has some significantly better agreements with the Southern Hemisphere reference record than does the BSO from the $U^{K'}_{37}$ record at the 95% level (*SI Appendix*, Table S17).

The Iberian Margin SST records generate Southern Hemisphere temperature simulations that are in good agreement with the Antarctic record—e.g., r values of 0.59 and 0.63 and τ values of 0.42 and 0.44 over the 115 to 12 ka BP period (*SI Appendix*, Table S16). Indeed, the BSOs from both biomarker-based Iberian Margin SST records show particularly strong AIM amplitudes during H6 to H3 and H1 as well as during H-like stadials such as C24, H10, and H8 (58), which is not the case for the BSOs from both Greenland paleothermometric records (Fig. 4). Despite their better resolutions compared with the Iberian Margin SST records (Fig. 2 *A*–*C*), the Greenland T_{air} and $\delta^{18}O_{ice}$ records do not generate better Southern Hemisphere temperature simulations (Fig. 4 and *SI Appendix*, Fig. S13 and Table S17). Discrepancies between the Southern Hemisphere reference record and BSOs from Greenland records occur, for instance, at ca. 112, 94, and 57 ka BP and during H5 to H3 and H1 (Fig. 4).

We then jointly use the classical ΔT_s versus Δt_n diagram and synthetic Southern Hemisphere records generated by forcing the thermal bipolar seesaw model with biomarker-based Iberian Margin SST records and Greenland T_{air} and $\delta^{18}O_{ice}$ records (*SI Appendix*, Tables S7–S14). Contrary to observed temperature records, filtered and simulated temperature records give typically weak to nonsignificant ΔT_s versus Δt_n relationships, except when using Southern Hemisphere temperature records simulated from the Iberian Margin SST records (*SI Appendix*, Tables S7 and S11). Furthermore, Southern Hemisphere temperature records simulated from the Greenland paleothermometric records systematically give weak and nonsignificant ΔT_s versus Δt_n relationships—r values between 0.10 and 0.30 and τ values between 0.16 and 0.27—whereas Southern Hemisphere temperature records simulated from the Iberian Margin SST records systematically give moderate-to-strong and significant ΔT_s versus Δt_n relationships—r values between 0.48 and 0.74 and τ values between 0.38 and 0.55 ($P < 0.02$ for all correlation tests; *SI Appendix*, Tables S7 and S11). Overall, our combined use of classical ΔT_s versus Δt_n diagrams with the thermal bipolar seesaw model further supports the relevance of North Atlantic SST records such as those from the Iberian Margin to study the thermal bipolar seesaw, in conjunction with Greenland and Antarctic ice-core paleothermometric records.

Extended Southern versus Northern Hemisphere Diagrams. We propose two extensions of the classical ΔT_s versus Δt_n diagram to consider the contrasting cooling amplitudes (ΔT_n) between H stadials and other DO stadials for Iberian Margin SST records, namely the ΔT_s versus $\Delta T_n \cdot \Delta t_n$ and $\Delta T_s \cdot \Delta t_n$ versus $\Delta T_n \cdot \Delta t_n$ diagrams. Like the classical ΔT_s versus Δt_n diagram, our extended ΔT_s versus $\Delta T_n \cdot \Delta t_n$ diagram relies on the physical basis of the thermal bipolar seesaw for which an approximation links ΔT_s, ΔT_n, and Δt_n:

$$\Delta T_s \approx \left(\frac{\Delta T_n}{2T} \right) \cdot \Delta t_n, \quad [1]$$

with T the time characteristic of the heat reservoir involved in the thermal bipolar seesaw model (46)—Equation 1 is Equation 9.5 on page 162 in ref. 63. This approximation implies that a linear correlation is expected in the ΔT_s versus Δt_n space, only if the term in parenthesis (ΔT_n/2T) is broadly constant. This is justified for Greenland and is the reason for the strong linear dependence described in ref. 30. However, Eq. **1** clearly illustrates that the Southern Hemisphere warming also depends on the overall cooling ΔT_n in the Northern Hemisphere, which is variable in North Atlantic SST records (19) by contrast to Greenland temperature records. The elegance of the extended ΔT_s versus $\Delta T_n \cdot \Delta t_n$ diagram is that the relationship linking ΔT_s, and $\Delta T_n \cdot \Delta t_n$ depends solely on 1/2T rather than on ΔT_n/2T for the classical ΔT_s versus Δt_n diagram.

In addition, we calculate the $\Delta T_n \cdot \Delta t_n$ product that would be proportional to the accumulated heat loss within the Northern Hemisphere during the time Δt_n when the AMOC is weaker. Similarly, the $\Delta T_s \cdot \Delta t_n$ product would be proportional to the accumulated heat gain within the Southern Hemisphere during the time Δt_n when the AMOC is weaker. This justifies the use of our second extended diagram, $\Delta T_s \cdot \Delta t_n$ versus $\Delta T_n \cdot \Delta t_n$ representative of the heat exchange between both hemispheres. We provide a more detailed physical basis and motivation of our extended ΔT_s versus $\Delta T_n \cdot \Delta t_n$ and $\Delta T_s \cdot \Delta t_n$ versus $\Delta T_n \cdot \Delta t_n$ diagrams in *SI Appendix*, Text S4 and Figs. S7–S10.

We use our Iberian Margin RI-OH′ SST record as the Northern Hemisphere component and our Antarctic $\delta^{18}O_{ice}$ stack as the Southern Hemisphere component (*Materials and Methods*) to evaluate ΔT_s versus $\Delta T_n \cdot \Delta t_n$ and $\Delta T_s \cdot \Delta t_n$ versus $\Delta T_n \cdot \Delta t_n$ relationships between DO stadials and AIM events—see *SI Appendix*, Table S3 for results from other Southern and Northern Hemisphere paleothermometric records. Our Antarctic $\delta^{18}O_{ice}$ stack and our Iberian Margin RI-OH′ SST record give strong ΔT_s versus $\Delta T_n \cdot \Delta t_n$ and $\Delta T_s \cdot \Delta t_n$ versus $\Delta T_n \cdot \Delta t_n$ relationships when all DO-AIM pairs are considered—$r = -0.81$ and $\tau = -0.51$ for ΔT_s versus $\Delta T_n \cdot \Delta t_n$ diagrams (Fig. 3*B*), and $r = -0.93$ and $\tau = -0.66$ for $\Delta T_s \cdot \Delta t_n$ versus $\Delta T_n \cdot \Delta t_n$ diagrams (Fig. 3*C*), $P < 0.001$ for all correlation tests.

Our extended $\Delta T_s \cdot \Delta t_n$ versus $\Delta T_n \cdot \Delta t_n$ diagram shows the strongest relationship, not only for our Antarctic $\delta^{18}O_{ice}$ stack paired with our Iberian Margin RI-OH′ SST record (Fig. 3) but also for all other pairs of Southern and Northern Hemisphere paleothermometric records (*SI Appendix*, Fig. S11 and Table S3). These correlation results are coherent with those obtained from idealized Antarctic and Iberian Margin temperature records—see *SI Appendix*, Text S4 for details. Most DO-AIM pairs follow linear relationships close to regression lines through the origin which consider error in both coordinates for our extended ΔT_s versus $\Delta T_n \cdot \Delta t_n$ and $\Delta T_s \cdot \Delta t_n$ versus $\Delta T_n \cdot \Delta t_n$ diagrams (Fig. 3 *B* and *C*). While the classical ΔT_s versus Δt_n diagram and our extended ΔT_s versus $\Delta T_n \cdot \Delta t_n$ diagram show linear relationships that involve the time characteristic of the heat reservoir, our extended $\Delta T_s \cdot \Delta t_n$ versus $\Delta T_n \cdot \Delta t_n$ diagram gives regression slopes that would reflect the heat distribution between both hemispheres—see *SI Appendix*, Text S9 for interpretations of the $\Delta T_s \cdot \Delta t_n$ versus $\Delta T_n \cdot \Delta t_n$ slopes and a test with AIM warming areas integrated from cyclic and idealized Southern Hemisphere temperature records.

Downloaded from https://www.pnas.org by 86.216.178.75 on March 13, 2023 from IP address 86.216.178.75.

Our extended ΔT_s versus $\Delta T_n \cdot \Delta t_n$ and $\Delta T_s \cdot \Delta t_n$ versus $\Delta T_n \cdot \Delta t_n$ diagrams only have a few DO-AIM pairs that prominently deviate from the linear relationships, notably the DO-AIM pair 2b (Fig. 3 *B* and *C* and *SI Appendix*, Fig. S11). This systematic deviation is due to our use of similar DO stadial 2b delimitations for all Northern Hemisphere paleothermometric records, as H2b has a much shorter duration in the Iberian Margin than DO stadial 2b in Greenland (*SI Appendix*, Fig. S14). Accordingly, the DO-AIM pair 2b would be closer to the DO-AIM pair 2a for the Iberian Margin, notably our RI-OH′ SST record which has similar DO coolings for both H2 subevents. The DO-AIM pair 18 still deviates from linear ΔT_s versus $\Delta T_n \cdot \Delta t_n$ and $\Delta T_s \cdot \Delta t_n$ versus $\Delta T_n \cdot \Delta t_n$ relationships when considering Greenland rather than the Iberian Margin (*SI Appendix*, Fig. S11). Despite these few deviations, our extended ΔT_s versus $\Delta T_n \cdot \Delta t_n$ and $\Delta T_s \cdot \Delta t_n$ versus $\Delta T_n \cdot \Delta t_n$ diagrams are relevant for studying the thermal bipolar seesaw, notably using paleothermometric records with contrasting cooling amplitudes between H stadials and other DO stadials such as Iberian Margin SST records.

Our joint use of extended Southern versus Northern Hemisphere diagrams and synthetic Southern Hemisphere records generated by forcing the thermal bipolar seesaw model with biomarker-based Iberian Margin SST records and Greenland T_{air} and $\delta^{18}O_{ice}$ records (*SI Appendix*, Tables S7–S14) reveals typically weak to nonsignificant ΔT_s versus $\Delta T_s \cdot \Delta t_n$ relationships, except when using Southern Hemisphere temperature records simulated from the Iberian Margin SST records (*SI Appendix*, Tables S7 and S11). Our extended ΔT_s versus $\Delta T_s \cdot \Delta t_n$ diagram also shows stronger relationships when using Southern Hemisphere temperature records simulated from the Iberian Margin SST records than when using those simulated from the Greenland paleothermometric records (*SI Appendix*, Tables S7 and S11). Conversely, our extended $\Delta T_s \cdot \Delta t_n$ versus $\Delta T_n \cdot \Delta t_n$ diagram systematically shows strong and significant relationships when using filtered and simulated temperature records—r values between –0.69 and –0.97 and τ values between –0.46 and –0.88 ($P < 0.001$ for almost all correlation tests under both end-member scenarios; *SI Appendix*, Text S8 and Tables S7 and S11). Overall, our combined use of Southern versus Northern Hemisphere diagrams with the thermal bipolar seesaw model further supports the relevance of our extended ΔT_s versus $\Delta T_n \cdot \Delta t_n$ and $\Delta T_s \cdot \Delta t_n$ versus $\Delta T_n \cdot \Delta t_n$ diagrams to study the thermal bipolar seesaw using North Atlantic SST records and Greenland and Antarctic ice-core paleothermometric records, in conjunction with the classical ΔT_s versus Δt_n diagram.

Interhemispheric Relationships for Restricted Populations of DO-AIM Pairs. We only use our extended $\Delta T_s \cdot \Delta t_n$ versus $\Delta T_n \cdot \Delta t_n$ diagram for statistical analyses restricted to populations of DO-AIM pairs, given the typical losses of significance at the 95% level for the other Southern versus Northern Hemisphere diagrams due to reduced numbers of events (*SI Appendix*, Tables S6, S10, and S14). When considering the population of H and H-like stadials, most $\Delta T_s \cdot \Delta t_n$ versus $\Delta T_n \cdot \Delta t_n$ relationships remain strong and significant at the 95% level, despite the reduced dynamic range in the restricted population. However, $\Delta T_s \cdot \Delta t_n$ versus $\Delta T_n \cdot \Delta t_n$ relationships are less robust to restrictions to the population of other DO stadials, given the more frequent losses of significance at the 95% level (*SI Appendix*, Tables S6, S10, and S14). This contrast in losses of significance is likely due to the contrasting thermal bipolar seesaw responses between H and H-like stadials and other DO stadials. Overall, our statistical analysis for restricted populations of DO-AIM pairs may support the existence of at least three glacial modes (64) or even continuous thermal bipolar seesaw responses scaled to the forcing during H stadials.

Bipolar Seesaw Index (BSI). Our Iberian Margin RI-OH′ SST record provides a clear illustration of the relevance of our extended $\Delta T_s \cdot \Delta t_n$ versus $\Delta T_n \cdot \Delta t_n$ diagram—r value of –0.93 and τ value of –0.66—in parallel with the strong relationships in ΔT_s versus Δt_n and ΔT_s versus $\Delta T_n \cdot \Delta t_n$ diagrams—r values of 0.70 and –0.81 and τ values of 0.51 and –0.51 (Fig. 3 *A*–*C*). We therefore use our extended $\Delta T_s \cdot \Delta t_n$ versus $\Delta T_n \cdot \Delta t_n$ diagram based on the Iberian Margin RI-OH′ record to derive a climatic index, providing values for each DO-AIM pair (Fig. 3*D* and *Materials and Methods*).

We propose a Bipolar Seesaw Index (BSI) to complement the $\Delta T_s \cdot \Delta t_n$ versus $\Delta T_n \cdot \Delta t_n$ diagram (Fig. 3 *C* and *D*). Our BSI is defined for each DO-AIM pair as being the distance along the regression line from the origin (arrows on Fig. 3 *C* and *D*; see exact definition in *Materials and Methods*). Therefore, the BSI depends on both the northern climate event and its southern response. While we could also derive the BSI from the classical ΔT_s versus Δt_n diagram—or the extended ΔT_s versus $\Delta T_n \cdot \Delta t_n$ diagram—based on core MD95-2042 to differentiate H and H-like stadials from other DO stadials, the resulting BSI values would simply mirror Δt_n values expressed in y—or $\Delta T_n \cdot \Delta t_n$ values expressed in normalized °C.y. In addition, BSI values from the classical ΔT_s versus Δt_n diagram based on Greenland ice cores would suggest a single stadial climate state.

As shown in Fig. 3*D* for our Iberian Margin RI-OH′ and Antarctic $\delta^{18}O_{ice}$ stack records, BSI values vary between 841 and 8,023 for H stadials, between 411 and 7,679 for H-like stadials, and between 178 and 859 for other DO stadials. The BSI clearly differentiates H and H-like stadials, including HQ (12, 65) and H5′ (66), from other DO stadials. However, ranges in BSI values overlap for DO stadials with H stadials and DO stadials with H-like stadials, so the BSI cannot fully predict the presence or absence of an IRD layer in core MD95-2042 sediments. H6 has the largest BSI value (8,023), followed by H8 (7,679) and H1 (7,373; Fig. 3*D*). While H8 is an H-like stadial rather than an H stadial off the southern Iberian Margin, given the absence of an IRD layer (58), it has one of the most pronounced peaks in magnetic specific susceptibility as an IRD indicator in core MD95-2042 (67, 68). H8 is also characterized by very low biomarker concentrations in core MD95-2042 (23, 61), likely due to the cessation of seasonal upwelling, as is the case for other H and H-like stadials (61). Furthermore, H8 is linked to one of the most prominent Southern Hemisphere responses (AIM21). By contrast, H2a (841) and H5′ (411) are the only H and H-like stadials with smaller BSI values than DO10, which is the normal DO stadial with the largest BSI value (859; Fig. 3*D*). This overlap may be linked to the short durations of these H-like events and the small warming amplitudes of the associated AIM events. When considering uncertainties in BSI values, as well as the site and proxy dependencies of BSI values, our BSI may further support the existence of at least three climate states during the glacial (64) or even a continuum of thermal bipolar seesaw responses.

Conclusions

Our complementary approaches based on the ΔT_s versus $\Delta T_n \cdot \Delta t_n$ and $\Delta T_s \cdot \Delta t_n$ versus $\Delta T_n \cdot \Delta t_n$ diagrams and associated BSI, together with the comparison between observed and synthetic Antarctic records simulated with the thermal bipolar seesaw model, favor Iberian Margin SST records over Greenland temperature records for discriminating between responses linked to the thermal bipolar seesaw. This is a consequence of H and H-like stadials being severely truncated in Greenland (13, 25) (Fig. 2*A*) but not off the Iberian Margin (23, 27, 56, 57, 61, 62, 69) (Fig. 2 *B* and *C*). The extended sea ice cover and southward shift of AMOC convection

Downloaded from https://www.pnas.org by 86.216.178.75 on March 13, 2023 from IP address 86.216.178.75.

zones likely isolated Greenland, but not the Iberian Margin, from North Atlantic coolings (36–39, 70).

Our data-model comparison clearly shows the importance of the North Atlantic conditions in defining the Southern Ocean response. The fact that the amplitude of the southern response is also correlated to the northern cooling during H and H-like stadials (Fig. 3) implies that the climate system is more complex than a simple flip-flop between two constant states when a threshold is exceeded, suggesting multiple glacial modes or even a continuous response scaled to the forcing during H stadials. North Atlantic SST records should thus be considered in parallel with high-resolution glaciological records, in order to study the tipping points linked to AMOC in the ocean–atmosphere–ice system (71, 72). Indeed, the RI-OH′ and $U^{K'}_{37}$ paleothermometers complement each other for high-resolution SST reconstructions off the southern Iberian Margin. Our work suggests a richer dynamic than was previously thought, which has direct implications for our understanding of past and future climate changes associated with the AMOC and the thermal bipolar seesaw.

Materials and Methods

Biomarker Analysis in Core MD95-2042. We took one sediment sample every 5 cm from core MD95-2042, resulting in an average temporal resolution of roughly 250 y and 638 sediment samples for the last 160 ky. Alkenones and tetraethers were analyzed as described in ref. 23 and references therein. Importantly, the tetraether and alkenone fractions were purified from the same lipid extracts. To strengthen the reliability of tetraether quantifications despite drops in biomarker concentration during cold climatic events and Marine Isotope Stage 1 (27, 61), we doubled the injection volume for the duplicate analyses of the corresponding MD95-2042 samples not previously analyzed when compared to ref. 23.

We selected the homogenized core catcher sample from core MD95-2042 as an in-house standard sediment to verify the absence of instrumental drift, as per ref. 23. Throughout the new sample analyses, we conducted 20 additional replicate analyses of the same standard. We obtained the following SDs from these 20 replicates: 0.007 (0.37 °C) for RI-OH (Ring Index of hydroxylated tetraethers without OH-GDGT-0; introduced by ref. 73), 0.006 (0.14 °C) for RI-OH′ (Ring Index of hydroxylated tetraethers with OH-GDGT-0; introduced by ref. 73), and 0.004 (0.21 °C) for TEX_{86} (TetraEther indeX of GDGTs with 86 carbons; introduced by ref. 74). These SDs are similar to those previously obtained by ref. 23 and are much smaller than the proxy value changes during H and DO stadials (Fig. 2*B* and *SI Appendix*, Fig. S2 *B* and *C*).

Antarctic $\delta^{18}O_{ice}$ and T_{air} Stacks. Given the contrasting AIM shapes between Antarctic $\delta^{18}O_{ice}$ records (49, 70, 75), we used an Antarctic $\delta^{18}O_{ice}$ stack record rather than individual Antarctic $\delta^{18}O_{ice}$ records as the Southern Hemisphere reference record (Fig. 2*D*). To build the Antarctic $\delta^{18}O_{ice}$ stack record, we resampled every 10 y and then centered to zero means and normalized to unit SDs $\delta^{18}O_{ice}$ records from EDC (28, 29), EDML (28, 30), and WD (31–33) over the 140 to 0 ka BP period (see locations in Fig. 1)–the $\delta^{18}O_{ice}$ record from WD, which covers a shorter period than $\delta^{18}O_{ice}$ records from EDC and EDML, was centered to a zero mean and normalized to a unit SD over the 68 to 0 ka BP period. To optimize the continuity between the portions with and without the WD ice core, we shifted Antarctic $\delta^{18}O_{ice}$ records again so that they have zero means over the 68 to 67 ka BP period–the bottom of the WD ice core–before averaging them. We then obtained stacking uncertainties by calculating the pooled SD of the stacked Antarctic $\delta^{18}O_{ice}$ records divided by the square root of the number of stacked Antarctic $\delta^{18}O_{ice}$ records, following ref. 76. To obtain the record plotted in Fig. 2*D* with its 2σ confidence interval (CI), we rescaled the stack with the SD of the $\delta^{18}O_{ice}$ record from EDML over the 140 to 0 ka BP period, expressed in ‰ and then shifted the stack so that its mean value over the 1 to 0 ka BP period is 0. Even if $\delta^{18}O_{ice}$ records reflect not only T_{air} but also the moisture source, the $\delta^{18}O$ of seawater, seasonality, and ice-sheet elevation changes among other factors, $\delta^{18}O_{ice}$ and T_{air} have an almost linear relationship in Antarctica (28, 77–80). In addition, single and dual isotope approaches generally produce similar Antarctic T_{air} records (28, 77, 81). We can thus use the Antarctic $\delta^{18}O_{ice}$ stack record as a proxy for Antarctic T_{air} changes.

We also built an Antarctic T_{air} stack of the EDC, EDML, and WD sites, which requires a correction of $\delta^{18}O_{ice}$ for seawater $\delta^{18}O$ variations due to land ice volume variations. We corrected the EDC, EDML, and WD $\delta^{18}O_{ice}$ records for seawater $\delta^{18}O$ variations following refs. 28 and 76. Before correcting the Antarctic $\delta^{18}O_{ice}$ records, we resampled every 10 y and synchronized the seawater $\delta^{18}O$ record (82)–the record used for ice-volume correction–on the core MD95-2042 benthic foraminiferal $\delta^{18}O$ record (7), itself placed on the core MD95-2042 chronology used in this study (see section *Ice-Core and Core MD95-2042 Chronologies*, below). We then converted the corrected EDC, EDML, and WD $\delta^{18}O_{ice}$ records into T_{air} following ref. 76, before building the Antarctic T_{air} stack as described above.

Ice-Core and Core MD95-2042 Chronologies. The ice-core chronologies for the 60 to 12 ka BP period are based on the latest bipolar synchronization (49) that uses the annual-layer-based Greenland Ice core Chronology 2005 (83–85) modified by ref. 49, with ages multiplied by 1.0063, following ref. 86 for alignment to Chinese speleothems (see locations in Fig. 1; ref. 20)–after 12 ka BP, ice-core records are synchronized on the WAIS Divide ice core chronology 2014 (86, 87) as per ref. 75. The core MD95-2042 chronology for the 43 to 12 ka BP period is obtained using the OxCal 4.4.2 software (88, 89) and previously published ^{14}C ages (68, 90–93) recalibrated with the Marine20 calibration curve (*SI Appendix*, Table S1; ref. 94)–we added two tie points at the core top and at the end of the Younger Dryas to tentatively constrain the core MD95-2042 chronology after 12 ka BP. We corrected ^{14}C ages for a preindustrial marine reservoir age of 500 y ($\Delta R = -50 \pm 100$ y) for consistency with previous studies (91–93), except during H1 ($\Delta R = 350 \pm 200$ y) to take into account the likely larger reservoir age during this H stadial (94–97). While ^{14}C ages older than 41 ky were obtained and gave corresponding calibrated ages older than 43 ky, these ^{14}C ages were deemed imprecise, given their relatively large uncertainties (*SI Appendix*, Table S1). The ice-core chronologies for the 115 to 60 ka BP period and the core MD95-2042 chronology for the 160 to 43 ka BP period were obtained with alignments to Chinese speleothems (20), as described in ref. 23–before 115 ka BP, ice-core records are synchronized on the Antarctic Ice Core Chronology 2012 by refs. 98 and 99. We also adjusted the Antarctic Temperature Stack (76) chronology to the ice-core chronology described here for this study.

Temperature Amplitudes and Event Durations. We named H and H-like stadials as the corresponding H events in ref. 65, except H2 and two H-like stadials. Rather than considering a single H2 stadial, we considered twinned subevents of H2 that we name H2a and H2b after ref. 57, with H2a as a H stadial and H2b as a H-like stadial. We named one H-like stadial H5′ after ref. 27 instead of H5a after ref. 66 and we named C24 the H stadial preceding H10 after ref. 100. We named DO-AIM pairs following the nomenclature of refs. 30, 47, and 48, with DO stadials named after their respective AIM events rather than with the Greenland stadial nomenclature proposed by ref. 101 and adopted by ref. 54.

We calculated ΔT_n and Δt_n values using the T_{air} record from Greenland (25) (Fig. 2*A*) and the $U^{K'}_{37}$ and RI-OH′ SST and ice-volume–corrected planktic foraminiferal $\delta^{18}O$ records from the Iberian Margin core MD95-2042 (Fig. 2 *B* and *C* and *SI Appendix*, Fig. S1*B*; see Fig. 1 for locations and section *Biomarker Analysis in Core MD95-2042* for analytical details, above). We determined ΔT_s values using the Antarctic Temperature Stack (76), the ice-volume–corrected benthic foraminiferal $\delta^{18}O$ record from the Iberian Margin core MD95-2042 (*SI Appendix*, Fig. S1*C*), and our Antarctic $\delta^{18}O_{ice}$ (Fig. 2*D*) and T_{air} stacks (see section *Antarctic* $\delta^{18}O_{ice}$ *and* T_{air} *Stacks*, above). To correct foraminiferal $\delta^{18}O$ records for ice volume changes, we subtracted the seawater $\delta^{18}O$ record (82)–the ice-sheet component–to both foraminiferal $\delta^{18}O$ records after a synchronization on the core MD95-2042 chronology used in this study (see section *Ice-Core and Core MD95-2042 Chronologies*, above) and a resampling of the three $\delta^{18}O$ records every 10 y. Given the opposite correlation between foraminiferal $\delta^{18}O$ and temperature–SST or deep ocean temperature for planktic and benthic foraminifera, respectively–in comparison with the other selected paleothermometric proxies, we took the opposite values of both ice-volume–corrected foraminiferal $\delta^{18}O$ records before calculating their Δt_n, ΔT_n, and ΔT_s values. We also calculated ΔT_n and Δt_n values using band-pass–filtered Northern Hemisphere records and ΔT_s values using band-pass–filtered or simulated Southern Hemisphere records (see section *Thermal Bipolar Seesaw Model*, below).

To determine ΔT_s values, we took the difference between the value at the onset of the AIM event and the highest AIM value (*SI Appendix*, Fig. S14 *D* and *H*).

Downloaded from https://www.pnas.org by 86.216.178.75 on March 13, 2023 from IP address 86.216.178.75.

We calculated ΔT_n values following two end-member scenarios (*SI Appendix*, Fig. S14 *A–C* and *E–G* and Text S8). For Scenario 1, we defined ΔT_n values as the difference between the lowest DO stadial value and the value at the start of the abrupt transition to the DO stadial. As was recently performed by ref. 54, we determined visually the start of the abrupt transition to the DO stadial. For Scenario 2, we defined ΔT_n values as the difference between the lowest DO stadial value and the highest preceding DO interstadial value. We obtained a set of ΔT_n and ΔT_s values for each of the observed, filtered, and simulated temperature records that we selected. For observed ice-core records, we generated a 5-point moving average for NGRIP T_{air} and 11-point moving averages for Antarctic stacks in order to suppress the influence of high-frequency noise.

To determine Δt_n values, we determined visually the midpoints of DO stadial onsets and terminations, as was recently performed by ref. 54 (*SI Appendix*, Fig. S14 *A–C* and *E–G*). We obtained a set of Δt_n values for Greenland and another set of Δt_n values for the Iberian Margin. We first applied a 5-point moving average for NGRIP T_{air} in order to facilitate Δt_n value determination.

To allow the relative comparison of temperature amplitudes between Greenland and the Iberian Margin (*SI Appendix*, Text S5) and to circumvent the imperfections of existing proxy-temperature calibrations (25, 27, 59, 60, 73, 102–106), we centered to zero means and normalized to unit SDs all observed Northern and Southern Hemisphere temperature records over the 129 to 0 ka BP period, which is covered by all paleothermometric records plotted in Fig. 2 *A–D* and *SI Appendix*, Fig. S1. Consequently, $\Delta T_n{\cdot}\Delta t_n$ and $\Delta T_s{\cdot}\Delta t_n$ values are expressed in normalized °C.y rather than in °C.y.

We excluded a few problematic DO-AIM pairs occurring during the last 160 ky from our analysis. Indeed, the DO stadials paired with AIM23, AIM21, and AIM14 have submillennial warm events in Greenland (Fig. 2*A* and *SI Appendix*, Fig. S14 *A* and *E*) which are poorly resolved, if at all, in the Iberian Margin (Fig. 2 *B* and *C* and *SI Appendix*, Fig. S14 *B*, *C*, *F*, and *G*). We thus treated DO stadials 23, 21, and 14–equivalent to Greenland stadials GS24, GS22, and GS15 in ref. 23–as single events for all Northern Hemisphere records. Following ref. 54, we excluded two DO stadials shorter than 300 y–named Greenland stadials GS17.2 and GS16.2 in ref. 54–and their Southern Hemisphere counterparts from our study. The DO stadials paired with AIM16 and AIM15 thus correspond to Greenland stadials GS17.1 and GS16.1 in ref. 54, respectively. Given their very small AIM amplitudes and very short DO stadial durations (Fig. 2 *A* and *D*), we excluded the DO-AIM pairs 22 and 13. Given their lower resolution compared with Greenland paleothermometric records, the Iberian Margin SST records did not allow to simulate the DO-AIM pair 9 (Fig. 4). Therefore, we excluded the DO-AIM pair 9 from all Southern versus Northern Hemisphere diagrams based on synthetic Southern Hemisphere records simulated with the Iberian Margin SST records.

Bipolar Seesaw Index. We defined the Bipolar Seesaw Index (BSI) as the distance between the origin and the orthogonal projection on the regression line of each point in the $\Delta T_s{\cdot}\Delta t_n$ versus $\Delta T_n{\cdot}\Delta t_n$ diagram (Eq. **2**). As a representative example, we provide the BSI for the $\Delta T_s{\cdot}\Delta t_n$ versus $\Delta T_n{\cdot}\Delta t_n$ diagram for our Antarctic $\delta^{18}O_{ice}$ stack and our core MD95-2042 RI-OH′ record (Fig. 3 *C* and *D*). We first determined the slope (*S*) of the regression line through the origin of all points by using the "deming" function of the deming R package (107). For simplicity we took similar errors on both coordinates for all points: 1 y for Δt_n values, 0.001 (normalized) °C for ΔT_s values, and 1 (normalized) °C.y for $\Delta T_n{\cdot}\Delta t_n$ and $\Delta T_s{\cdot}\Delta t_n$ values. We then calculated the BSI as the distance between the origin and the orthogonal projection:

$$\mathrm{BSI} = \frac{\left|\Delta T_n \cdot \Delta t_n + S{\cdot}\Delta T_s{\cdot}\Delta t_n\right|}{\sqrt{1+S^2}}. \qquad [2]$$

Thermal Bipolar Seesaw Model. To generate synthetic Southern Hemisphere signals (T_S) from Northern Hemisphere signals (T_N) convoluted with the time characteristic of the heat reservoir (T = 1,120 y, as per ref. 46), we solved the differential equation Eq. **3** (Equation 1 in ref. 46) every 10 y using the "ode" function of the "deSolve" R package (108):

$$\frac{dT_S(t)}{dt} = \frac{1}{\mathrm{T}}\left[-T_N(t) - T_S(t)\right]. \qquad [3]$$

To focus on the abrupt variability, we centered to zero means the evenly resampled records (every 10 y) before applying a fourth-order Butterworth band-pass filter (500- to 10,000-y or 500- to 16,000-y window) over the 7 to 120 or 4 to 123 ka BP period to limit the edge effect over the 12 to 115 ka BP period. We used the "linterp" function of the "astrochron" R package (109) for resampling and the "butterworth.wge" function of the "tsgwe" R package (110, 111) for filtering. We then used the "ccf" R function (112) for phase relationship analyses. We assumed that the first $T_S(k_0)$ value at 120 or 123 ka BP is 0, following refs. 46 and 113–see *SI Appendix*, Text S10 for comparisons with a discretized thermal bipolar seesaw model and considerations about the T value.

Uncertainty Analysis. We employed a Monte Carlo method modified from ref. 54. Using the "MonteCarlo" R package (114), we randomly perturbed all Northern and Southern Hemisphere temperature records by drawing all their data points from normal distributions centered on their measured values and with SDs set as the analytical uncertainties for the core MD95-2042 RI-OH′ (0.008 RI-OH′ units equivalent to 0.19 °C based on 37 replicate analyses of the same standard; this study), $U^{K'}_{37}$ (0.010 $U^{K'}_{37}$ units equivalent to 0.26 °C; ref. 27), and planktic and benthic foraminiferal $\delta^{18}O$ values (0.1‰; ref. 69), the 1σ CIs around our Antarctic $\delta^{18}O_{ice}$ and T_{air} stacks, and the rms errors between raw and 500-y smoothed time series–with a fourth-order Butterworth low-pass filter–for NGRIP T_{air} (0.85 °C) and $\delta^{18}O_{ice}$ (0.60‰). For simplicity, we used the same delimitations for event durations and temperature amplitudes as those based on original temperature records for all Monte Carlo iterations. For comparison purposes, we also randomly perturbed ΔT_n values for Greenland by drawing them from normal distributions centered on the calculated ΔT_n values and with SDs set as the published uncertainty in ΔT_n values (1σ = 1.5 °C; ref. 25). After 1,000 Monte Carlo iterations, we repeated all analyses for each iteration–except the interhemispheric correlations for restricted populations of DO-AIM pairs, given the typically nonsignificant correlations–and reported 95% CIs as intervals between the 2.5th and 97.5th percentiles.

We also employed a bootstrapping method as a complement to the Monte Carlo method in order to compare interhemispheric correlations as depicted by Southern versus Northern Hemisphere diagrams. Using the "boot" R package (115, 116), we ran 1,000 bootstrap iterations for each correlation comparison and reported 95% CIs of the differences in absolute coefficient correlation values. Here again, we focused on interhemispheric correlations for all DO-AIM pairs.

Data, Materials, and Software Availability. All new data are available at Zenodo and PANGAEA: https://doi.org/10.5281/zenodo.7587300 (117). Previously published tetraether-based data from core MD95-2042 for the 160 to 45 ka BP period are available at https://doi.pangaea.de/10.1594/PANGAEA.927622. Alkenone-based data from core MD95-2042 are available in the supplement of ref. 27 for the 70 to 0 ka BP period and at https://doi.pangaea.de/10.1594/PANGAEA.927622 for the 160 to 70 ka BP period. Foraminiferal $\delta^{18}O$ data from core MD95-2042 are available at https://doi.pangaea.de/10.1594/PANGAEA.60829 and https://doi.pangaea.de/10.1594/PANGAEA.58195 for planktic foraminiferal $\delta^{18}O$ and at https://doi.pangaea.de/10.1594/PANGAEA.58228 for benthic foraminiferal $\delta^{18}O$. T_{air} reconstructions from Greenland are available in the supplements of refs. 24, 25, and 26, at https://www.ncdc.noaa.gov/paleo/study/22057 and https://www.ncdc.noaa.gov/paleo/study/24371 for GISP2 and NGRIP, respectively, and at https://doi.pangaea.de/10.1594/PANGAEA.905451 for GISP2. $\delta^{18}O_{ice}$ data from the NGRIP are available at https://www.iceandclimate.nbi.ku.dk/data/2010-11-19_GICC05modelext_for_NGRIP.txt and https://doi.pangaea.de/10.1594/PANGAEA.824889. $\delta^{18}O_{ice}$ data from Antarctica are available at https://www.ncdc.noaa.gov/paleo/study/27950 for EDC, at https://www.ncdc.noaa.gov/paleo/study/27950 and https://doi.pangaea.de/10.1594/PANGAEA.824888 for EDML, and in the supplement of ref. 31 for WD. Seawater $\delta^{18}O$ data are available at https://www.ncdc.noaa.gov/paleo/study/11933. The Antarctic Temperature Stack is available in the supplement of ref. 76 and at https://doi.pangaea.de/10.1594/PANGAEA.810188. The Southern Ocean SST records and stack plotted in *SI Appendix*, Fig. S6 *A–C* are available at https://doi.pangaea.de/10.1594/PANGAEA.931020, https://doi.pangaea.de/10.1594/PANGAEA.931025, and https://doi.pangaea.de/10.1594/PANGAEA.912158.

ACKNOWLEDGMENTS. Coring of MD95-2042 by the R/V Marion Dufresne was supported by the International Marine Global Change Study program. Work at CEREGE is supported by the Collège de France, including a postdoctoral salary

Downloaded from https://www.pnas.org by 86.216.178.75 on March 13, 2023 from IP address 86.216.178.75.

for N.D. We thank the referees for their numerous constructive comments: T. Stocker notably for pointing to his course for a better physical motivation of our approach and for suggesting to model idealized records; J. McManus in particular for asking for more justification on paleothermometric proxies and discussion on the chronological uncertainties; and E. Rohling notably for requesting the consideration of southern SSTs and quantitative assessments of uncertainties and of the slope of the North-South correlations in relation to heat exchange.

Author affiliations: [a]CEREGE, Aix-Marseille University, CNRS, IRD, INRAE, Collège de France, Technopôle de l'Arbois, 13545 Aix-en-Provence, France

1. D. A. Smeed *et al.*, Observed decline of the Atlantic meridional overturning circulation 2004–2012. *Ocean Sci.* **10**, 29–38 (2014).
2. L. Caesar, S. Rahmstorf, A. Robinson, G. Feulner, V. Saba, Observed fingerprint of a weakening Atlantic Ocean overturning circulation. *Nature* **556**, 191–196 (2018).
3. M. Dima, G. Lohmann, Evidence for two distinct modes of large-scale ocean circulation changes over the last century. *J. Clim.* **23**, 5–16 (2010).
4. W. Weijer, W. Cheng, O. A. Garuba, A. Hu, B. T. Nadiga, CMIP6 models predict significant 21st century decline of the Atlantic Meridional Overturning Circulation. *Geophys. Res. Lett.* **47**, e2019GL086075 (2020).
5. K. H. Kilbourne *et al.*, Atlantic circulation change still uncertain. *Nat. Geosci.* **15**, 165–167 (2022).
6. T. F. Stocker, A. Schmittner, Influence of CO_2 emission rates on the stability of the thermohaline circulation. *Nature* **388**, 862–865 (1997).
7. N. J. Shackleton, M. A. Hall, E. Vincent, Phase relationships between millennial-scale events 64000–24000 years ago. *Paleoceanography* **15**, 565–569 (2000).
8. J. F. McManus, R. Francois, J.-M. Gherardi, L. D. Keigwin, S. Brown-Leger, Collapse and rapid resumption of Atlantic meridional circulation linked to deglacial climate changes. *Nature* **428**, 834–837 (2004).
9. A. M. Piotrowski, S. L. Goldstein, S. R. Hemming, R. G. Fairbanks, Temporal relationships of carbon cycling and ocean circulation at glacial boundaries. *Science* **307**, 1933–1938 (2005).
10. L. G. Henry *et al.*, North Atlantic ocean circulation and abrupt climate change during the last glaciation. *Science* **353**, 470–474 (2016).
11. H. C. Ng *et al.*, Coherent deglacial changes in western Atlantic Ocean circulation. *Nat. Commun.* **9**, 2947 (2018).
12. Y. Zhou *et al.*, Enhanced iceberg discharge in the western North Atlantic during all Heinrich events of the last glaciation. *Earth Planet. Sci. Lett.* **564**, 116910. (2021).
13. North Greenland Ice Core Project members, High-resolution record of Northern Hemisphere climate extending into the last interglacial period. *Nature* **431**, 147–151 (2004).
14. G. C. Bond *et al.*, Correlations between climate records from North Atlantic sediments and Greenland ice. *Nature* **365**, 143–147 (1993).
15. W. Dansgaard *et al.*, Evidence for general instability of past climate from a 250-kyr ice-core record. *Nature* **364**, 218–220 (1993).
16. W. Dansgaard *et al.*, "North Atlantic climatic oscillations revealed by deep Greenland ice cores" in *Climate Processes and Climate Sensitivity*, (American Geophysical Union AGU, 1984), pp. 288–298.
17. H. Oeschger *et al.*, "Late glacial climate history from ice cores" in *Climate Processes and Climate Sensitivity*, (American Geophysical Union AGU, 1984), pp. 299–306.
18. H. Heinrich, Origin and consequences of cyclic ice rafting in the Northeast Atlantic Ocean during the past 130,000 years. *Q. Res.* **29**, 142–152 (1988).
19. J. B. Pedro *et al.*, Dansgaard-Oeschger and Heinrich event temperature anomalies in the North Atlantic set by sea ice, frontal position and thermocline structure. *Q. Sci. Rev.* **289**, 107599 (2022).
20. H. Cheng *et al.*, The Asian monsoon over the past 640,000 years and ice age terminations. *Nature* **534**, 640–646 (2016).
21. K. S. Casey, T. B. Brandon, P. Cornillon, R. Evans, "The past, present, and future of the AVHRR pathfinder SST program" in *Oceanography from Space: Revisited*, V. Barale, J. F. R. Gower, L. Alberotanza, Eds. (Springer, Netherlands, 2010), pp. 273–287.
22. K. S. Casey, E. J. Kearns, V. Halliwell, R. Evans, AVHRR Pathfinder version 5.0 and 5.1 global 4km sea surface temperature (SST) daily, 5-day, and monthly harmonic climatologies for 1982-2008. [monthly]. NOAA National Centers for Environmental Information. Dataset (2011). https://www.ncei.noaa.gov/archive/accession/AVHRR_Pathfinder-NODC-v5.0_v5.1-climatologies (Accessed 15 January 2020).
23. N. Davtian, E. Bard, S. Darfeuil, G. Ménot, F. Rostek, The novel hydroxylated tetraether index RI-OH′ as a sea surface temperature proxy for the 160–45 ka BP period off the Iberian Margin. *Paleoceanogra. Paleoclimatol.* **36**, e2020PA004077 (2021).
24. T. Kobashi *et al.*, Volcanic influence on centennial to millennial Holocene Greenland temperature change. *Sci. Rep.* **7**, 1441 (2017).
25. P. Kindler *et al.*, Temperature reconstruction from 10 to 120 kyr b2k from the NGRIP ice core. *Clim. Past* **10**, 887–902 (2014).
26. NEEM community members, Eemian interglacial reconstructed from a Greenland folded ice core. *Nature* **493**, 489–494 (2013).
27. S. Darfeuil *et al.*, Sea surface temperature reconstructions over the last 70 kyr off Portugal: Biomarker data and regional modeling. *Paleoceanography* **31**, 40–65 (2016).
28. B. Stenni *et al.*, The deuterium excess records of EPICA Dome C and Dronning Maud Land ice cores (East Antarctica). *Q. Sci. Rev.* **29**, 146–159 (2010).
29. EPICA community members, Eight glacial cycles from an Antarctic ice core. *Nature* **429**, 623–628 (2004).
30. EPICA Community Members, One-to-one coupling of glacial climate variability in Greenland and Antarctica. *Nature* **444**, 195–198 (2006).
31. WAIS Divide Project Members, Precise interpolar phasing of abrupt climate change during the last ice age. *Nature* **520**, 661–665 (2015).
32. E. J. Steig *et al.*, Recent climate and ice-sheet changes in West Antarctica compared with the past 2,000 years. *Nat. Geosci.* **6**, 372–375 (2013).
33. WAIS Divide Project Members, Onset of deglacial warming in West Antarctica driven by local orbital forcing. *Nature* **500**, 440–444 (2013).
34. S. J. Johnsen *et al.*, Irregular glacial interstadials recorded in a new Greenland ice core. *Nature* **359**, 311–313 (1992).
35. P. M. Grootes, M. Stuiver, J. W. C. White, S. Johnsen, J. Jouzel, Comparison of oxygen isotope records from the GISP2 and GRIP Greenland ice cores. *Nature* **366**, 552–554 (1993).
36. A. Ganopolski, S. Rahmstorf, Rapid changes of glacial climate simulated in a coupled climate model. *Nature* **409**, 153–158 (2001).
37. C. Li, D. S. Battisti, D. P. Schrag, E. Tziperman, Abrupt climate shifts in Greenland due to displacements of the sea ice edge. *Geophys. Res. Lett.* **32**, L19702 (2005).
38. C. Li, D. S. Battisti, C. M. Bitz, Can North Atlantic sea ice anomalies account for Dansgaard-Oeschger climate signals? *J. Clim.* **23**, 5457–5475 (2010).
39. C. Li, A. Born, Coupled atmosphere-ice-ocean dynamics in Dansgaard-Oeschger events. *Q. Sci. Rev.* **203**, 1–20 (2019).
40. C. He *et al.*, Abrupt Heinrich Stadial 1 cooling missing in Greenland oxygen isotopes. *Sci. Adv.* **7**, eabh1007 (2021).
41. R. Knutti, J. Flückiger, T. F. Stocker, A. Timmermann, Strong hemispheric coupling of glacial climate through freshwater discharge and ocean circulation. *Nature* **430**, 851–856 (2004).
42. R. J. Stouffer *et al.*, Investigating the causes of the response of the thermohaline circulation to past and future climate changes. *J. Clim.* **19**, 1365–1387 (2006).
43. Z. Liu *et al.*, Transient simulation of last deglaciation with a new mechanism for Bølling-Allerød warming. *Science* **325**, 310–314 (2009).
44. J. B. Pedro *et al.*, Beyond the bipolar seesaw: Toward a process understanding of interhemispheric coupling. *Q. Sci. Rev.* **192**, 27–46 (2018).
45. T. F. Stocker, The seesaw effect. *Science* **282**, 61–62 (1998).
46. T. F. Stocker, S. J. Johnsen, A minimum thermodynamic model for the bipolar seesaw. *Paleoceanography* **18**, 1087 (2003).
47. E. Capron *et al.*, Synchronising EDML and NorthGRIP ice cores using $\delta^{18}O$ of atmospheric oxygen ($\delta^{18}O_{atm}$) and CH_4 measurements over MIS 5 (80–123 kyr). *Q. Sci. Rev.* **29**, 222–234 (2010).
48. E. Capron *et al.*, Millennial and sub-millennial scale climatic variations recorded in polar ice cores over the last glacial period. *Clim. Past* **6**, 345–365 (2010).
49. A. Svensson *et al.*, Bipolar volcanic synchronization of abrupt climate change in Greenland and Antarctic ice cores during the last glacial period. *Clim. Past* **16**, 1565–1580 (2020).
50. T. Blunier, E. J. Brook, Timing of millennial-scale climate change in Antarctica and Greenland during the last glacial period. *Science* **291**, 109–112 (2001).
51. B. Stenni *et al.*, Expression of the bipolar see-saw in Antarctic climate records during the last deglaciation. *Nat. Geosci* **4**, 46–49 (2011).
52. M. Siddall *et al.*, Using a maximum simplicity paleoclimate model to simulate millennial variability during the last four glacial periods. *Q. Sci. Rev.* **25**, 3185–3197 (2006).
53. V. Margari *et al.*, The nature of millennial-scale climate variability during the past two glacial periods. *Nat. Geosci.* **3**, 127–131 (2010).
54. P. Zheng, J. B. Pedro, M. Jochum, S. O. Rasmussen, Z. Lai, Different trends in Antarctic temperature and atmospheric CO_2 during the last glacial. *Geophys. Res. Lett.* **48**, e2021GL093868 (2021).
55. P. J. Reimer *et al.*, The IntCal20 Northern Hemisphere radiocarbon age calibration curve (0–55 cal kBP). *Radiocarbon* **62**, 725–757 (2020).
56. E. Bard *et al.*, Retreat velocity of the North Atlantic polar front during the last deglaciation determined by ^{14}C accelerator mass spectrometry. *Nature* **328**, 791–794 (1987).
57. E. Bard, F. Rostek, J.-L. Turon, S. Gendreau, Hydrological impact of Heinrich events in the subtropical northeast Atlantic. *Science* **289**, 1321–1324 (2000).
58. F. Eynaud, J. L. Turon, M. F. Sánchez-Goñi, S. Gendreau, Dinoflagellate cyst evidence of 'Heinrich-like events' off Portugal during the Marine Isotopic Stage 5. *Marine Micropaleontol.* **40**, 9–21 (2000).
59. C. Buizert *et al.*, Antarctic surface temperature and elevation during the Last Glacial Maximum. *Science* **372**, 1097–1101 (2021).
60. B. R. Markle, E. J. Steig, Improving temperature reconstructions from ice-core water-isotope records. *Clim. Past* **18**, 1321–1368 (2022).
61. D. Pailler, E. Bard, High frequency palaeoceanographic changes during the past 140 000 yr recorded by the organic matter in sediments of the Iberian Margin. *Palaeogeogra. Palaeoclimatol. Palaeoecol.* **181**, 431–452 (2002).
62. B. Martrat *et al.*, Four climate cycles of recurring deep and surface water destabilizations on the Iberian Margin. *Science* **317**, 502–507 (2007).
63. T. F. Stocker, *Introduction to Climate Modelling* (University of Bern, 2022), pp. 1–209, https://climatehomes.unibe.ch/~stocker/stocker22icm.pdf.
64. R. B. Alley, P. U. Clark, The deglaciation of the Northern Hemisphere: A global perspective. *Annu. Rev. Earth Planet. Sci.* **27**, 149–182 (1999).
65. J. N. Bassis, S. V. Petersen, L. Mac Cathles, Heinrich events triggered by ocean forcing and modulated by isostatic adjustment. *Nature* **542**, 332–334 (2017).
66. H. Rashid, R. Hesse, D. J. W. Piper, Evidence for an additional Heinrich event between H5 and H6 in the Labrador Sea. *Paleoceanography* **18**, 1077 (2003).
67. N. Thouveny *et al.*, Rock magnetic detection of distal ice-rafted debries: Clue for the identification of Heinrich layers on the Portuguese margin. *Earth Planet. Sci. Lett.* **180**, 61–75 (2000).
68. E. Bard, F. Rostek, G. Ménot-Combes, Radiocarbon calibration beyond 20,000 ^{14}C yr B.P. by means of planktonic foraminifera of the Iberian Margin. *Q. Res.* **61**, 204–214 (2004).
69. O. Cayre, Y. Lancelot, E. Vincent, M. A. Hall, Paleoceanographic reconstructions from planktonic foraminifera off the Iberian Margin: Temperature, salinity, and Heinrich events. *Paleoceanography* **14**, 384–396 (1999).
70. A. Landais *et al.*, A review of the bipolar see–saw from synchronized and high resolution ice core water stable isotope records from Greenland and East Antarctica. *Q. Sci. Rev.* **114**, 18–32 (2015).
71. A. A. Cimatoribus, S. S. Drijfhout, V. Livina, G. van der Schrier, Dansgaard-Oeschger events: Bifurcation points in the climate system. *Clim. Past* **9**, 323–333 (2013).
72. V. Brovkin *et al.*, Past abrupt changes, tipping points and cascading impacts in the Earth system. *Nat. Geosci.* **14**, 550–558 (2021).

Downloaded from https://www.pnas.org by 86.216.178.75 on March 13, 2023 from IP address 86.216.178.75.

73. X. Lü *et al.*, Hydroxylated isoprenoid GDGTs in Chinese coastal seas and their potential as a paleotemperature proxy for mid-to-low latitude marginal seas. *Org. Geochem.* **89–90**, 31–43 (2015).
74. S. Schouten, E. C. Hopmans, E. Schefuß, J. S. Sinninghe Damsté, Distributional variations in marine crenarchaeotal membrane lipids: A new tool for reconstructing ancient sea water temperatures? *Earth Planet. Sci. Lett.* **204**, 265–274 (2002).
75. C. Buizert *et al.*, Abrupt ice-age shifts in southern westerly winds and Antarctic climate forced from the north. *Nature* **563**, 681–685 (2018).
76. F. Parrenin *et al.*, Synchronous change of atmospheric CO_2 and Antarctic temperature during the last deglacial warming. *Science* **339**, 1060–1063 (2013).
77. J. Jouzel *et al.*, Orbital and millennial Antarctic climate variability over the past 800,000 years. *Science* **317**, 793–796 (2007).
78. G. Delaygue, J. Jouzel, V. Masson, R. D. Koster, E. Bard, Validity of the isotopic thermometer in central Antarctica: Limited impact of glacial precipitation seasonality and moisture origin. *Geophys. Res. Lett.* **27**, 2677–2680 (2000).
79. J. Jouzel *et al.*, Magnitude of isotope/temperature scaling for interpretation of central Antarctic ice cores. *J. Geophys. Res. Atmosp.* **108**, 4361 (2003).
80. M. Werner, J. Jouzel, V. Masson-Delmotte, G. Lohmann, Reconciling glacial Antarctic water stable isotopes with ice sheet topography and the isotopic paleothermometer. *Nat. Commun.* **9**, 3537 (2018).
81. B. Stenni *et al.*, A late-glacial high-resolution site and source temperature record derived from the EPICA Dome C isotope records (East Antarctica). *Earth Planet. Sci. Lett.* **217**, 183–195 (2004).
82. R. Bintanja, R. S. W. van de Wal, North American ice-sheet dynamics and the onset of 100,000-year glacial cycles. *Nature* **454**, 869–872 (2008).
83. K. K. Andersen *et al.*, The Greenland Ice core chronology 2005, 15–42 ka. Part 1: Constructing the time scale. *Q. Sci. Rev.* **25**, 3246–3257 (2006).
84. A. Svensson *et al.*, A 60 000 year Greenland stratigraphic ice core chronology. *Clim. Past* **4**, 47–57 (2008).
85. S. O. Rasmussen *et al.*, A new Greenland ice core chronology for the last glacial termination. *J. Geophys. Res. Atmosp.* **111**, D06102 (2006).
86. C. Buizert *et al.*, The WAIS Divide deep ice core WD2014 chronology–Part 1: Methane synchronization (68–31 ka BP) and the gas age–ice age difference. *Clim. Past* **11**, 153–173 (2015).
87. M. Sigl *et al.*, The WAIS divide deep ice core WD2014 chronology–Part 2: Annual-layer counting (0–31 ka BP). *Clim. Past* **12**, 769–786 (2016).
88. C. Bronk Ramsey, Bayesian analysis of radiocarbon dates. *Radiocarbon* **51**, 337–360 (2009).
89. C. Bronk Ramsey, OxCal 4.4.2. https://c14.arch.ox.ac.uk/oxcal.html (Accessed 11 September 2020).
90. E. Bard, F. Rostek, G. Ménot-Combes, A better radiocarbon clock. *Science* **303**, 178–179 (2004).
91. E. Bard, G. Ménot-Combes, F. Rostek, Present status of radiocarbon calibration and comparison records based on Polynesian corals and Iberian margin sediments. *Radiocarbon* **46**, 1189–1202 (2004).
92. N. J. Shackleton, R. G. Fairbanks, T. Chiu, F. Parrenin, Absolute calibration of the Greenland time scale: implications for Antarctic time scales and for $\Delta^{14}C$. *Q. Sci. Rev.* **23**, 1513–1522 (2004).
93. E. Bard *et al.*, Radiocarbon calibration/comparison records based on marine sediments from the Pakistan and Iberian Margins. *Radiocarbon* **55**, 1999–2019 (2013).
94. T. J. Heaton *et al.*, Marine20–The marine radiocarbon age calibration curve (0–55,000 cal BP). *Radiocarbon* **62**, 779–820 (2020).
95. J. V. Stern, L. E. Lisiecki, North Atlantic circulation and reservoir age changes over the past 41,000 years. *Geophys. Res. Lett.* **40**, 3693–3697 (2013).
96. C. Waelbroeck *et al.*, The timing of the last deglaciation in North Atlantic climate records. *Nature* **412**, 724–727 (2001).
97. L. C. Skinner *et al.*, Atlantic Ocean ventilation changes across the last deglaciation and their carbon cycle implications. *Paleoceanogra. Paleoclimatol.* **36**, e2020PA004074 (2021).
98. D. Veres *et al.*, The Antarctic ice core chronology (AICC2012): An optimized multi-parameter and multi-site dating approach for the last 120 thousand years. *Clim. Past* **9**, 1733–1748 (2013).
99. L. Bazin *et al.*, An optimized multi-proxy, multi-site Antarctic ice and gas orbital chronology (AICC2012): 120–800 ka. *Clim. Past* **9**, 1715–1731 (2013).
100. J. F. McManus *et al.*, High-resolution climate records from the North Atlantic during the last interglacial. *Nature* **371**, 326–329 (1994).
101. S. O. Rasmussen *et al.*, A stratigraphic framework for abrupt climatic changes during the Last Glacial period based on three synchronized Greenland ice-core records: Refining and extending the INTIMATE event stratigraphy. *Q. Sci. Rev.* **106**, 14–28 (2014).
102. S. Fietz, S. L. Ho, C. Huguet, Archaeal membrane lipid-based paleothermometry for applications in polar oceans. *Oceanog* **33**, 104–114 (2020).
103. J. E. Tierney, M. P. Tingley, A. Bayesian, spatially-varying calibration model for the TEX_{86} proxy. *Geochim. et Cosmochim. Acta* **127**, 83–106 (2014).
104. J. E. Tierney, M. P. Tingley, A TEX_{86} surface sediment database and extended Bayesian calibration. *Sci. Data* **2**, 150029 (2015).
105. M. H. Conte *et al.*, Global temperature calibration of the alkenone unsaturation index ($U^{K'}_{37}$) in surface waters and comparison with surface sediments. *Geochem. Geophys. Geosyst.* **7**, Q02005 (2006).
106. J. E. Tierney, M. P. Tingley, BAYSPLINE: A new calibration for the alkenone paleothermometer. *Paleoceanogra. Paleoclimatol.* **33**, 281–301 (2018).
107. T. Therneau, Deming, Theil-Sen, Passing-Bablock and Total Least Squares Regression (R package version 1.4, 2018).
108. K. Soetaert, T. Petzoldt, R. W. Setzer, Solving differential equations in R: Package deSolve. *J. Stat. Software* **33**, 1–25 (2010).
109. S. R. Meyers, Astrochron: An R package for astrochronology (R package version 1.1, 2021).
110. W. A. Woodward, tswge: Time Series for Data Science (R package version 2.0.0, 2022).
111. W. A. Woodward, H. L. Gray, A. C. Elliott, *Applied Time Series Analysis with R* (CRC Press, ed. 2, 2017).
112. R Core Team, *R: A language and environment for statistical computing* (Version 4.2.2, R Foundation for Statistical Computing, Vienna, Austria, 2022)
113. T. F. Stocker, S. J. Johnsen, Correction to "A minimum thermodynamic model for the bipolar seesaw". *Paleoceanography* **20**, PA1002 (2005).
114. C. H. Leschinski, MonteCarlo: Automatic Parallelized Monte Carlo Simulations (R package version 1.0.6, 2019).
115. A. Canty, B. Ripley, boot: Bootstrap R (S-Plus) Functions (R package version 1.3-28.1, 2022).
116. A. C. Davidson, D. V. Hinkley, *Bootstrap Methods and Their Applications* (Cambridge University Press, 1997).
117. N. Davtian, E. Bard, Biomarker indices and concentrations and biomarker-based temperature estimates from the Iberian Margin core MD95-2042, composite atmospheric temperature record from Greenland, and stacks of delta 18Oice and atmospheric temperature records from three Antarctic sites. Zenodo. https://doi.org/10.5281/zenodo.7587300 (Deposited 30 January 2023).

Downloaded from https://www.pnas.org by 86.216.178.75 on March 13, 2023 from IP address 86.216.178.75.

PNAS

Supporting Information for

A new view on abrupt climate changes and the bipolar seesaw based on paleotemperatures from Iberian Margin sediments

Nina Davtian and Edouard Bard

Email: Nina.Davtian@uab.cat and bard@cerege.fr

This PDF file includes:

Supporting text sections S1 to S14
Figures S1 to S18
Tables S1 to S19
SI References

Supporting Information Text

S1 Paleotemperatures in Greenland and the Iberian Margin during H and DO stadials. The temperature proxies measured in Greenland ice do not show a systematic difference between H and DO stadials (Fig. 2*A*). This is the main reason why the specificity of H stadials was not recognized in Greenland ice cores (1–4).

Another reason for overlooking the cooling difference between the two types of stadials is that the cooling difference between H stadials and normal DO stadials was not apparent in early studies of marine sediments, which were solely based on percentages of the polar foraminifera *Neogloboquadrina pachyderma sinistral* (5). This temperature proxy is not linearly related to SST and saturates at 100% in cold waters.

However, even before the discovery of the classic series of H events (6) characterized by IRD layers, it was known from geochemical and micropaleontological studies of deep-sea sediments that the H1 period corresponded to a massive cooling in the North Atlantic, more intense than the YD itself (7). Those authors wrote that *"In core SU8118 the beginning of the [deglacial] oxygen isotope decrease is characterized by a concomitant temperature drop of ca. 7 °C which can surely be attributed to a pulse-like injection of large volumes of ice or melt water into the Atlantic"*. This drastic cooling during H1 was evidenced with quantitative SSTs reconstructed with a statistical transfer function based on counts of all species of planktic foraminifera. The other novel aspect of this 1987 study was the use of a deep-sea core located mid-latitude (37°N) off the southern Iberian Margin. This North Atlantic site is relatively far from the higher latitude IRD belt, which has sediments that are usually barren of planktic foraminifera (8). Moreover, deep-sea cores from the southern Iberian Margin exhibit high sedimentation rates, allowing for the establishment of precise chronologies based on ^{14}C dating in planktic foraminifera (7, 9).

The extraordinary quality of sediments from the southern Iberian Margin was confirmed by ref. 10 which reconstructed an SST record based on planktic foraminifera from a new core covering the entire glacial cycle—MD95-2042 located at the same site as core SU8118 used in refs. 7 and 11. The previous observation of a pronounced cooling during H1 was clearly confirmed with all other H stadials, contrasting with the moderate cooling reconstructed for normal DO stadials (10). An additional outcome of the transfer function based on planktic foraminifera are estimations of summer and winter SSTs. The Iberian Margin records (7, 10, 12, 13) show minimal changes of the seasonality. Notably, there is a lack of diverging temperature trends during DO stadials, with warming for summers and cooling for winters as hypothesized recently (14).

The systematic SST pattern based on planktic foraminifera was further strengthened on the same or nearby cores from the Iberian Margin, with geochemical paleothermometric proxies such as the oxygen isotope composition ($\delta^{18}O$) of planktic foraminifera (15), the unsaturation index of alkenones ($U^{K'}_{37}$; refs. 11, 16, and 17, the Mg/Ca of planktic foraminifera (18) and the TetraEther indeX of GDGTs with 86 carbons (TEX_{86}; ref. 19). The recognition of the southern Iberian Margin as a "sweet spot" for paleoceanographic studies was further strengthened by extending the record over more than a million years by drilling the "Shackleton site" (U1385) in the framework of IODP (20).

The environmental context of the Iberian Margin and core MD95-2042 site is shown in Fig. 1 *B* and *C* and described in detail in ref. 21 and references therein. In short, the Iberian Margin has seasonal contrasts, with an upwelling that occurs in late spring/summer. In addition to North Atlantic Deep Waters, Antarctic Intermediate Waters, and Antarctic Bottom Waters, a relatively warm and salty water mass from the Mediterranean Sea flows poleward along the margin between roughly 500 to 600 and 1,500 to 1,600 m water depth. During the last glacial cycle, the hydrology was generally similar to today's, except during H and H-like stadials when the seasonal upwelling likely ceased (16).

Core MD95-2042 comprises five high-resolution (average temporal resolution < 300 y) paleothermometric records covering the entire last glacial cycle. The first high-resolution paleothermometric record from core MD95-2042 is based on the $\delta^{18}O$ of planktic foraminifera (Fig. S1*B*; ref. 15). However, non-thermal influences—e.g., changes in global ice volume and local hydrologic conditions correlated to salinities (22)—on planktic foraminiferal $\delta^{18}O$ likely

occurred, notably during H events. For these reasons, we compare the ice-volume–corrected $\delta^{18}O$ of planktic foraminifera (Fig. S1*B*) only with the ice-volume–corrected $\delta^{18}O$ of benthic foraminifera (Fig. S1*C*) in our study.

The other four high-resolution paleothermometric records from core MD95-2042 are based on the Ring Index of hydroxylated tetraethers with OH-GDGT-0 (RI-OH′), the Ring Index of hydroxylated tetraethers without OH-GDGT-0 (RI-OH), TEX_{86}, and $U^{K'}_{37}$ (Figs. 2 *B* and *C* and S2 *B* and *C*). Refs. 19 and 21 converted all biomarker-based indices into SSTs using the best available calibrations for each organic paleothermometer (ref. 23 for RI-OH′, ref. 24 for RI-OH, refs. 19, 25, and 26 for TEX_{86}, and refs. 27 and 28 for $U^{K'}_{37}$). However, TEX_{86} has relatively complicated signals during the 160 to 45 ka BP period (21), notably during H-like stadials (29) when TEX_{86} shows a peculiar behavior compared with other organic paleothermometers. Accordingly, TEX_{86} may record not only SSTs, but also temperature signals from intermediate to deep waters (water depths > 500 m) during H-like stadials (21). In addition, the expanded RI-OH record fails to show the same characteristic responses to H6 and H4 to H1 as the other organic paleothermometers (Fig. S2*B*), including TEX_{86} (Fig. S2*C*; see also ref. 19). RI-OH′ records the influence of (sub)polar waters during H stadials better than does RI-OH (21), and the tetraether-based records expanded to the 160 to 0 ka BP period strengthen this conclusion. Conversely, the recent RI-OH′ paleothermometer generally resembles the established $U^{K'}_{37}$ SST proxy (21) and this resemblance still holds for the last 45 ky (Fig. 2 *B* and *C*). Another recent application of the RI-OH′ paleothermometer in the Alboran Sea, western Mediterranean Sea, over the last 35 ky further suggests that this recent biomarker-based index is suitable for studies of H and DO stadials (30). We therefore choose the RI-OH′ and $U^{K'}_{37}$ paleothermometric records as the best core MD95-2042 SST records to be used as inputs of the thermal bipolar seesaw model (31).

S2 The Ring Index of hydroxylated tetraethers as an independent SST proxy. Organic SST proxies such as $U^{K'}_{37}$, TEX_{86}, and RI-OH′ are driven by specific biological producers and mechanisms, which differ from those for microfossil-based paleothermometric proxies such as $\delta^{18}O$ and Mg/Ca. The most established organic SST proxy, $U^{K'}_{37}$ (32), indicates the degree of saturation—the number of double bounds—of long-chain ketones produced by photosynthetic haptophyte algae (33–35). $U^{K'}_{37}$ values range from 0 to 1 and increase with increasing SST (27, 28, 32, 36, 37)—warmer SSTs give more saturated alkenones i.e. alkenones with less double bounds. One of the most recent organic SST proxies, RI-OH′ (24), indicates the degree of cyclization—the number of cycles—of hydroxylated isoprenoid tetraethers produced by ammonia-oxidizing *Thaumarchaeota* (38–46). RI-OH′ values range from 0 to 2 and increase with increasing SST (23, 24, 46–48)—warmer SSTs give more cyclized hydroxylated isoprenoid tetraethers i.e. hydroxylated isoprenoid tetraethers with more cycles. $U^{K'}_{37}$ and RI-OH′ thus rely on lipids from different biological sources—photosynthetic haptophyte algae versus ammonia-oxidizing archaea—and represent two different ways for unicellular organisms to control the fluidity or viscosity of their constituting lipids—alkenone unsaturation versus hydroxylated isoprenoid tetraether cyclization.

RI-OH′ and $U^{K'}_{37}$ show a strong correlation—*r* values of 0.86 and 0.92 over the 160 to 0 and 45 to 1 ka BP periods, respectively—and a near 1:1 relationship between their derived SSTs in core MD95-2042 sediments, which reflects a substantial shared variance (Fig. S3*A*). However, RI-OH′-SSTs are typically cooler than $U^{K'}_{37}$-SSTs, as previously reported by ref. 21, with generally larger SST differences during the 160 to 45 ka BP period than during the 45 to 0 ka BP period and a millennial variability in these SST differences that partly covaries with the DO variability (Fig. S4). RI-OH′ and $U^{K'}_{37}$ thus also show a non-random unshared variance that supports the independence of RI-OH′ from $U^{K'}_{37}$ in core MD95-2042 sediments.

The most established tetraether-based SST proxy, TEX_{86} (49), indicates the degree of cyclization—the number of cycles—of non-hydroxylated isoprenoid tetraethers produced by ammonia-oxidizing *Thaumarchaeota* (40–44, 50–52). TEX_{86} values range from 0 to 1 and increase with increasing SST (25, 49, 53–56)—warmer SSTs give more cyclized non-hydroxylated isoprenoid tetraethers i.e. non-hydroxylated isoprenoid tetraethers with more cycles. While both RI-OH′ and TEX_{86} represent isoprenoid tetraether cyclization for ammonia-oxidizing archaea to control the fluidity or viscosity of their constituting lipids, only some ammonia-oxidizing *Thaumarchaeota* strains produce both hydroxylated and non-hydroxylated isoprenoid tetraethers

(39, 42). This difference in biological producers may partly explain why TEX_{86} and its variants do not systematically covary with RI-OH′ in marine core sediments (21, 57), which supports the independence of RI-OH′ from TEX_{86}.

RI-OH′ and TEX_{86}^{H} expectedly show a strong correlation—*r* values of 0.84 and 0.90 over the 160 to 0 and 45 to 1 ka BP periods, respectively—and a near 1:1 relationship between their derived SSTs in core MD95-2042 sediments (Fig. S3*B*)—TEX_{86}^{H} values are the logarithm of TEX_{86} values. While RI-OH′-SSTs better agree with TEX_{86}^{H}-SSTs than with $U^{K'}_{37}$-SSTs during warm DO interstadials of the 160 to 45 ka BP period (Figs. S4 and S5), absolute differences between RI-OH′-SSTs and TEX_{86}^{H}-SSTs increase by up to 7 °C during cold DO stadials, notably H-like stadials during the 160 to 45 ka BP period (Fig. S5*C*). Differences between RI-OH′-SSTs and TEX_{86}^{H}-SSTs also show a clearer millennial variability than do differences between RI-OH′-SSTs and $U^{K'}_{37}$-SSTs, especially during the 160 to 45 ka BP period (Figs. S4*C* and S5*C*).

The similarities and differences in biomarker-based SSTs over the 160 to 45 ka BP period in core MD95-2042 sediments are discussed in detail in ref. 21. In short, ref. 21 pointed out that differences between RI-OH′-SSTs and $U^{K'}_{37}$-SSTs in core MD95-2042 sediments, as well as core top calibration residuals for RI-OH′, may reflect non-thermal influences to be explored while further studying paleothermometry based on hydroxylated isoprenoid tetraethers. Similarly, the reasons for larger differences between RI-OH′-SSTs and TEX_{86}^{H}-SSTs during H-like stadials in core MD95-2042 sediments are not fully constrained (21). Further work is also needed to strengthen the $U^{K'}_{37}$-SST relationship at low temperatures for the Iberian Margin. For instance, ref. 12 already mentioned a systematic difference between records based on various alkenone calibrations, specifically during cold events such as the YD and H1 for the Iberian Margin (Fig. 5 in ref. 12). Accordingly, we favor the complementary use of RI-OH′ and $U^{K'}_{37}$ to study North Atlantic paleoclimates (21) as well as their relationships with Southern Hemisphere paleoclimates via the thermal bipolar seesaw.

S3 Shortcomings for comparisons with Southern Ocean SST records. In theory, it would be more relevant to compare SSTs from the North Atlantic with SSTs from the Southern Ocean than with atmospheric temperatures from Antarctica to study the thermal bipolar seesaw. During the last 160 ky, several SST records from deep-sea cores in the Southern Ocean show millennial events similar to AIM events in Antarctica (58, 59). While ref. 59 restricted their study to the AIM events AIM12–AIM3, we could in principle generate a Southern Ocean SST stack covering the 115 to 12 ka BP period using 7 of the 14 Southern Ocean SST records stacked by ref. 59 (E11-2, ref. 60; ODP-1089, ref. 61; MD03-2607, ref. 62; SO136-111, ref. 63; MD97-2120 Mg/Ca-derived record, ref. 64; MD97-2120 $U^{K'}_{37}$-derived record, ref. 65; and MD97-2121, ref. 65) and both Southern Ocean SST records by ref. 58.

However, AIM events are generally not as well-resolved in Southern Ocean SST records, such as those stacked by ref. 59, as they are in Antarctic atmospheric temperature records, partly due to the limited time resolutions of Southern Ocean SST records compared with Antarctic atmospheric temperature records and, to a lesser extent, our Iberian Margin SST records from core MD95-2042. Consequently, ref. 59 did not systematically detect all AIM events in the selected Southern Ocean SST records.

An absolute and independent chronology of Southern Ocean records is notoriously difficult to establish as this zone is characterized by large and potentially variable ^{14}C reservoir ages, partly as a response to the variability of sea ice. Indeed, the IntCal group does not recommend the use of the Marine20 calibration for latitudes south of 40°S (66). More recently, Heaton et al. (67) provided corrections for the Southern Ocean based on 3D ocean modeling, but these first-order corrections are associated with a significant increase of uncertainty.

Importantly, ref. 59 tuned the Southern Ocean SST records stacked over the last 75 ky to the Antarctic EDC δD record on its Antarctic Ice Core Chronology (AICC12; refs. 68 and 69). This makes this Southern Ocean record somewhat redundant, but with a lower resolution than the Antarctic ice-core record. This caveat is also relevant for both SST records by ref. 58 that are also tuned to Antarctic ice-core records—Antarctic EDC δD record (70) for MD11-3353 and Antarctic Temperature Stack (71) for most of MD12-3394.

In addition, most SST proxies become rather imprecise at low temperatures typifying the Southern Ocean. For example, the slope of the $U^{K'}_{37}$-SST relationship decreases significantly (27,

72). A similar low sensitivity at cold temperature is exhibited by the Mg/Ca paleothermometer (73, 74). Further difficulties are associated with the TEX_{86} paleothermometer and its variant proposed for polar oceans, TEX_{86}^{L}, as they have particularly large calibration residuals at low temperatures, including in the Southern Ocean (23, 25, 54, 75–78), and gave some unrealistic down-core SST reconstructions in the Southern Ocean (79). Consequently, TEX_{86} is "Not recommended yet for glacial-interglacial SST reconstructions in the Southern Ocean" as concluded by ref. 80.

Despite all these pitfalls, the studies by refs. 58 and 59 are nonetheless useful in the context of our work because both are compatible with (but partly rely on) the hypothesis of an equivalence of variations in Southern Ocean and atmospheric temperatures during AIM events. When putting both Southern Ocean SST records by ref. 58 and the Southern Ocean SST stack by ref. 59 on our ice-core chronology, Fig. S6 shows that the largest AIM events can be identified in the marine records, but that the Antarctic ice-core record is needed to detect smaller AIM events. Fig. S6 also shows that our Antarctic T_{air} stack agrees with the Antarctic Temperature Stack by ref. 71 placed on the same ice-core timescale and within 2σ uncertainties.

For all these reasons, we have used the Antarctic $\delta^{18}O_{ice}$ record in our quantitative study of the thermal bipolar seesaw as in previous studies since ref. 31. Comparing with Southern Ocean SST records could be interesting for future work with strengthened chronologies and new SST records at high resolution.

In their seminal work on core MD95-2042, Shackleton et al. (15) proposed that the $\delta^{18}O$ record of planktic foraminifera can be used as a proxy for North Atlantic SST and the $\delta^{18}O$ of benthic foraminifera, at this very same North Atlantic location, could be used as a proxy of temperature around Antarctica. The advantage of this approach is to obtain both records from the same sediment core, thereby reducing the problem of timescale discrepancies between records from different sites and measured on various types of archives (see Text S6, below). However, the use of $\delta^{18}O$ has also many pitfalls because the $\delta^{18}O$ of foraminifera is not a simple paleothermometer, but rather a complex indicator influenced by several factors such as growth temperature—SST or deep ocean temperature for planktic and benthic foraminifera, respectively—hydrological changes correlated to local salinity for planktic foraminifera, and global melting of ice sheets leading to a long-term relationship between foraminiferal $\delta^{18}O$ and sea level changes. An additional drawback of the benthic foraminiferal $\delta^{18}O$ record from core MD95-2042 is its lower resolution when compared to other proxies measured on the same core (planktic foraminiferal $\delta^{18}O$, $U^{K'}_{37}$, and RI-OH′), notably during H and H-like stadials. This is due to the scarcity of benthic foraminifera at that location, notably during cold and biologically less productive periods.

Despite these problems, we also use both foraminiferal $\delta^{18}O$ records from core MD95-2042 (Fig. S1 *B* and *C*) to test the thermal bipolar model with the planktic record as the North Atlantic component and input record and the benthic record as the Southern Ocean component and reference record (Table S3). We first correct both foraminiferal $\delta^{18}O$ records for the long-term trend of seawater $\delta^{18}O$ correlated to global sea level changes (Fig. S1 *B* and *C*) and then take the opposite values of these foraminiferal $\delta^{18}O$ records for comparisons with the other selected paleothermometric records (*Materials and Methods*). Both foraminiferal $\delta^{18}O$ records give strong and significant $\Delta T_s \cdot \Delta t_n$ versus $\Delta T_n \cdot \Delta t_n$ correlations—up to $r = -0.88$ and up to $\tau = -0.76$ with $p < 0.001$ for all correlation tests (Table S3). Interestingly, we obtained the strongest $\Delta T_s \cdot \Delta t_n$ versus $\Delta T_n \cdot \Delta t_n$ correlations—up to $r = -0.94$ and up to $\tau = -0.79$ with $p < 0.001$ for all correlation tests (Table S3)—when using the RI-OH′ SST record as the Northern Hemisphere record compared to the benthic foraminiferal $\delta^{18}O$ record from core MD95-2042, which is assumed to represent the temperature variations of the Southern Ocean. These strong correlations may be linked to the advantage of studying both records in the same archive, despite the reservations about $\delta^{18}O$ listed above. However, the ice-volume–corrected benthic foraminiferal $\delta^{18}O$ record from core MD95-2042 is not competitive relative to our Antarctic $\delta^{18}O_{ice}$ stack as a Southern Hemisphere reference record, given the poorer bipolar seesaw fits (see Text S14, below).

S4 Motivation of extended Southern versus Northern Hemisphere diagrams. While we find the classical ΔT_s versus Δt_n diagram not fully satisfactory, it does give moderate-to-strong and significant inter-hemispheric relationships (81–84), including in our study (Tables S3, S7, and

S11). These results are coherent with the physical basis of the thermal bipolar seesaw. For cyclic Northern Hemisphere temperature records, Equation 9.5 from the Spring Semester 2022 lecture notes by Thomas Stocker (https://climatehomes.unibe.ch/~stocker/stocker22icm.pdf; page 162 in ref. 85)—Eq. 1 in the main text—provides an approximation that confirms the physical importance of the multiplication product $\Delta T_n \cdot \Delta t_n$ and directly motivates our use of the ΔT_s versus $\Delta T_n \cdot \Delta t_n$ diagram.

Although the $\Delta T_s \cdot \Delta t_n$ product does not seem motivated by Eq. 1, it would be proportional to the accumulated heat conservation within the Southern Hemisphere during the time Δt_n when the AMOC is weaker. This definition applies to both normalized and non-normalized temperature records. Pairing $\Delta T_n \cdot \Delta t_n$ products with $\Delta T_s \cdot \Delta t_n$ products thus allows to consider the redistribution of heat anomalies between both hemispheres, although it would be necessary to multiply non-normalized ΔT_n and ΔT_s values by the masses or volumes of the considered reservoirs and the specific heat capacity of water to express heat transfers in joules (see Text S5, below).

The possibility to quantify heat transfers between both hemispheres motivates our use of the $\Delta T_s \cdot \Delta t_n$ versus $\Delta T_n \cdot \Delta t_n$ diagram, as well as our Bipolar Seesaw Index. Furthermore, our Bipolar Seesaw Index gives values that are not redundant with Δt_n values expressed in y when using the ΔT_s versus Δt_n diagram instead, or with $\Delta T_n \cdot \Delta t_n$ values expressed in (normalized) °C.y when using the ΔT_s versus $\Delta T_n \cdot \Delta t_n$ diagram instead. The Bipolar Seesaw Index thus emphasizes real bipolar signals and reduces the importance of signals linked to other causes, notably signals significant in only one hemisphere.

To further justify the use of both extended Southern versus Northern Hemisphere diagrams—$\Delta T_s \cdot \Delta t_n$ versus $\Delta T_n \cdot \Delta t_n$ and ΔT_s versus $\Delta T_n \cdot \Delta t_n$—we use three idealized Northern Hemisphere temperature records (Fig. S7). First, an idealized Greenland temperature record with +1 °C values for warm DO interstadials that all last 2 ky and –1 °C values for cold DO stadials that either last 2 or 5 ky (solid line in Fig. S7 *A* and *D*). Second, another idealized Greenland temperature record with the same DO event durations but with +2 °C values for warm DO interstadials and –2 °C values for cold DO stadials (dashed line in Fig. S7 *A* and *D*). Third, an idealized Iberian Margin temperature record with the same DO event durations as both idealized Greenland records, but with +1 °C values for warm DO interstadials, –1 °C values for DO stadials without an H or H-like event, and –3 °C values for DO stadials with an H or H-like event (Fig. S7 *B* and *E*). We compare all idealized Northern Hemisphere temperature records with a single idealized Antarctic temperature record (Fig. S7 *C* and *F*). The idealized Antarctic temperature record is the bipolar seesaw model output from the idealized Iberian Margin temperature record, generated with the time characteristic of 1,120 y and an initial Antarctic temperature value of 0, similarly to real temperature records (*Materials and Methods*).

We generate two idealized Greenland temperature records rather than one to consider two hypotheses. The first idealized Greenland temperature record follows our hypothesis that temperature records from Greenland are truncated during H stadials, contrary to temperature records from the North Atlantic. The second idealized Greenland temperature record follows an alternative hypothesis that temperature records from Greenland record extreme coolings during all DO stadials, whereas temperature records from the North Atlantic record those extreme coolings only during H stadials. During other DO stadials, North Atlantic temperatures would be warmer due to stronger AMOC than during H stadials.

We also use two cyclic Northern Hemisphere temperature records with DO events of 2 and 5 ky and with +1.5 °C values for warm DO interstadials and –1.5 °C values for cold DO stadials (Fig. S8). We compare both cyclic Northern Hemisphere temperature records with their respective bipolar seesaw model outputs as cyclic Southern Hemisphere temperature records (Fig. S8), also generated as described in *Materials and Methods*. While cyclic temperature records allow to generate Southern versus Northern Hemisphere diagrams only when including the origin as an additional point, they complement idealized temperature records as aids to interpret Southern versus Hemisphere diagrams and their derived slopes.

We determine Δt_n and ΔT_n values from all cyclic and idealized Northern Hemisphere temperature records. We determine ΔT_s values from all cyclic and idealized Southern Hemisphere temperature records. As for real temperature records, we calculate Pearson's *r* coefficients and Kendall's τ rank coefficients for all Southern versus Northern Hemisphere

diagrams. However, we do not include temperature uncertainties in cyclic and idealized temperature records for simplicity.

We compare the classical ΔT_S versus Δt_n diagram with ΔT_S versus $\Delta T_n \cdot \Delta t_n$ and $\Delta T_S \cdot \Delta t_n$ versus $\Delta T_n \cdot \Delta t_n$ diagrams in Fig. S9. While the ΔT_S versus Δt_n and ΔT_S versus $\Delta T_n \cdot \Delta t_n$ diagrams do not show a significant relationship for Greenland—absolute r values of 0.08 with $p = 0.71$ and absolute τ values of 0.21 with $p = 0.23$—the ΔT_S versus $\Delta T_n \cdot \Delta t_n$ diagram shows a moderate and significant relationship for the Iberian Margin—$r = -0.64$ and $\tau = -0.54$, $p < 0.001$ for both correlation tests (Fig. S9). Both main populations of DO stadials—H and H-like stadials and other DO stadials—also show the same ΔT_S versus $\Delta T_n \cdot \Delta t_n$ slope, consistently with the approximation depicted in main text Eq. 1. The switch from the ΔT_S versus $\Delta T_n \cdot \Delta t_n$ diagram to the $\Delta T_S \cdot \Delta t_n$ versus $\Delta T_n \cdot \Delta t_n$ diagram gives strong and significant relationships for all idealized Northern Hemisphere records, especially the idealized Iberian Margin record—r values of up to –1.00 and τ values of up to –0.84 with $p < 0.001$ for all correlation tests (Fig. S9).

For a more accurate estimate of heat exchanges between both hemispheres, we determine AIM warming areas for cyclic and idealized Southern Hemisphere records. We assume a straight base level integration line set at the Southern Hemisphere temperature value at the onset of the corresponding AIM event. We follow the trapezoidal rule generalized to integration bases different from 0, by calculating areas every 10 y (dt) between the Southern Hemisphere temperature record (T_S) and the base level (B_S) and then summing these areas between the onset and optimum of each AIM event following Eq. S1:

$$\text{AIM warming area} = \frac{dt}{2} \sum_{k}^{\text{AIM warming}} [T_S(k) - B_S(k) + T_S(k+1) - B_S(k+1)] \quad \text{[S1]}$$

We show the Southern versus Northern Hemisphere diagram based on AIM warming areas and $\Delta T_n \cdot \Delta t_n$ values in Fig. S9. The Southern versus Northern Hemisphere diagram based on AIM warming areas shows strong and significant relationships—r values from –0.81 to –0.99 and τ values from –0.62 to –0.84 with $p < 0.001$ for all correlation tests—which are almost perfect for the Iberian Margin—$r = -0.99$ and $\tau = -0.84$, $p < 0.001$ for both correlation tests (Fig. S9). The Southern versus Northern Hemisphere diagram based on AIM warming areas thus shows relationships at least as strong as $\Delta T_S \cdot \Delta t_n$ versus $\Delta T_n \cdot \Delta t_n$ relationships.

We also tested a few additional Southern versus Northern Hemisphere diagrams that are not physically motivated by the thermal bipolar seesaw model using idealized and observed temperature records—e.g., $\Delta T_S \cdot \Delta t_S$ versus $\Delta T_n \cdot \Delta t_n$ with Δt_S for the entire duration of AIM event. While these Southern versus Northern Hemisphere diagrams give typically moderate-to-strong and significant correlations, notably for idealized and observed Iberian Margin SST records, these correlations are weaker than $\Delta T_S \cdot \Delta t_n$ versus $\Delta T_n \cdot \Delta t_n$ correlations. We thus only use the classical ΔT_S versus Δt_n diagram and the extended ΔT_S versus $\Delta T_n \cdot \Delta t_n$ and $\Delta T_S \cdot \Delta t_n$ versus $\Delta T_n \cdot \Delta t_n$ diagrams in this study.

S5 Temperature amplitude sensitivity tests using non-normalized temperature records. While we essentially used temperature records normalized to zero means and unit standard deviations, we do the same $\Delta T_S \cdot \Delta t_n$ versus $\Delta T_n \cdot \Delta t_n$ correlation exercises and uncertainty analyses for non-normalized temperature records as well (Fig. S10)—correlation test results are identical to those shown in Table S3 for normalized temperature records. When using non-normalized temperature records, $\Delta T_S \cdot \Delta t_n$ versus $\Delta T_n \cdot \Delta t_n$ diagrams generate regression slopes of roughly –0.8 for the Iberian Margin versus a slope of roughly –0.4 for Greenland (Fig. S10). Indeed, Greenland ΔT_n values are much larger than Iberian Margin ΔT_n values—x-axes with different scales between Greenland and the Iberian Margin in Fig. S10—due to continental temperature changes larger than oceanic temperature changes (86–89) and the polar amplification of temperature changes (86, 87, 90, 91). This difference in ΔT_n values explains the different regression slopes between Greenland and the Iberian Margin when using non-normalized temperature records.

In addition to inter-regional and land-ocean contrasts in ΔT_n and ΔT_s values, several shortcomings would complicate any quantitative interpretation of regression slopes beyond the geometric effect discussed below in Text S9. To quantify inter-hemispheric heat transfers expressed in joules, ΔT_n and ΔT_s values would need to be multiplied by the masses or volumes of the considered reservoirs and the specific heat capacity of water. While we implicitly assume that representative oceanic reservoirs for each hemisphere have similar masses or volumes when using ΔT_n and ΔT_s values and their derived $\Delta T_n \cdot \Delta t_n$ and $\Delta T_s \cdot \Delta t_n$ products, this assumption may be invalid, i.e. representative oceanic reservoirs for each hemisphere may have different masses or volumes.

Moreover, it would be necessary to determine ΔT_n and ΔT_s values exclusively from oceanic temperature records representative of both reservoirs, which would be better approximated with SST records from the North Atlantic and the Southern Ocean than with T_{air} records from Greenland and Antarctica. Indeed, T_{air} records, notably those from Greenland, would overestimate oceanic temperature changes as evidenced by our results, as well as a linear relationship with a regression slope different from 1 between Antarctic T_{air} changes and Southern Ocean SST changes found by ref. 59. However, existing SST records from the Southern Ocean would not allow to determine ΔT_s values for all AIM events as easily as would T_{air} records from Antarctica, as discussed above in Text S3. Furthermore, any quantitative heat transfer estimate would be uncertain due to both non-systematic analytical uncertainties in proxy values and systematic errors attributable to proxy-calibration uncertainties. For SST reconstructions from marine sediment cores, notably from polar oceans such as the Southern Ocean, smaller calibration slopes (27, 72–74, 92, 93) or larger calibration residuals (23, 25, 54, 75–78) at low temperature are major sources of uncertainty, as discussed above in Text S3. All these shortcomings motivate our use of normalized temperature records, with the inherent assumption that the shape of temperature curves provides a robust first guess for the northern and southern reservoirs involved in the thermal bipolar seesaw.

When using non-normalized temperature records, we also take advantage of the use of two rather than a single idealized Greenland temperature record (Fig. S7 *A* and *D*; see Text S4, above) to consider two hypotheses. The first idealized Greenland temperature (solid line in Fig. S7 *A* and *D*) hypothesizes that temperature records from Greenland are truncated during H stadials, contrary to SST records from the Iberian Margin. The second idealized Greenland temperature record (dashed line in Fig. S7 *A* and *D*) hypothesizes that temperature records from Greenland do record all extreme coolings during DO stadials, whereas temperature records from the Iberian Margin only record those extreme coolings during H stadials, when the heat transport by the AMOC is the most drastically reduced. The implications of both hypotheses are further illustrated in Fig. S9 showing regression slopes for the idealized temperature records (see Text S4, above). While the first hypothesis gives different regression slopes between Greenland and the Iberian Margin, the second hypothesis gives similar regression slopes for both regions (red solid lines in Fig. S9). After the normalization of idealized temperature records, both hypotheses give strictly identical regression slopes for Greenland (red dashed lines in Fig. S9). Therefore, the normalization of temperature records allows us to avoid concluding between the two hypotheses concerning differences in the variability of DO coolings between Greenland and North Atlantic temperature records. Distinguishing between the two hypotheses would require a comprehensive and accurate treatment of heat transfers between the two hemispheres, requiring coupled ocean-atmosphere-cryosphere simulations with 3D general circulation models.

S6 Main sources of uncertainties. Uncertainties in our results are due to uncertainties in paleothermometric proxy values, and to uncertainties in Greenland and Antarctic ice-core and MD95-2042 core chronologies. We focus on non-systematic uncertainties in paleothermometric proxy values, such as analytical uncertainties inferred from repeated measurements of a single sample and measurements of multiple aliquots of a single sediment (21, 94). Given that we focus on the shapes of the temperature variations by using temperature records expressed in unit standard deviation, we do not include systematic uncertainties in temperature reconstructions, such as proxy-temperature calibration uncertainties (21, 95–97) due to, for instance, non-linearities in $\delta^{18}O_{ice}$-T_{air} relationships for ice cores (95–98) and proxy-SST core top calibration

residuals for marine sediment cores (23–28). Similarly, we do not include chronological uncertainties in this study for the sake of simplicity, as discussed below in this section. Therefore, we expect the reported confidence intervals to be lower bounds for the total uncertainties in our results.

We establish one chronology for Greenland and Antarctic ice cores and another chronology for the Iberian Margin core MD95-2042, as described in *Materials and Methods*. By comparing results from the core MD95-2042 with those from Greenland and Antarctic ice cores, we lose the benefits of the exclusive use of Greenland and Antarctic ice cores, notably the bipolar synchronization with atmospheric methane (99, 100) and bipolar imprints of volcanic eruptions (101). This is particularly true for the last 60 ky when Greenland and Antarctic ice cores and core MD95-2042 have fully independent chronologies. Here, we review the different sources of chronological uncertainties relevant to Greenland and Antarctic ice cores, the marine sediment core MD95-2042, or both. For each source of chronological uncertainties, we provide the amplitude in y or in %, the relevant time period, and type of uncertainty source—systematic error or non-systematic uncertainty.

First, our ice-core chronology partly relies on two annual-layer-based chronologies, the WAIS Divide ice core chronology 2014 (WD2014) for the last 12 ky (102) and the Greenland Ice Core Chronology 2005 (GICC05) for the 60 to 12 ka BP period (103–105). The main source of uncertainty in annual-layer-based chronologies is a cumulative error inherent to annual-layer counting, which is named “maximum counting error” for the GICC05 timescale and treated as a 2σ error in GICC05 ages (103–106). Given their cumulative character, errors in annual-layer counting generate gradually larger chronological uncertainties downcore that are expressed in y or in %. For the WD2014 timescale, the uncertainty over the last 12 ky ranges from less than ±5 y for the last 2,500 y to mostly 0.5% for the rest of the Holocene (102)—the Holocene roughly covers the last 12 ky. For the GICC05 timescale, the uncertainty based on the “maximum counting error” is of 99 y—equivalent to 0.8%—at the onset of the Holocene (105, 106), 3% for the last deglaciation (105), and 5% for the 60 to 15 ka BP period (103, 104). The uncertainty in GICC05 ages also shows variations between 4% for DO interstadials and 7% for DO stadials (103), as annual-layer thickness and accumulation rates partly covary with the DO variability in atmospheric temperature (95, 103). In addition, annual-layer-based chronologies may have systematic errors, which is the case for GICC05 ages that are consistently too young by roughly 1% compared with U–Th-based ages for Chinese speleothems (99)—the U–Th-based timescale for Chinese speleothems (107) is named SpeleoAge in ref. 21. An astronomically calibrated $^{40}Ar/^{39}Ar$ age of 56.14 ± 0.44 ka (2σ) for the North Atlantic Z2 Ash (108) also supports GICC05 ages too young by 740 y for the older part of this ice-core timescale. Consequently, ref. 99 multiplied GICC05 ages on the BP timescale—0 ka BP equivalent to 1950 CE—by 1.0063 for alignment to the SpeleoAge timescale (107), a systematic correction that we apply as well for the 60 to 12 ka BP period as stated in *Materials and Methods*. Similarly, ref. 102 revealed systematic errors in ages derived from a preliminary annual-layer-based chronology for the WD ice core.

Second, our core MD95-2042 chronology for the 43 to 12 ka BP period relies on calibrated ^{14}C ages, which have two main sources of uncertainty, a systematic error and a non-systematic uncertainty. The systematic error in calibrated ^{14}C ages is related to estimates of the marine reservoir age that differ between different regions (66, 67). As stated in *Materials and Methods* and Table S1, we assume the same preindustrial marine reservoir age as for previous core MD95-2042 studies (109–111), except during H1 for which we assume a larger and more uncertain reservoir age, as per several previous studies for different regions (66, 67, 112–114). The non-systematic uncertainty in calibrated ^{14}C ages is related to the analytical precision of measured ^{14}C ages, which tends to decrease with decreasing ^{14}C content—equivalent to older ^{14}C ages—as shown in Table S1 for core MD95-2042. As stated in *Materials and Methods*, we do not use calibrated ^{14}C ages older than 43 ka BP, given the analytical uncertainties typically larger than ±1,000 y (1σ) for raw ^{14}C ages (Table S1). Instead, we tune core MD95-2042 records to the SpeleoAge timescale (107) before 43 ka BP, as per ref. 21.

Third, the latest bipolar synchronization between Greenland and Antarctic ice-core records before 60 ka BP is on the Antarctic Ice Core Chronology 2012 (AICC2012) by refs. 68 and 69. However, this timescale suffers from absolute uncertainties larger than 1,000 y before 60 ka BP (68). While refs. 115 and 116 tuned core MD95-2042 records to the AICC2012

timescale, we do not use their tuning, given the large absolute uncertainties in AICC2012 ages (68). In addition, refs. 117 and 118 found that AICC2012 ages were too young by 3,000 y compared with U–Th-based ages from Chinese and northern Alpine speleothems for the 120 to 100 ka BP period. For Greenland and Antarctic ice cores, ref. 21 and ourselves used the original AICC2012 timescale before 120 ka BP and established a transfer function from the AICC2012 timescale to the SpeleoAge timescale (107) for the 120 to 60 ka BP period. Indeed, ref. 21 also found that the multiplications of AICC2012 and GICC05 ages by 1.0063, as per ref. 99 were not applicable for ages older than 60 ka BP.

Fourth, speleothem-based $\delta^{18}O$ records from China (107), which ref. 21 and ourselves used as a reference for tuning, also have analytical uncertainties in their U–Th-based ages, although these uncertainties compare favorably with those in absolute GICC05 and AICC2012 ages. For the 60 to 43 ka BP period, the SpeleoAge timescale has uncertainties of roughly 370 to 140 y at the DO warming transitions (99). Ranges in 2σ uncertainties in U–Th-based ages are roughly 910 to 450 y for the 97 to 60 ka BP period (119), roughly 1,400 to 500 y for the 125 to 97 ka BP period (120, 121), roughly 1,600 to 800 y for the 145 to 125 ka BP period (121), and roughly 1,600 to 1,300 y for the 160 to 145 ka BP period (122).

Fifth, synchronizations of Greenland and Antarctic ice-core records have their own sources of uncertainty (68, 69, 99–101, 123). These sources of uncertainty include incorrect ties and interpolation uncertainties. While Gaussian uncertainties were assigned to volcanic tie points between Antarctic ice cores for the AICC2012 timescale (68, 69), ref. 123 did not recommend this approach and instead did a thorough quality control so that they had high confidence in the correctness of their volcanic ties. For the 60 to 12 ka BP period that benefited from the latest bipolar synchronization (101), relative age uncertainties at DO transitions are of up to 50 y. The bipolar synchronization by ref. 101 mostly relies on bipolar volcanic ties rather than solely atmospheric methane as done by refs. 99, 100, and 123, resulting in reduced relative chronological uncertainties. Indeed, ref. 100 found that the largest source of uncertainty in their results is the uncertainty in gas age–ice age differences for the WD ice core, which is a systematic error. Following their inter-hemispheric phase relationship analysis, ref. 101 subsequently suggested that the glacial gas age–ice age difference for the WD ice core was too small by 70 y on average.

Sixth, chronological uncertainties are also attributable to the accuracy and precision of our tuning to the SpeleoAge timescale for the 160 to 43 ka BP and 120 to 60 ka BP periods for core MD95-2042 and Greenland and Antarctic ice cores, respectively. As for synchronizations of Greenland and Antarctic ice-core records, tuning-related uncertainties are relative chronological uncertainties. In their review, ref. 116 considered four sources of tuning-based chronological uncertainties: a matching error, the temporal resolution of the tuned record, the temporal resolution of the reference record, and the absolute chronological uncertainties of the reference record. However, these authors did not consider chronological uncertainties inherent to the hypothesis underlying the tuning, as these uncertainties are difficult to estimate and may give very large combined chronological uncertainties. While it looks counter-intuitive to tune core MD95-2042 records to speleothem-based records from China (see Fig. 1 for locations of the mentioned records), we are confident in the hypothesis underlying our tuning to the SpeleoAge timescale as described in detail in refs. 19 and 21. In particular, the U–Th-based chronology of northern Alpine speleothems—with $\delta^{18}O$ records that reflect the DO variability more directly than do $\delta^{18}O$ records from Chinese speleothems—mostly agrees with the SpeleoAge timescale within chronological uncertainties (118). For the matching error, ref. 116 assumed uncertainties of 500 to 1,500 y when considering the planktic foraminiferal $\delta^{18}O$ from core MD95-2042 as the tuned record over the 140 to 100 ka BP period. For our study, the tuned record for core MD95-2042 is a high-resolution $CaCO_3$ record derived from the calcium X-ray fluorescence record calibrated with conventional $CaCO_3$ measurements—see refs. 19 and 21 for details. Therefore, we can neglect chronological uncertainties inherent to temporal resolutions not only for ice cores and Chinese speleothems as ref. 116 did, but also for core MD95-2042. Tuning-related uncertainties relevant to our study would thus be restricted to matching errors and the absolute uncertainties in the SpeleoAge timescale described above.

The complexity of the various chronological uncertainties, shared or not by several records, and uncertainty differences for specific time windows, as described above, would make a

formal and rigorous statistical analysis extremely difficult. Therefore, our uncertainty analysis does not include chronological uncertainties (*Materials and Methods*). However, we recognize that chronological uncertainties would be more acute when using the Iberian Margin records as model inputs to be compared with an Antarctic ice-core record. To circumvent the problem, we also include the ice-volume–corrected planktic and benthic foraminiferal $\delta^{18}O$ records for the Iberian Margin core MD95-2042 to avoid relative chronological uncertainties when considering our new biomarker-based (RI-OH′ and $U^{K'}_{37}$) SST records from the same core (see main text and Text S14, below). This exercise is like the sole comparison of ice-core records, although the analysis of marine $\delta^{18}O$ records also goes with its own tradeoffs, as discussed above in Text S3.

S7 Classical ΔT_s versus Δt_n relationships. When considering all DO-AIM pairs, Iberian Margin SST records and the Greenland T_{air} record give statistically similar correlations in ΔT_s versus Δt_n diagrams, notably for τ values and when considering 95% confidence intervals based on the bootstrapping method (Fig. S11 and Tables S3–S5, S7–S9, and S11–S13). The Iberian Margin SST records thus complement the Greenland T_{air} record for studying the thermal bipolar seesaw with the classical ΔT_s versus Δt_n diagram. However, our extension of ΔT_s versus Δt_n diagrams to the entire last glacial cycle generates *r* values of up 0.73 for observed temperature records (Table S3)—versus the *r* value of 0.92 in ref. 81. To investigate possible reasons for this weaker correlation, we consider comparable sets of DO-AIM pairs, namely DO-AIM pairs 12 to 3 (n = 11) for ref. 81, as well as DO-AIM pairs 16 to 3 (n = 14), DO-AIM pairs 16 to 10 (n = 6), and DO-AIM pairs 9 to 3 (n = 8) for ref. 84. For these sets of DO-AIM pairs, we correlate Antarctic ΔT_s with Greenland Δt_n using the sets of Antarctic ΔT_s and Greenland Δt_n values from refs. 81 and 84 and ourselves (Table S15). The use of Antarctic stacks by ref. 84 and ourselves, rather than only the EDML T_{air} record as in refs. 81 and 83, weakens the correlations for the sets of DO-AIM pairs 16 to 3, DO-AIM pairs 12 to 3, and DO-AIM pairs 9 to 3. Improved Greenland chronologies with GICC05 ages multiplied by 1.0063 (99, 100) and updated bipolar synchronizations (101, 123) also weaken the Antarctic ΔT_s versus Greenland Δt_n correlations. These results are coherent with the weakened ΔT_s versus Δt_n correlations in ref. 84—*r* values of 0.59 and 0.63 for the sets of DO-AIM pairs 16 to 3 and DO-AIM pairs 9 to 3, respectively—compared with the original ΔT_s versus Δt_n correlation in ref. 81. Conversely, our ΔT_s versus Δt_n correlations based on Greenland and Antarctic ice cores are comparable with those published in ref. 84 (Table S15). Therefore, changes of the Antarctic record and updated Greenland chronologies, in addition to an extended set of DO-AIM pairs, likely explain the weakened ΔT_s versus Δt_n correlations.

S8 Sensitivity tests with the two end-member scenarios. Scenario 1 (see description in *Materials and Methods*) defines ΔT_n values as DO coolings, so it most accurately depicts the thermal bipolar seesaw. However, Scenario 1 also involves the visual determination of the temperature at the DO stadial onset, which may be subjective and uncertain, especially for the shortest preceding DO interstadials—a similar subjectivity affects ref. 84. Scenario 2 (*Materials and Methods*) limits the subjectivity of ΔT_n value determination by taking the preceding DO optimum as the initial temperature, which usually leads to larger absolute ΔT_n values than would Scenario 1. However, AIM events start roughly 100 to 200 y after the abrupt DO cooling (Scenario 1; refs. 100, 101, and 124) rather than after the initial gradual DO cooling (Scenario 2). Overall, Scenarios 1 and 2 constitute end members that provide an upper bound for the uncertainty in ΔT_n value determinations.

With Scenario 1 and when considering all DO-AIM pairs, the Iberian Margin SST records almost systematically generate better anti-correlations than does the Greenland T_{air} record (Fig. S11 and Tables S3, S7, and S11). However, only a minority of differences in absolute *r* and τ values between Iberian Margin SST records and the Greenland T_{air} record are significant at the 95% level based on both Monte Carlo and bootstrapping methods, with more significant differences in favor than those in disfavor of the Iberian Margin over Greenland (Tables S4, S5, S8, S9, S12, and S13). Scenario 2 tends to strengthen anti-correlations compared with Scenario 1, although this trend is less obvious for non-parametric τ values than for parametric *r* values (Tables S3, S7, and S11). Scenario 2 also tends to strengthen correlations with the Greenland T_{air} record, but not sufficiently to surpass those with the Iberian Margin SST records

(Tables S4, S5, S8, S9, S12, and S13). The Iberian Margin SST records are thus competitive relative to the Greenland T_{air} record for thermal bipolar seesaw investigations, under both end-member scenarios.

S9 Regression slopes in $\Delta T_s \cdot \Delta t_n$ versus $\Delta T_n \cdot \Delta t_n$ diagrams. While our normalization procedures do not affect the relationships in Southern versus Northern Hemisphere diagrams, they result in similar regression slopes between the Greenland T_{air} record and both biomarker-based (RI-OH′ and $U^{K'}_{37}$) Iberian Margin SST records as Northern Hemisphere records (Fig. S11)—skipping the normalizations of temperature records removes these inter-regional similarities in regression slopes, as discussed in detail in Text S5, above. With the normalizations of temperature records, our extended $\Delta T_s \cdot \Delta t_n$ versus $\Delta T_n \cdot \Delta t_n$ diagram gives regression slopes of –0.97, –0.84, and –0.86 for the Greenland T_{air} and our biomarker-based Iberian Margin $U^{K'}_{37}$ and RI-OH′, respectively (Figs. 3*C* and S11). Without the normalizations of temperature records, our extended $\Delta T_s \cdot \Delta t_n$ versus $\Delta T_n \cdot \Delta t_n$ diagram gives regression slopes of –0.36, –0.77, and –0.78 for the Greenland T_{air} and our biomarker-based Iberian Margin $U^{K'}_{37}$ and RI-OH′, respectively (Fig. S10). The $\Delta T_s \cdot \Delta t_n$ versus $\Delta T_n \cdot \Delta t_n$ regression slopes from non-normalized temperature records thus suggest a prominent heat conservation deficit at the Southern Hemisphere compared with the heat loss at the Northern Hemisphere when only considering ice-core temperature records.

Using cyclic and idealized records (Figs. S7 and S8; see Text S4, above), we determine AIM warming areas (Eq. S1) to assess how well $\Delta T_s \cdot \Delta t_n$ values would estimate the accumulated heat conservation within the Southern Hemisphere. The switch from $\Delta T_s \cdot \Delta t_n$ versus $\Delta T_n \cdot \Delta t_n$ diagrams to AIM warming areas versus $\Delta T_n \cdot \Delta t_n$ diagrams flattens regression slopes by roughly 30% for idealized temperature records (Fig. S9), by roughly 36% for temperature records with cycles of 2 ky, and by roughly 21% for temperature records with cycles of 5 ky. For cyclic and idealized temperature records, areas of DO stadials are equal to $\Delta T_n \cdot \Delta t_n$ values (Fig. S9). By contrast, $\Delta T_s \cdot \Delta t_n$ values systematically overestimate AIM warming areas by a multiplication factor between 1 and 2—between 1.3 and 1.6 for the cyclized and idealized temperature records in Figs. S7 and S8—which is larger when DO stadials are shorter. This multiplication factor, which is modulated by the difference between ΔT_s and ΔT_n values, is coherent with the rectangular shape of DO stadials—$\Delta T_n \cdot \Delta t_n$—versus the triangular shape of AIM events—$\Delta T_s \cdot \Delta t_n/2$ (Figs. S7 and S8). Therefore, accurate heat transfer estimates between both hemispheres would, among other recommendations, require the integration of DO stadial and AIM warming areas for real temperature records, ideally from several continental and oceanic regions within each of the two hemispheres (see also Text S5, above).

S10 Bipolar seesaw model output comparisons and time characteristic optimizations. Our use of main text Eq. 3 (*Materials and Methods*) to obtain the cyclic and idealized Southern Hemisphere temperature records shown in Figs. S7 *C* and *F* and S8 demonstrates that we can reproduce the results of ref. 31. As a test, we also use a discretized version of the thermal bipolar seesaw model, which consists in solving Eq. S2—discretized version of Eq. 1 in ref. 31—using the first-order exponential integrator method (125), with Δ = 10 y as the sampling interval and T = 1,120 y as the time characteristic of the heat reservoir:

$$T_S(k_0 + 1) = e^{-\frac{\Delta}{\mathrm{T}}} \cdot T_S(k_0) + \left(e^{-\frac{\Delta}{\mathrm{T}}} - 1\right) \cdot T_N(k_0). \qquad [S2]$$

Based on bipolar seesaw output (BSO) comparisons, the differences between both thermal bipolar seesaw models are negligible compared with temperature uncertainties and the variability in BSO records, with almost all relative differences equivalent to relative errors < 0.1%. The discretization thus has little impact for the purposes of this study, so we use the discretized thermal bipolar seesaw model for the Monte Carlo uncertainty analysis, given its lower computational cost compared with the original thermal bipolar seesaw model.

Using T values between 100 and 4,000 y with a 10-y step, we determine the optimal T value by comparing the BSOs from both biomarker-based Iberian Margin SST records and the Greenland T_{air} (95) and $\delta^{18}O_{ice}$ (126) records with our Antarctic $\delta^{18}O_{ice}$ stack as the Southern

Hemisphere reference record using Pearson's *r* coefficients and mean squared errors (MSEs; Fig. S15)—we compare records centered to zero means and normalized to unit standard deviations over the 115 to 12 ka BP period. The optimal T values are generally > 4,000 y based on both goodness-of-fit metrics. Using a band-pass filter with a 500- to 10,000-y window, we obtain optimal T values < 4,000 y for the 115 to 12 and 43 to 12 ka BP periods when using RI-OH′ and $U^{K'}_{37}$ and for the 115 to 45 ka BP period when using $U^{K'}_{37}$ (Fig. S15 *A* and *B*). Using a band-pass filter with a 500- to 16,000-y window, we obtain optimal T values < 4,000 y for all three periods when using RI-OH′ and $U^{K'}_{37}$ and for the 43 to 12 ka BP period when using NGRIP T_{air} and $\delta^{18}O_{ice}$ (Fig. S15 *C* and *D*)—only MSEs suggest an optimal T value < 4,000 y for NGRIP T_{air}. The lack of an optimal T value < 4,000 y, notably for the 115 to 45 ka BP period, could be due to uncertain bipolar synchronizations (68, 82, 127) and to lagged Southern Hemisphere responses to Northern Hemisphere climatic events (100, 101, 123, 124). In addition, the few T optima < 4,000 y are poorly constrained when considering 95% confidence intervals, except for the 43 to 12 ka BP period (Fig. S15). Conversely, the obtained optimal T values for the 43 to 12 ka BP period using a band-pass filter with a 500- to 10,000-y window are close to the value of 1,120 y for the 65 to 25 ka BP period used by ref. 31 (Fig. S15 *A* and *B*): we thus choose the T value of 1,120 y for further investigation, using records centered to zero means and normalized to unit standard deviations over the 115 to 12 ka BP period.

S11 Comparisons between observed and simulated Antarctic records. Using a band-pass filter with a 500- to 10,000-y window, MSEs range between 0.73 and 0.96 squared normalized °C for the entire 115 to 12 ka BP period, between 0.52 and 0.88 squared normalized °C for the 43 to 12 ka BP period, and between 0.82 and 0.99 squared normalized °C for the 115 to 45 ka BP period (Table S16). The MSEs for the Greenland $\delta^{18}O_{ice}$ record are all significantly smaller than those for the Greenland T_{air} at the 95% level (Table S17)—*r* and τ values also show a significantly better goodness-of-fit for the Greenland $\delta^{18}O_{ice}$ record than for the Greenland T_{air} record at the 95% level. Except for $U^{K'}_{37}$ during the 115 to 45 ka BP period, the MSEs for both biomarker-based Iberian Margin SST records are all significantly smaller than those for both Greenland paleothermometric records at the 95% level (Table S17)—*r* and τ values also show a significantly better goodness-of-fit for both biomarker-based Iberian Margin SST records than for both Greenland paleothermometric records at the 95% level. For simplicity, we do not include chronological uncertainties (see Text S6, above), so the real 95% confidence intervals may be wider than those reported in Tables S16 and S17. Nevertheless, our thermal bipolar seesaw model results further show that Iberian Margin SST records are at least competitive relative to Greenland paleothermometric records as bipolar seesaw inputs.

We also used a band-pass filter with a wider window (500- to 16,000-y window) because the other band-pass filter (500- to 10,000-y window) artificially reduces the amplitudes of the longest DO stadials and AIM events, such as H8-AIM21, compared with shorter ones (Fig. 4*A*). The alternative band-pass filter (500- to 16,000-y window) limits the artificial amplitude reductions for H8-AIM21, strengthens most correlations between BSOs and the Southern Hemisphere record for the 115 to 45 ka BP period (Table S16), and generally gives the same results in terms of statistical significance of goodness-of-fit differences (Table S17). However, this alternative band-pass filter weakens all correlations between BSOs and the Southern Hemisphere record for the 43 to 12 ka BP period (Table S16). The original band-pass filter (500- to 10,000-y window) thus seems more appropriate for the 43 to 12 ka BP period with typically shorter DO stadials and AIM events compared with the 115 to 45 ka BP period. Nevertheless, the change of band-pass filter width has little impact on the discussion and main messages of our study.

S12 $\delta^{18}O_{ice}$ versus T_{air} records in Greenland. Based on visual and statistical comparisons with the Southern Hemisphere reference record and on cross-correlograms (Figs. 4 and S16 and Tables S16–S19), the Greenland $\delta^{18}O_{ice}$ record (126) generates a significantly better BSO simulating the Southern Hemisphere temperature than does the Greenland T_{air} record (95) at the 95% level. The contrast in goodness-of-fit between the BSOs based on both Greenland paleothermometric records may be due to the non-linear relationship between $\delta^{18}O_{ice}$ and T_{air} in Greenland (95, 128). Indeed, reliable Greenland T_{air} reconstructions also require borehole or gas

isotope measurements (95, 129–131). In parallel, the strongest non-thermic effects—e.g., moisture source, $\delta^{18}O$ of seawater, and ice-sheet elevation changes—on $\delta^{18}O_{ice}$ in Antarctica are focused on glacial inceptions and terminations (96, 98), so both Antarctic $\delta^{18}O_{ice}$ and T_{air} show clear AIM events, albeit with different shapes at both EPICA sites (EDC and EDML, see locations in Fig. 1; ref. 98). Given the temporally variable relationship between $\delta^{18}O_{ice}$ and T_{air} in Greenland, we favor Greenland T_{air} over Greenland $\delta^{18}O_{ice}$ for BSO comparisons with an Antarctic $\delta^{18}O_{ice}$ stack linearly linked to T_{air}.

S13 Inter-hemispheric phase relationships. Inter-hemispheric relationships are another aspect of the thermal bipolar seesaw (Fig. 2), so we also determine phase differences between BSOs and the Antarctic reference record with their 95% confidence intervals (*Materials and Methods*; Fig. S16 and Tables S18 and S19). Despite contrasting uncertainties in bipolar synchronizations during the last glacial cycle (68, 82, 100, 101, 123, 127), the BSOs from Greenland T_{air} and $\delta^{18}O_{ice}$ lead Antarctic $\delta^{18}O_{ice}$ during the entire last glacial cycle (Fig. S16 and Table S18). Our reported inter-hemispheric relationships between Greenland and Antarctic temperatures support the lagged Southern Hemisphere thermal bipolar seesaw responses observed by refs. 100 and 101 and those modeled by ref. 124, with the best agreements with lags of 100 to 200 y for the 43 to 12 ka BP period (Fig. S16 and Table S18). The consistent phase relationships during the entire glacial cycle also strengthen the H-like character of C24, H10, and H8 (29). The BSOs from Iberian Margin SST records also lead to phase lags of up to a few centuries (Fig. S16 and Table S18), although those phase lags are often somewhat smaller than those between ice-core records at the 95% level (Table S19). This difference in inter-hemispheric phase relationships is likely due to partly independent chronologies with different sources of uncertainty for Greenland and Antarctic ice cores and core MD95-2042 (see Text S6, above). Despite their strong correlation with each other (21), the Iberian Margin $U^{K'}_{37}$ and RI-OH′ SST records also have subtle differences (Fig. 2 *B* and *C*; see Text S2, above), which likely explains the contrasting inter-hemispheric relationships (Table S19). RI-OH′ better agrees with Greenland temperature in terms of inter-hemispheric relationships than does $U^{K'}_{37}$ (Fig. S16 and Tables S18 and S19), which strengthens the complementarity of both organic paleothermometers for studying the thermal bipolar seesaw.

S14 Bipolar seesaw model output comparisons with an alternative reference record. As acknowledged above in Text S13, chronological uncertainties affect the determination of phase differences between BSOs and the Antarctic reference record. This problem is more acute when using the Iberian Margin records as model inputs to be compared with Antarctic ice-core records (see Text S6, above). To circumvent this issue, we compare BSOs from the three core MD95-2042 SST records (RI-OH′, $U^{K'}_{37}$, and ice-volume–corrected planktic foraminiferal $\delta^{18}O$) with the core MD95-2042 ice-volume–corrected benthic foraminiferal $\delta^{18}O$ record as the alternative Southern Hemisphere reference (15) to our Antarctic $\delta^{18}O_{ice}$ stack (Figs. S17 and S18 and Tables S16–S19)—i.e. opposite values of the ice-volume–corrected benthic foraminiferal $\delta^{18}O$ record for comparison with BSOs from both biomarker-based SST records.

Visually, the three BSOs from core MD95-2042 somehow agree with the ice-volume–corrected benthic foraminiferal $\delta^{18}O$ record from the same core (Fig. S17). However, the ice-volume–corrected benthic foraminiferal $\delta^{18}O$ record has larger relative uncertainties in proxy values than does our Antarctic $\delta^{18}O_{ice}$ stack (see Fig. 4 for comparison). Indeed, we assumed an analytical uncertainty of ±0.1‰ in foraminiferal $\delta^{18}O$ values from core MD95-2042 (10), which is substantial compared with the AIM-like variability in benthic foraminiferal $\delta^{18}O$ values from core MD95-2042 corrected for ice volume changes—AIM-like amplitudes of up to 0.5‰ (Fig. S1*C*). This disadvantage adds to those stated above in Text S3—e.g., non-thermal influences on foraminiferal $\delta^{18}O$ values other than ice volume and scarcity of benthic foraminifera during cold and less productive periods.

In addition, both goodness-of-fit—*r* and τ values and MSEs—and cross-correlation results favor our Antarctic $\delta^{18}O_{ice}$ stack over the ice-volume–corrected benthic foraminiferal $\delta^{18}O$ record as the Southern Hemisphere reference record despite the chronological uncertainties (Fig. S18 and Tables S16 and S18). The poorer bipolar seesaw fits following a switch from our

Antarctic $\delta^{18}O_{ice}$ stack to the ice-volume–corrected benthic foraminiferal $\delta^{18}O$ record are most acute for the 43 to 12 ka BP period and most limited for the 115 to 45 ka BP period, which likely reflects the contrasting independence of the ice-core chronology from the core MD95-2042 chronology between these two periods—full independence for the 43 to 12 ka BP period and limited independence for the 115 to 45 ka BP period. Given the tradeoffs stated above, the reduction in relative chronological uncertainties does not suffice to make the ice-volume–corrected benthic foraminiferal $\delta^{18}O$ record competitive relative to our Antarctic $\delta^{18}O_{ice}$ stack as a Southern Hemisphere reference record.

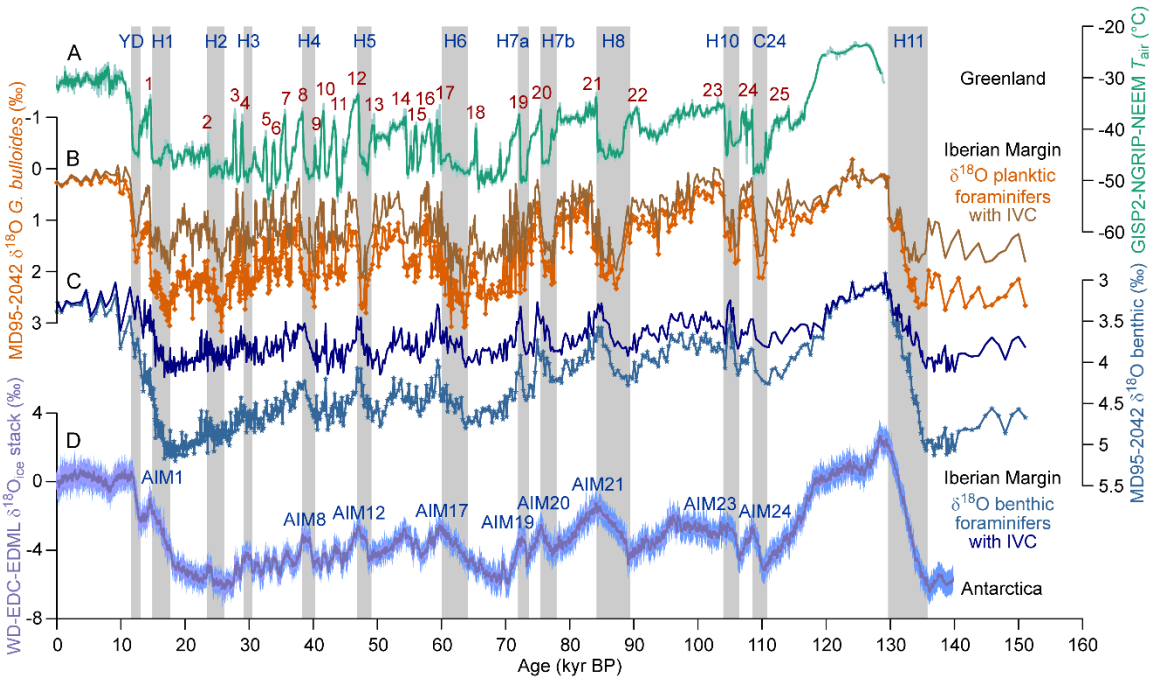

Fig. S1. Relationships between Iberian Margin foraminiferal $\delta^{18}O$ records and Greenland and Antarctic T_{air} records during the last 160 ky. (*A*) As Fig. 2*A*. (*B*) Planktic foraminiferal $\delta^{18}O$ (species *G. bulloides*) record from core MD95-2042 (10, 15). (*C*) Benthic foraminiferal $\delta^{18}O$ record from core MD95-2042 (15). (*D*) As Fig. 2*D*. Both foraminiferal $\delta^{18}O$ records are plotted on reversed scales and shown without and with ice volume correction (IVC, *Materials and Methods*). Grey bars with labels indicate the Younger Dryas and Heinrich and Heinrich-like stadials. Numbers in *A* indicate Dansgaard–Oeschger events. Labels in *D* indicate Antarctic Isotope Maximum events occurring during Heinrich and Heinrich-like stadials.

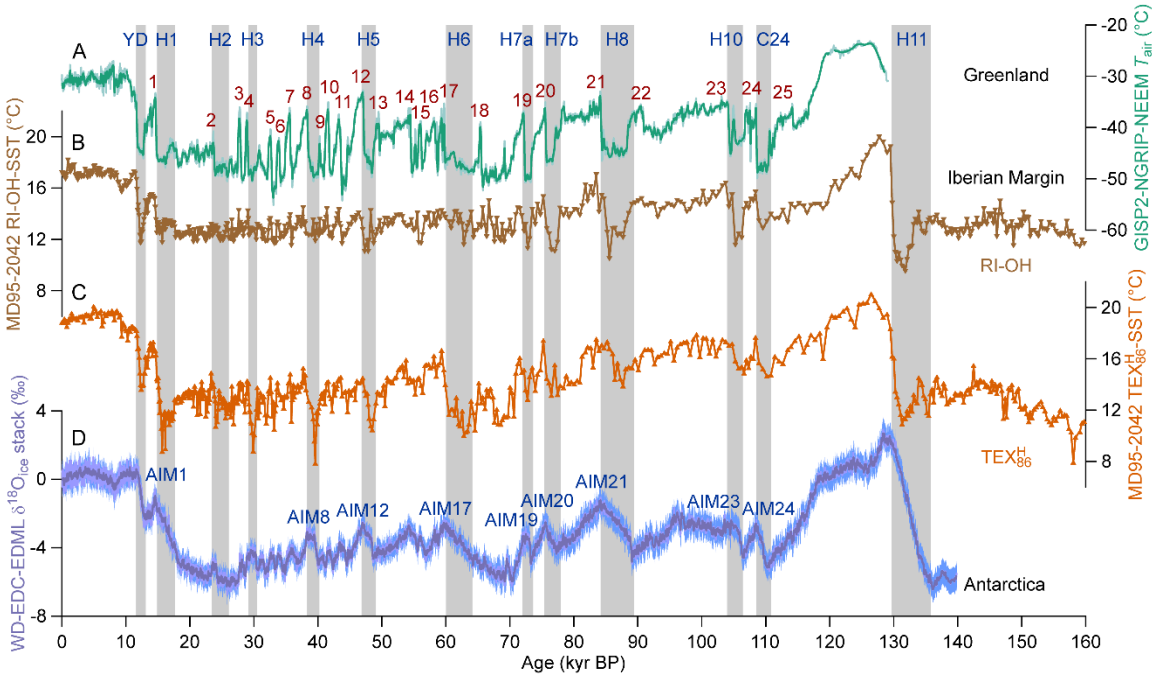

Fig. S2. Relationships between alternative biomarker-based Iberian Margin SST records and Greenland and Antarctic T_{air} records during the last 160 ky. (*A*) As Fig. 2*A*. (*B*) RI-OH-SST record from core MD95-2042 (*Materials and Methods*; partly published in ref. 21). (*C*) TEX_{86}^{H}-SST record from core MD95-2042 (*Materials and Methods*; partly published in ref. 21). (*D*) As Fig. 2*D*. Grey bars with labels indicate the Younger Dryas and Heinrich and Heinrich-like stadials. Numbers in *A* indicate Dansgaard–Oeschger events. Labels in *D* indicate Antarctic Isotope Maximum events occurring during Heinrich and Heinrich-like stadials.

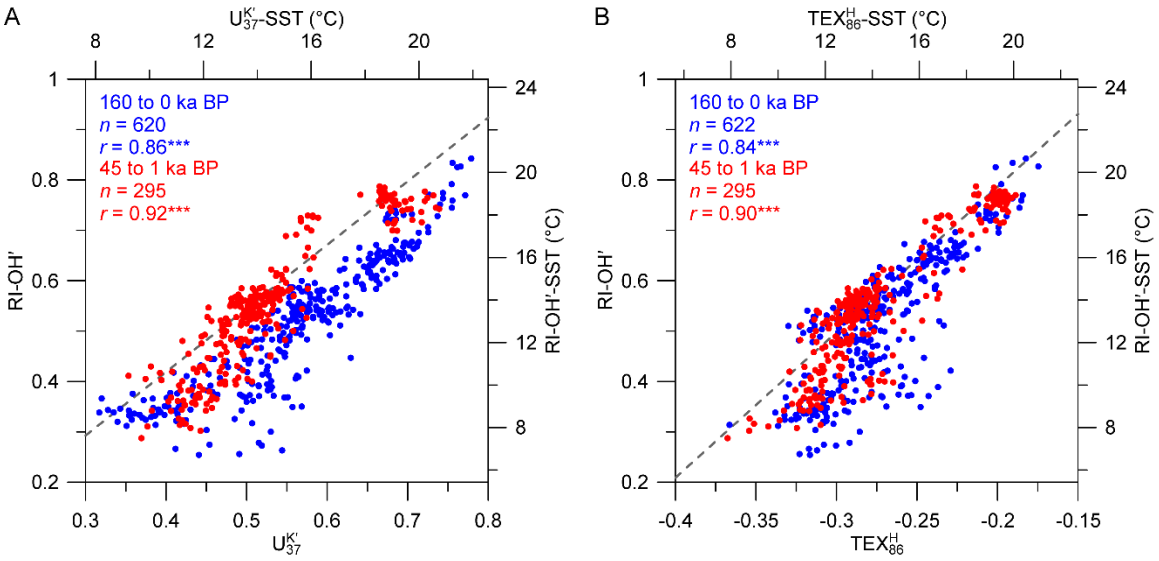

Fig. S3. Correlation between RI-OH′ and the two most established biomarker-based SST proxies for the Iberian Margin core MD95-2042. (*A*) Correlation between RI-OH′ and $U^{K'}_{37}$. (*B*) Correlation between RI-OH′ and TEX_{86}^{H}. Proxy value scales are shown with their conversions into SST scales based on the following global calibrations: SST = (RI-OH′ + 0.029)/0.0422 (23), SST = 29.876 × $U^{K'}_{37}$ − 1.334 (27), and SST = 68.4 × TEX_{86}^{H} − 33.0 (19). The grey dashed line represents the 1:1 line for SST values. Blue and red symbols represent data points previously published in ref. 21 and new data points from this study covering the 45 to 1 ka BP period, respectively. The 99.9% statistical significance level ($p < 0.001$ from a non-parametric method that accounts for serial correlation; ref. 132) is coded as ***.

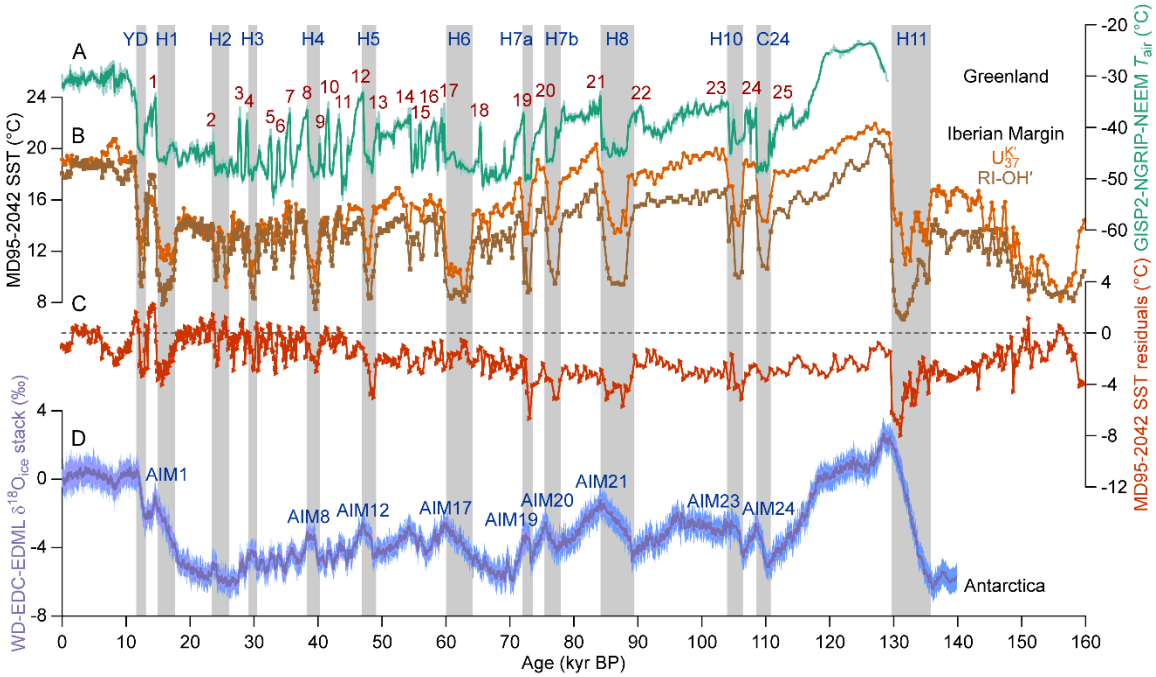

Fig. S4. Comparisons of two biomarker-based Iberian Margin SST records over the last 160 ky. (*A*) As Fig. 2*A*. (*B*) RI-OH′-SST (partly published in ref. 21) and $U^{K'}_{37}$-SST (19, 21) records from core MD95-2042 (*Materials and Methods*). (*C*) Difference between RI-OH′-SSTs and $U^{K'}_{37}$-SSTs from core MD95-2042. (*D*) As Fig. 2*D*. Grey bars with labels indicate the Younger Dryas and Heinrich and Heinrich-like stadials. Numbers in *A* indicate Dansgaard–Oeschger events. Labels in *D* indicate Antarctic Isotope Maximum events occurring during Heinrich and Heinrich-like stadials.

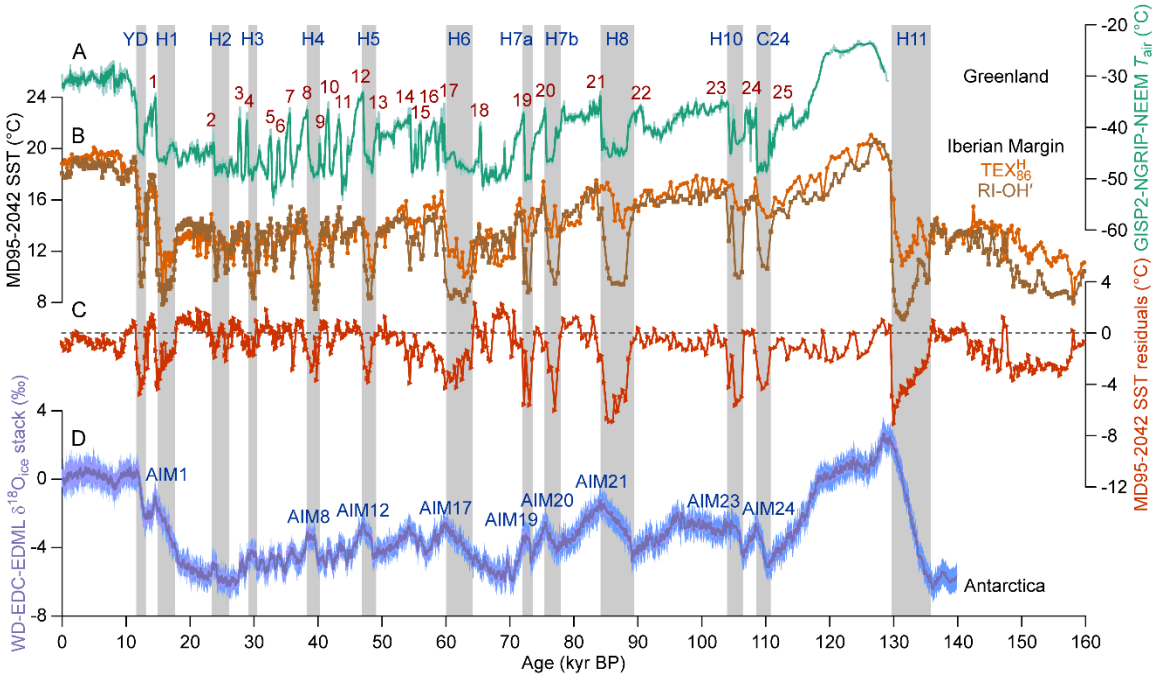

Fig. S5. As Fig. S4, but with RI-OH′-SSTs compared with TEX_{86}^{H}-SSTs for core MD95-2042. Both tetraether-based SST records from core MD95-2042 in *B* are partly published in ref. 21.

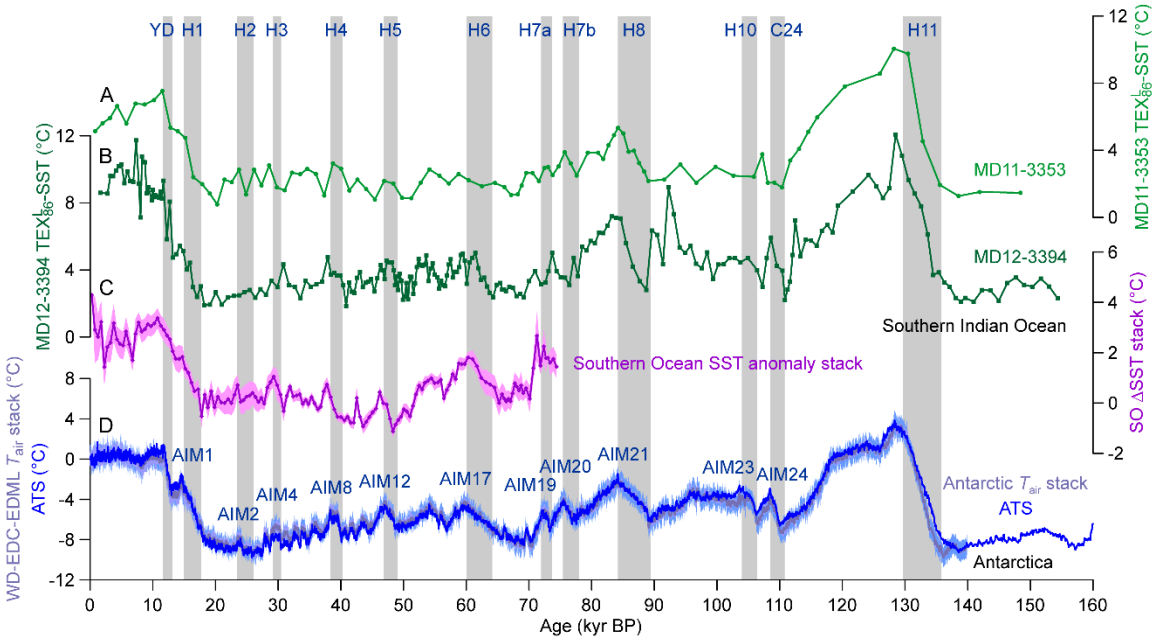

Fig. S6. Southern Ocean SST record comparisons with Antarctic T_{air} stacks. (*A*) TEX_{86}^{L}-SST record from core MD11-3353 (Southern Indian Ocean; ref. 58). (*B*) TEX_{86}^{L} record from core MD12-3394 (Southern Indian Ocean; ref. 58). (*C*) Southern Ocean SST anomaly (ΔSST) stack with its stacking error (59). (*D*) Antarctic stack of the T_{air} records from EDC (98, 133), EDML (81, 98), and WD (100, 134, 135) over the 140 to 0 ka BP period with its 2σ confidence interval (*Materials and Methods*). The Antarctic Temperature Stack (ATS) generated by ref. 71 is also shown in *D* for comparison. Grey bars with labels indicate the Younger Dryas and Heinrich and Heinrich-like stadials. Labels in *D* indicate Antarctic Isotope Maximum events occurring during Heinrich and Heinrich-like stadials. All records are on the ice-core chronology adopted in this study.

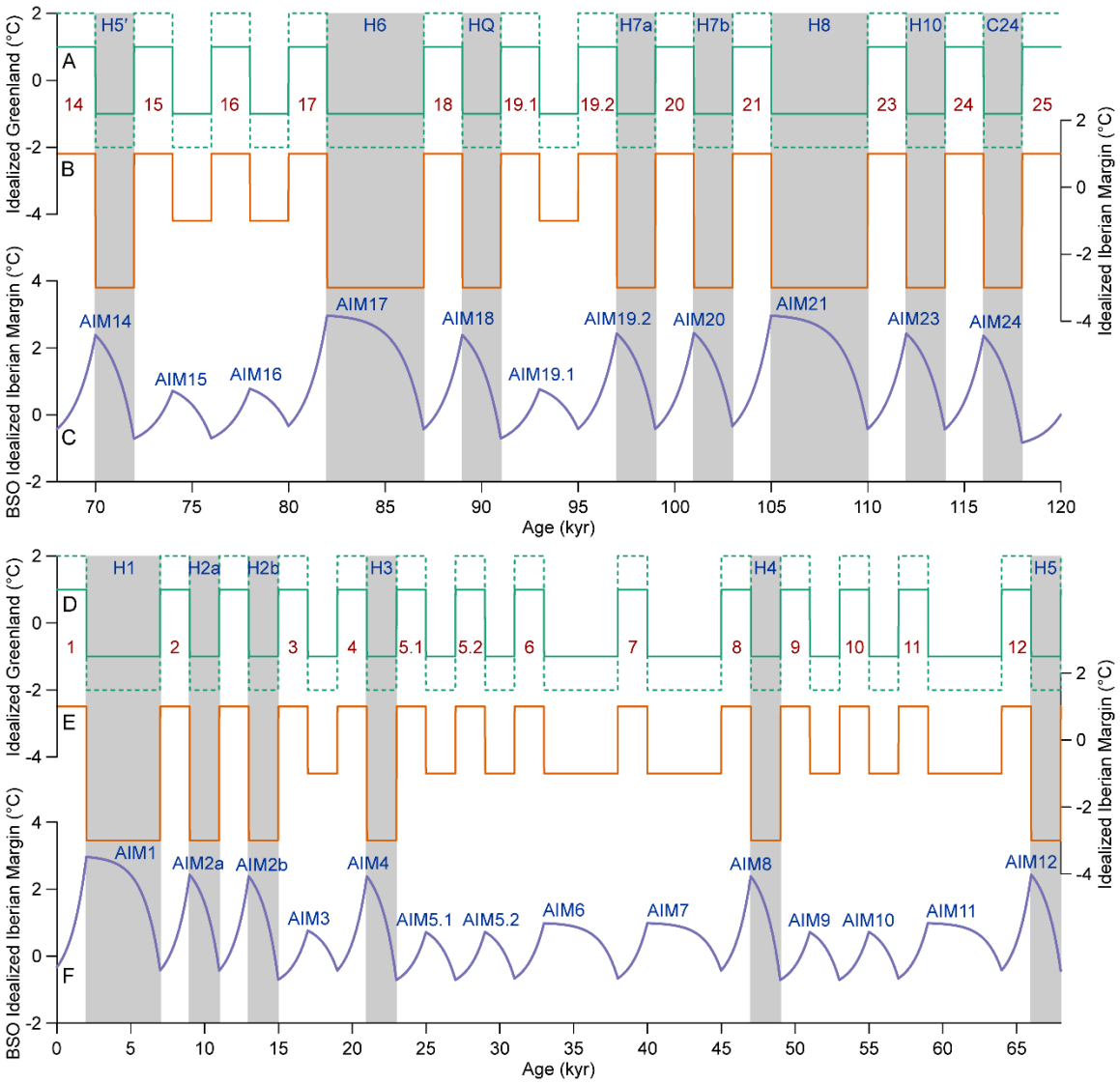

Fig. S7. Idealized Northern and Southern Hemisphere temperature records. (*A*) and (*D*) Idealized Greenland records with DO stadial coolings of –2 °C (solid line) and –4 °C (dashed line). (*B*) and (*E*) Idealized Iberian Margin record. (*C*) and (*F*) Idealized Antarctic temperature record as a bipolar seesaw model output generated from the idealized Iberian Margin record in *B* and *E* similarly to bipolar seesaw model outputs in Fig. 4. Grey bars with labels indicate Heinrich and Heinrich-like stadials. Numbers in *A* and *D* indicate Dansgaard–Oeschger events. Labels in *C* and *F* indicate Antarctic Isotope Maximum (AIM) events.

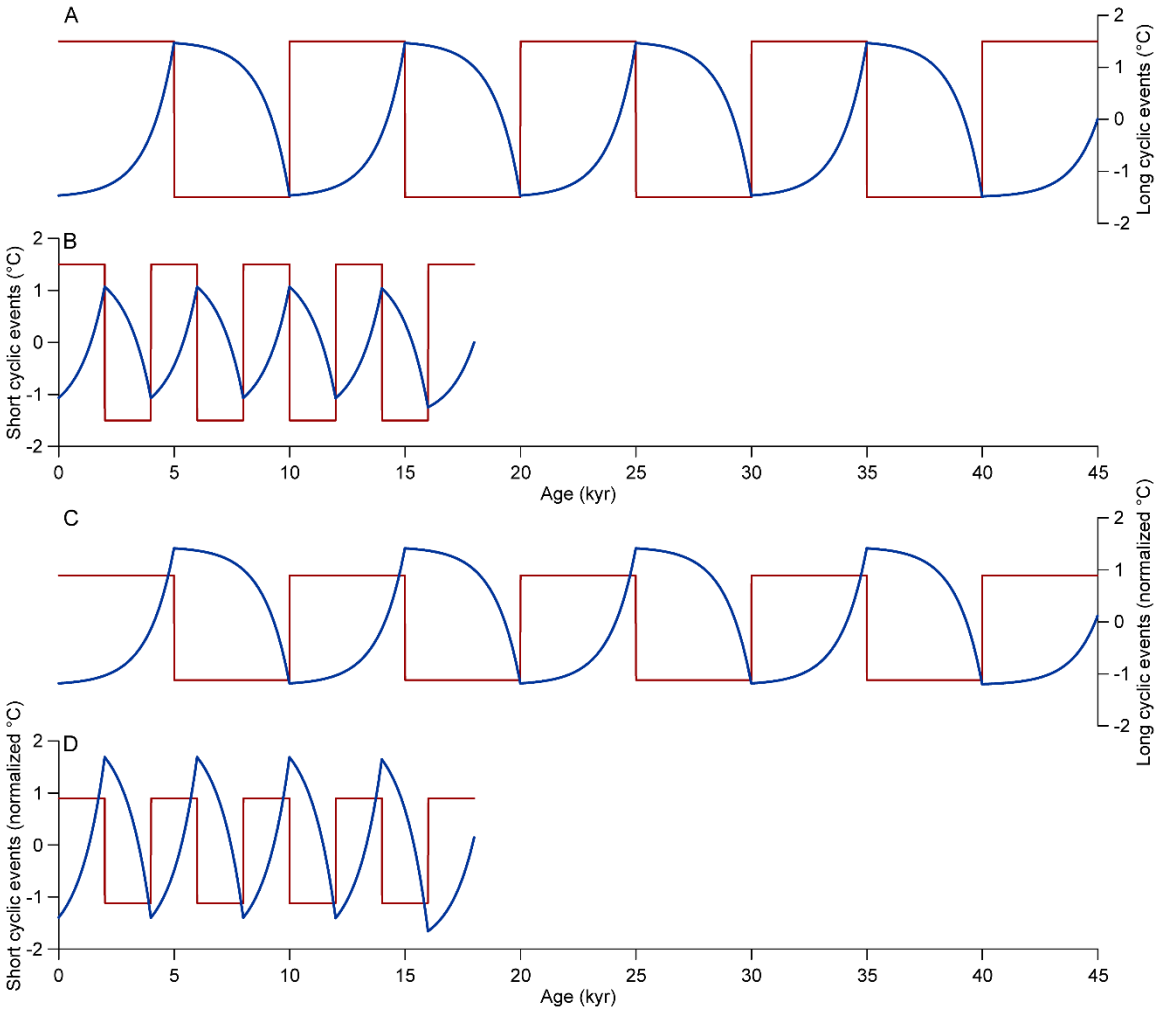

Fig. S8. Cyclic Northern and Southern Hemisphere temperature records. (*A*) Cycles of 5,000 y. (*B*) Cycles of 2,000 y, both time series have an amplitude of 3 °C. (*C*) Same as *A*, but with time series normalized to zero means and unit standard deviations. (*D*) Same as *B*, but with time series normalized to zero means and unit standard deviations. Northern and Southern Hemisphere temperature records are shown in red and blue, respectively. Southern Hemisphere temperature records are bipolar seesaw model outputs from the corresponding Northern Hemisphere temperature records.

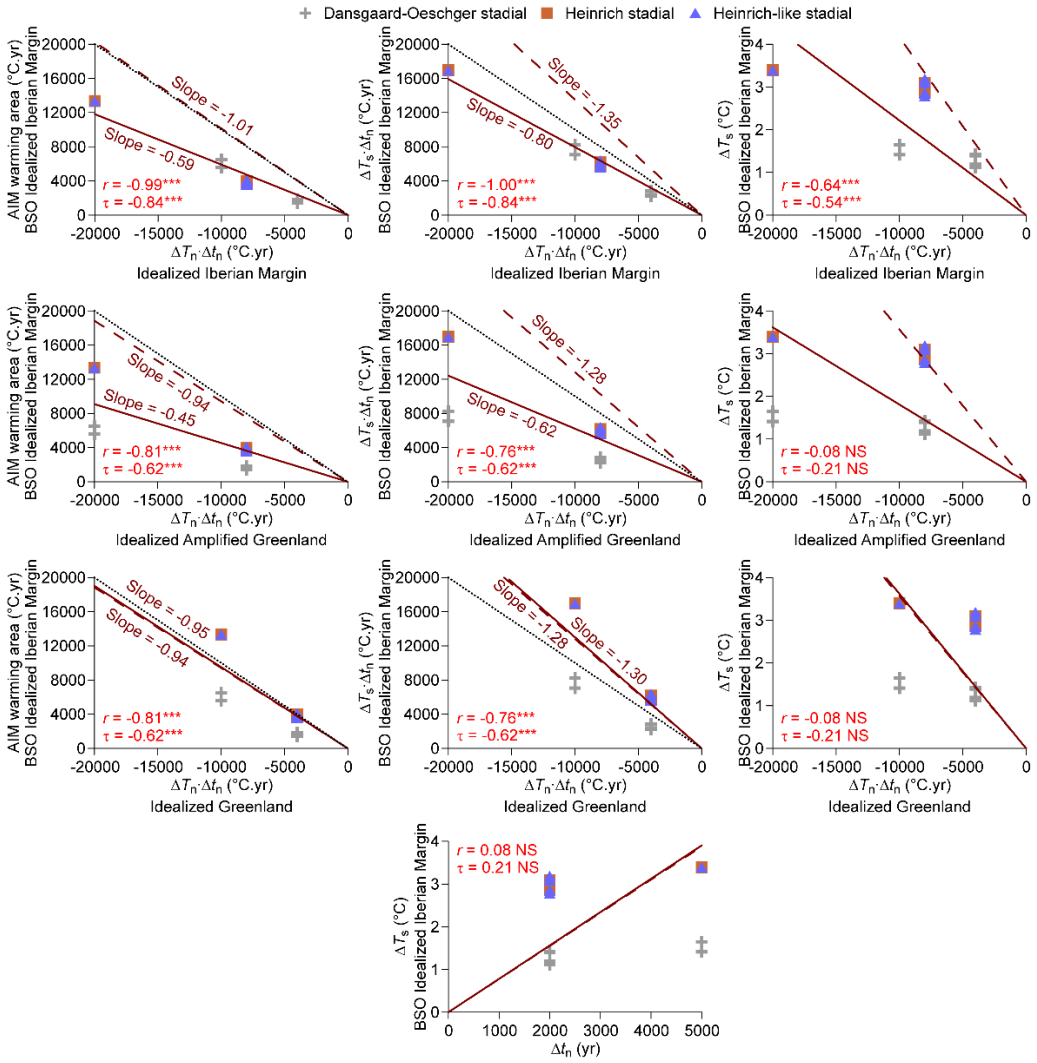

Fig. S9. Comparison of four different Southern versus Northern Hemisphere diagrams from idealized temperature records shown in Fig. S7. The Southern versus Northern Hemisphere diagrams are Antarctic Isotope Maximum (AIM) warming areas (see Fig. S7 *C* and *F*) versus $\Delta T_n \cdot \Delta t_n$ (left column), $\Delta T_s \cdot \Delta t_n$ versus $\Delta T_n \cdot \Delta t_n$ (middle column except the bottom), ΔT_s versus $\Delta T_n \cdot \Delta t_n$ (right column), and ΔT_s versus Δt_n (bottom). The Northern Hemisphere records used for all Southern versus Northern Hemisphere diagrams used are the idealized Iberian Margin temperature record (1st line), the idealized Greenland temperature record with ΔT_n values of –4 °C (2nd line), and the idealized Greenland temperature record with ΔT_n values of –2 °C (3rd line). The Southern Hemisphere record used in all cases is the bipolar seesaw model output from the idealized Iberian Margin temperature record. Antarctic Isotope Maximum events with Heinrich and Heinrich-like stadials are distinguished from Antarctic Isotope Maximum events with other Dansgaard–Oeschger stadials. The plotted regression lines have intercepts forced to 0 and consider errors in both coordinates (*Materials and Methods*). Dashed and solid lines represent linear regression scenarios with and without time series normalization to zero means and unit standard deviations, respectively. Regression slope values are provided for AIM warming areas versus $\Delta T_n \cdot \Delta t_n$ and $\Delta T_s \cdot \Delta t_n$ versus $\Delta T_n \cdot \Delta t_n$ diagrams. Dotted lines in AIM warming areas versus $\Delta T_n \cdot \Delta t_n$ and $\Delta T_s \cdot \Delta t_n$ versus $\Delta T_n \cdot \Delta t_n$ diagrams indicate –1:1 lines. Pearson's *r* coefficients and Kendall's τ rank coefficients are also shown, with their significance levels coded as follows: NS, not significant and $p > 0.05$; and ***, $p < 0.001$.

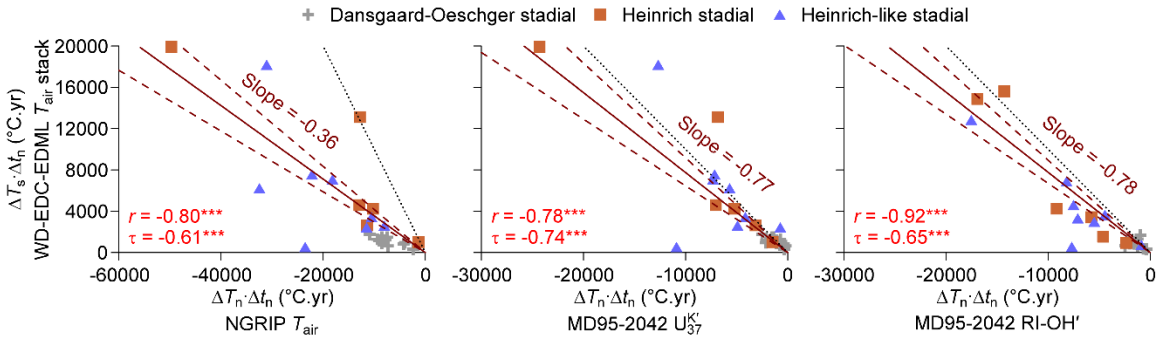

Fig. S10. Comparison of regression slopes for $\Delta T_s \cdot \Delta t_n$ versus $\Delta T_n \cdot \Delta t_n$ diagrams from non-normalized temperature records. Only the end-member scenario that best depicts the thermal bipolar seesaw (Scenario 1; see Text S8, above) is shown here. The Northern Hemisphere records used are the NGRIP T_{air} record (left) plotted in Fig. 2*A* and the Iberian Margin core MD95-2042 RI-OH′-SST (right) and $U^{K'}_{37}$-SST (middle) records plotted in Fig. 2 *B* and *C*. The Southern Hemisphere record used in all cases is an Antarctic stack of the T_{air} records from EDC (98, 133), EDML (81, 98), and WD (100, 134, 135) over the 140 to 0 ka BP period (*Materials and Methods*). Antarctic Isotope Maximum events with Heinrich and Heinrich-like stadials are distinguished from Antarctic Isotope Maximum events with other Dansgaard–Oeschger stadials. Solid lines represent regression lines with intercepts forced to 0 and which consider errors in both coordinates (*Materials and Methods*). Regression slope values are provided for each diagram. Dashed lines represent 95% confidence intervals of the regression slopes from 1,000 Monte Carlo iterations (*Materials and Methods*). For the sake of readability, error bars for individual data points are omitted. Dotted lines indicate –1:1 lines. Pearson's *r* coefficients and Kendall's τ rank coefficients are also shown, with their 99.9% significance levels coded as ***.

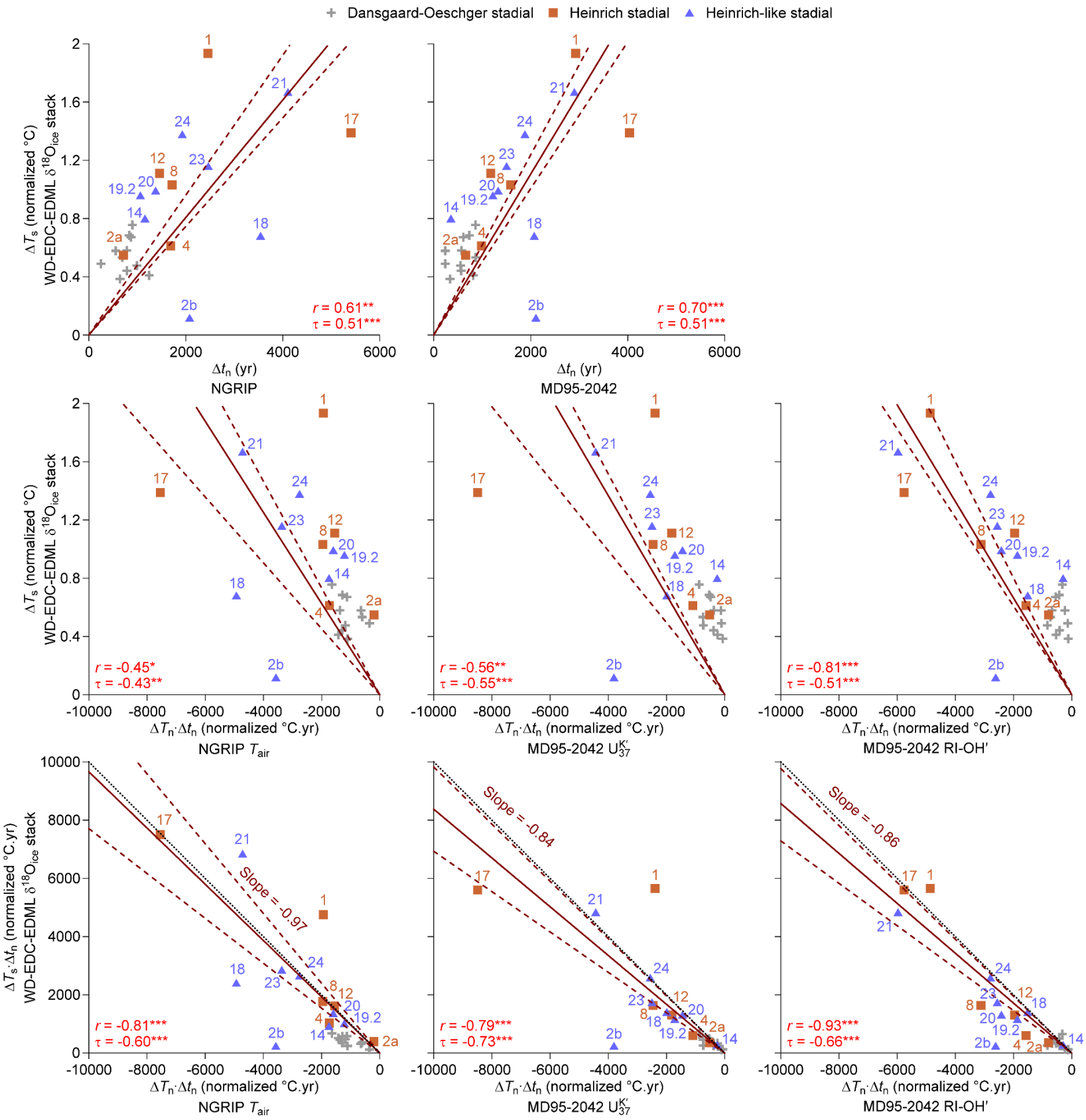

Fig. S11. The relationship between Southern and Northern Hemisphere climate events from the perspectives of normalized Greenland T_{air} and biomarker-based Iberian Margin SST records. Only the end-member scenario that best depicts the thermal bipolar seesaw (Scenario 1; see Text S8, above) is shown here. The Southern versus Northern Hemisphere diagrams are ΔT_s versus Δt_n (top line), ΔT_s versus $\Delta T_n \cdot \Delta t_n$ (middle line), and $\Delta T_s \cdot \Delta t_n$ versus $\Delta T_n \cdot \Delta t_n$ (bottom line). The Northern Hemisphere records used are the NGRIP T_{air} record (left column) and the Iberian Margin core MD95-2042 $U^{K'}_{37}$-SST (middle column) and RI-OH′-SST (right column) records, which all have been centered to zero means and normalized to unit standard deviations over the 129 to 0 ka BP period. A single set of Δt_n values is used for the Iberian Margin. The Southern Hemisphere record used in all cases is an Antarctic stack of the $\delta^{18}O_{ice}$ records from EDC (98, 133), EDML (81, 98), and WD (100, 134, 135) over the 140 to 0 ka BP period (*Materials and Methods*). Labels indicate Dansgaard–Oeschger stadial-Antarctic Isotope Maximum pairs, as per refs. 81, 82, and 83. Antarctic Isotope Maximum events with Heinrich and Heinrich-like stadials are distinguished from Antarctic Isotope Maximum events with other Dansgaard–Oeschger stadials. Solid lines represent regression lines with intercepts forced to 0 and which consider errors in both coordinates (*Materials and Methods*). Dashed lines represent 95% confidence intervals of the regression slopes from 1,000 Monte Carlo iterations (*Materials and Methods*). For the sake of readability, error bars for individual data points are omitted. Dotted lines in $\Delta T_s \cdot \Delta t_n$ versus $\Delta T_n \cdot \Delta t_n$ diagrams indicate –1:1 lines. Pearson's *r* coefficients and Kendall's τ rank coefficients are also shown, with their significance levels coded as follows: *, $p < 0.05$; **, $p < 0.01$; and ***, $p < 0.001$.

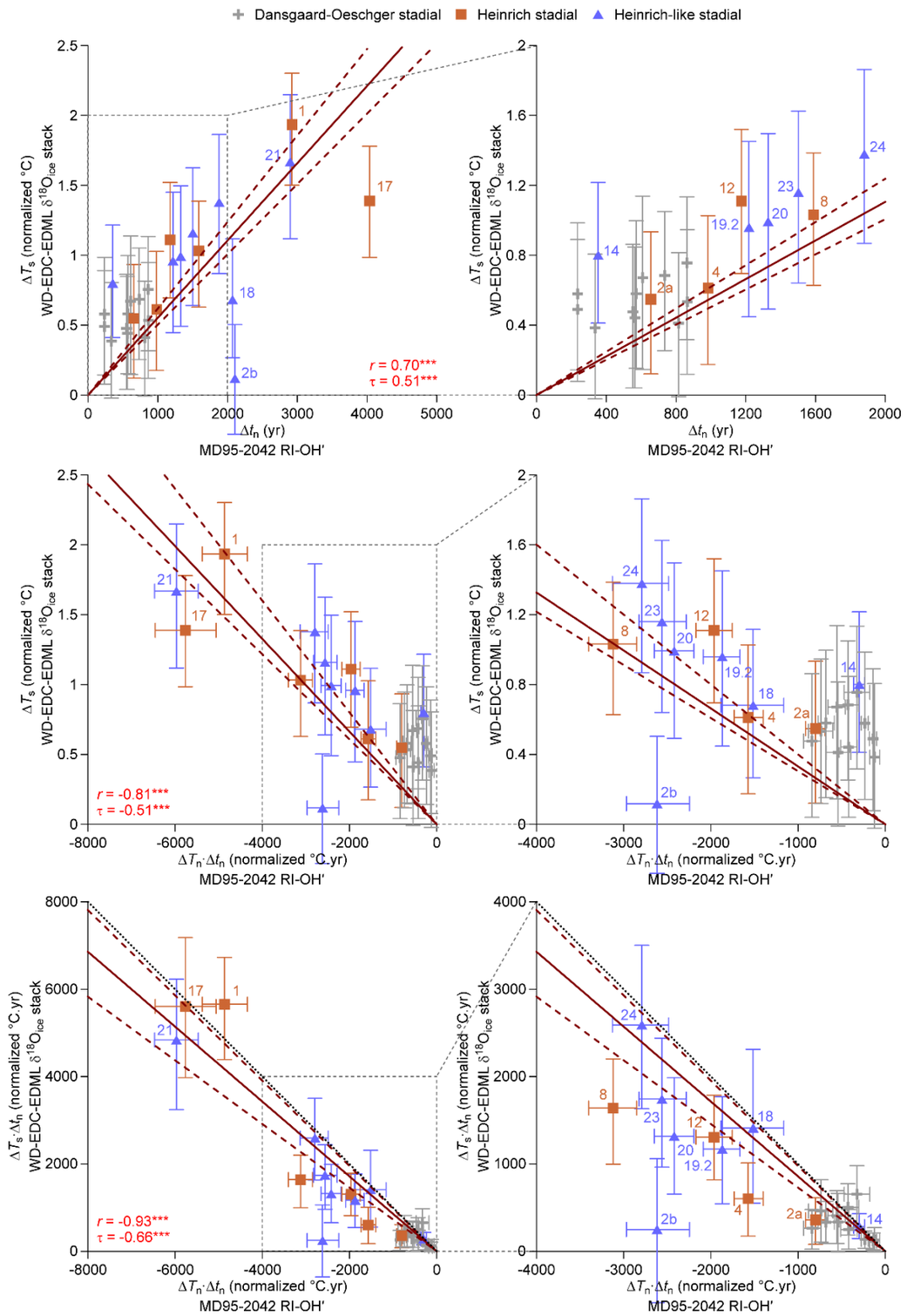

Fig. S12. The relationship between Southern and Northern Hemisphere climate events from the perspective of the Iberian Margin RI-OH′ SST record with all uncertainties shown. Only the end-member scenario that best depicts the thermal bipolar seesaw (Scenario 1; see Text S8, above) is shown here. The Southern versus Northern Hemisphere diagrams are ΔT_s versus Δt_n (top line), ΔT_s versus $\Delta T_n \cdot \Delta t_n$ (middle line), and $\Delta T_s \cdot \Delta t_n$ versus $\Delta T_n \cdot \Delta t_n$ (bottom line). The Southern Hemisphere record used in all cases is an Antarctic stack of the $\delta^{18}O_{ice}$ records from EDC (98, 133), EDML (81, 98), and WD (100, 134, 135) over the 140 to 0 ka BP period (*Materials and Methods*). Both Southern and Northern Hemisphere have been centered to zero means and normalized to unit standard deviations over the 129 to 0 ka BP period. Labels indicate Dansgaard–Oeschger stadial-Antarctic Isotope Maximum pairs, as per refs. 81, 82, and 83. Antarctic Isotope Maximum events with Heinrich and Heinrich-like stadials are distinguished from Antarctic Isotope Maximum events with other Dansgaard–Oeschger stadials. Error bars represent 95% confidence intervals from 1,000 Monte Carlo iterations (*Materials and Methods*). Solid lines represent regression lines with intercepts forced to 0 and which consider errors in both coordinates (*Materials and Methods*). Dashed lines represent 95% confidence intervals of the regression slopes from 1,000 Monte Carlo iterations (*Materials and Methods*). Dotted lines in $\Delta T_s \cdot \Delta t_n$ versus $\Delta T_n \cdot \Delta t_n$ diagrams indicate –1:1 lines. Pearson's *r* coefficients and Kendall's τ rank coefficients are also shown, with their 99.9% significance levels coded as ***.

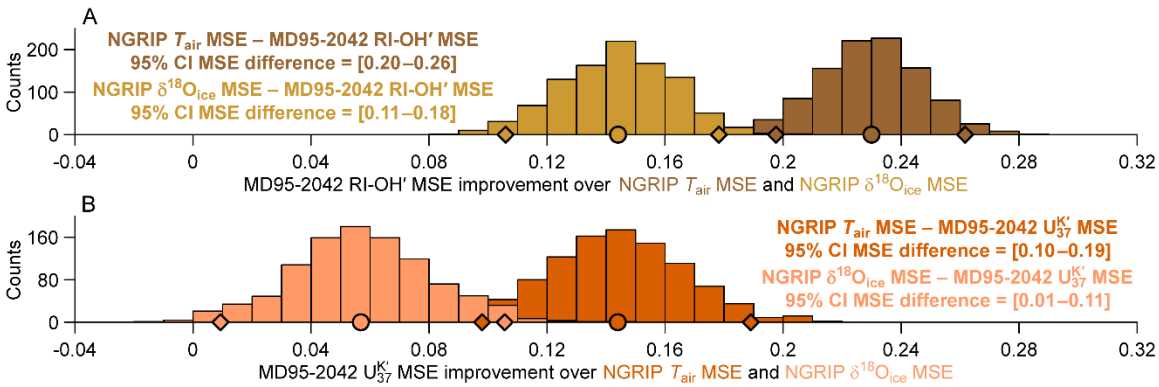

Fig. S13. Improvements in goodness-of-fit after a switch from Greenland to Iberian Margin paleothermometric records as bipolar seesaw model inputs. (*A*) Distributions of mean squared error (MSE) differences between bipolar seesaw model outputs from core MD95-2042 RI-OH′ and bipolar seesaw model outputs from NGRIP paleothermometric records following 1,000 Monte Carlo iterations (*Materials and Methods*). (*B*) Distributions of MSE differences between bipolar seesaw model outputs from core MD95-2042 $U^{K'}_{37}$ and bipolar seesaw model outputs from NGRIP paleothermometric records following 1,000 Monte Carlo iterations (*Materials and Methods*). The Southern Hemisphere reference record is an Antarctic stack of the $\delta^{18}O_{ice}$ records from EDC (98, 133), EDML (81, 98), and WD (100, 134, 135) over the 140 to 0 ka BP period (*Materials and Methods*). MSE differences are expressed in squared normalized °C and the bin size is 0.01 for all histograms. Diamonds and circles indicate 95% confidence intervals (CI) and medians from 1,000 Monte Carlo iterations, respectively (*Materials and Methods*).

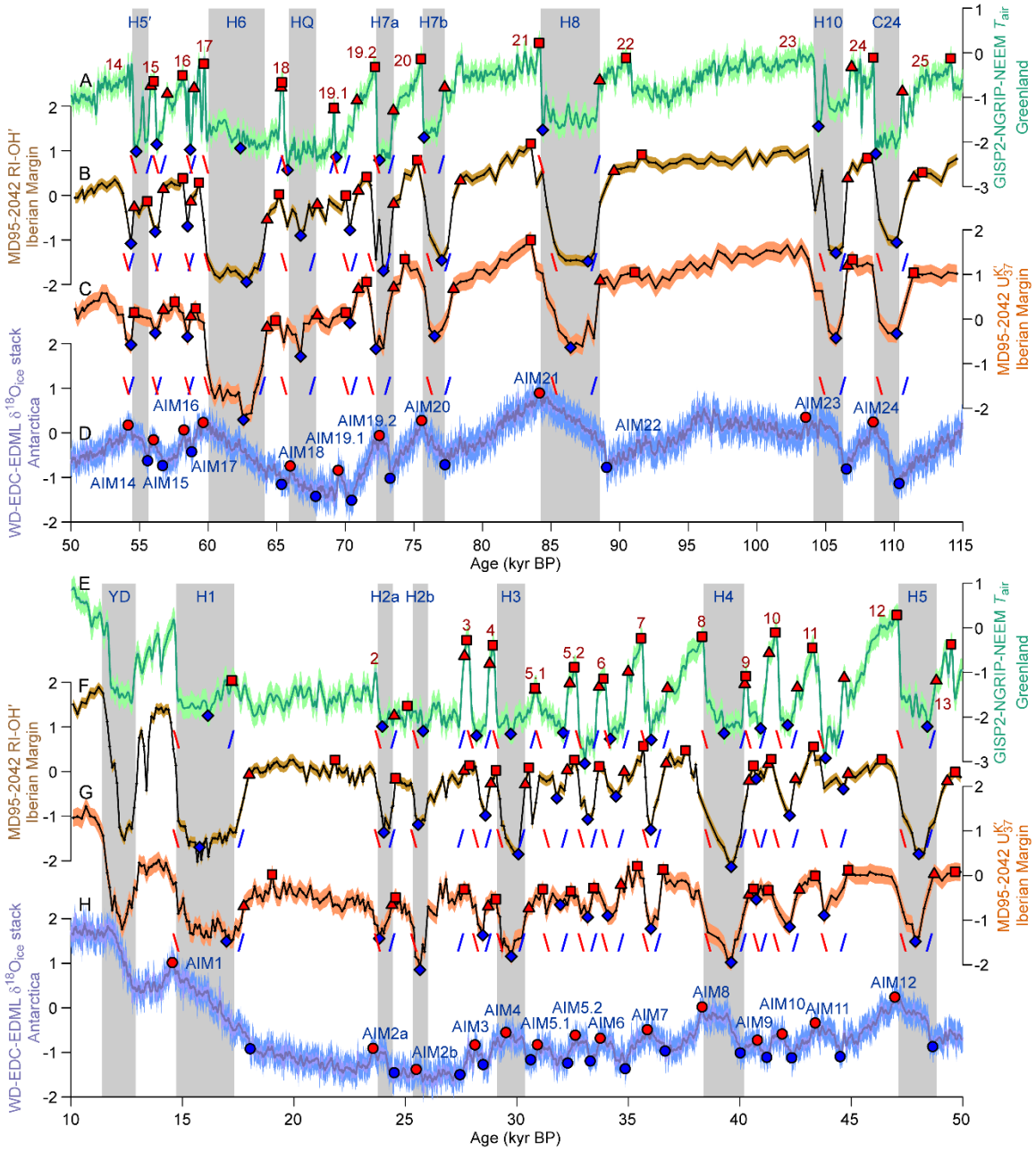

Fig. S14. Temperature amplitude and cold event delimitations. (*A*) and (*E*) As Fig. 2*A*. (*B*) and (*F*) As Fig. 2*B*. (*C*) and (*G*) As Fig. 2*C*. (*D*) and (*H*) As Fig. 2*D*. Shading around the temperature records represents their 95% confidence intervals from 1,000 Monte Carlo iterations (*Materials and Methods*). Blue and red symbols on the curves indicate temperature delimitations. Red triangles and red squares indicate Scenarios 1 and 2, respectively, in *A*–*C* and *E*–*G*. Blue and red circles in *D* and *H* indicate the onsets and optima of Antarctic Isotope Maximum events, respectively. Blue and red slashes below the curves indicate DO stadial delimitations. Grey bars with labels indicate the Younger Dryas and Heinrich and Heinrich-like stadials. Numbers in *A* and *E* indicate DO events. Labels in *D* and *H* indicate Antarctic Isotope Maximum events occurring during Heinrich and Heinrich-like stadials.

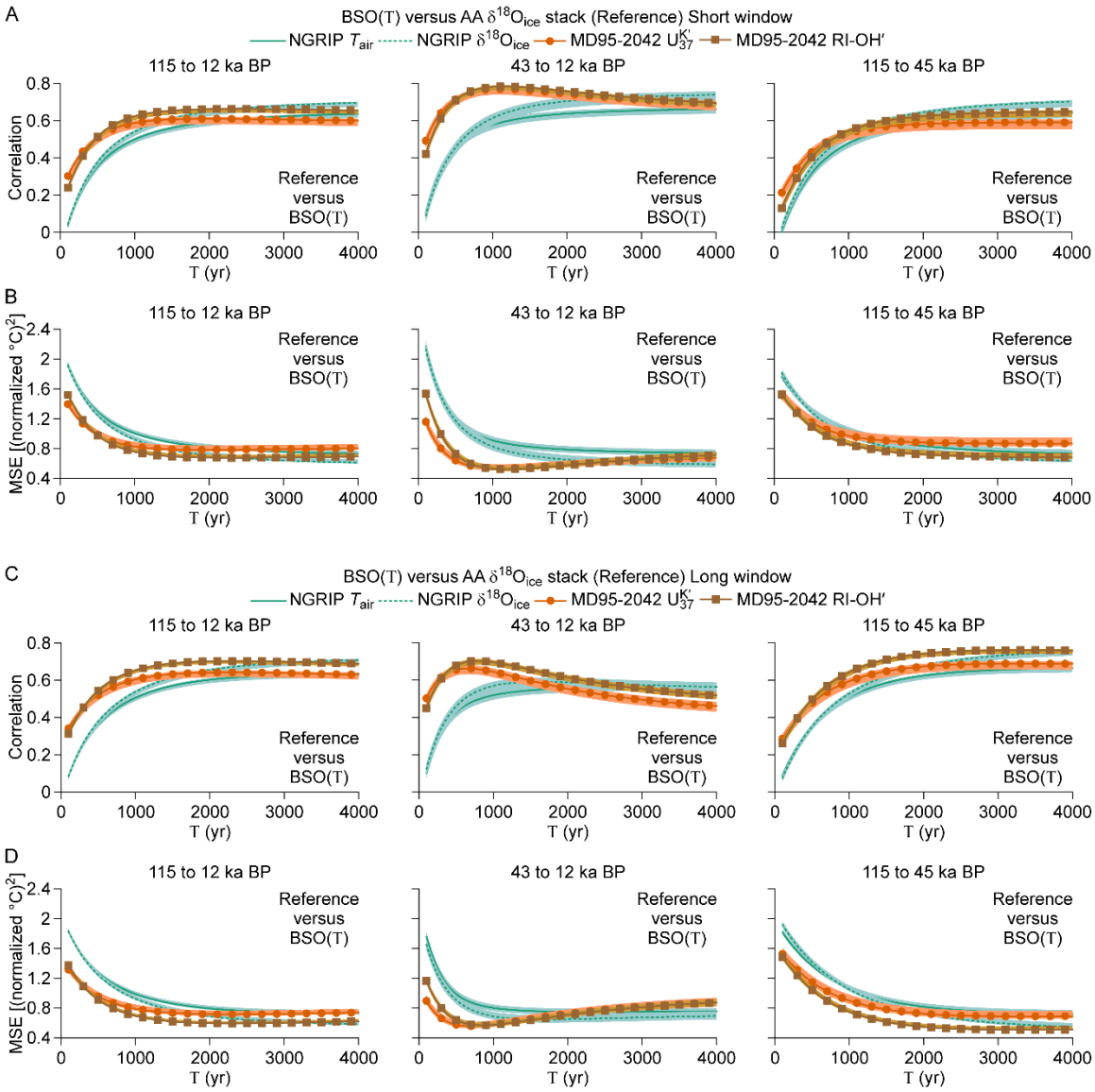

Fig. S15. Optimization of the time characteristic of the thermal bipolar seesaw model. (*A*) Correlation between bipolar seesaw output (BSO) record and a Southern Hemisphere reference record as a function of the time characteristic T using a band-pass filter with a 500- to 10,000-y window. (*B*) As *A*, but with mean squared error (MSE). (*C*) As *A*, but using a band-pass filter with a 500- to 16,000-y window. (*D*) As *C*, but with MSE. Shading represents 95% confidence intervals from 1,000 Monte Carlo iterations (*Materials and Methods*). The Southern Hemisphere reference record is an Antarctic stack of the $\delta^{18}O_{ice}$ records from EDC (98, 133), EDML (81, 98), and WD (100, 134, 135) over the 140 to 0 ka BP period (*Materials and Methods*).

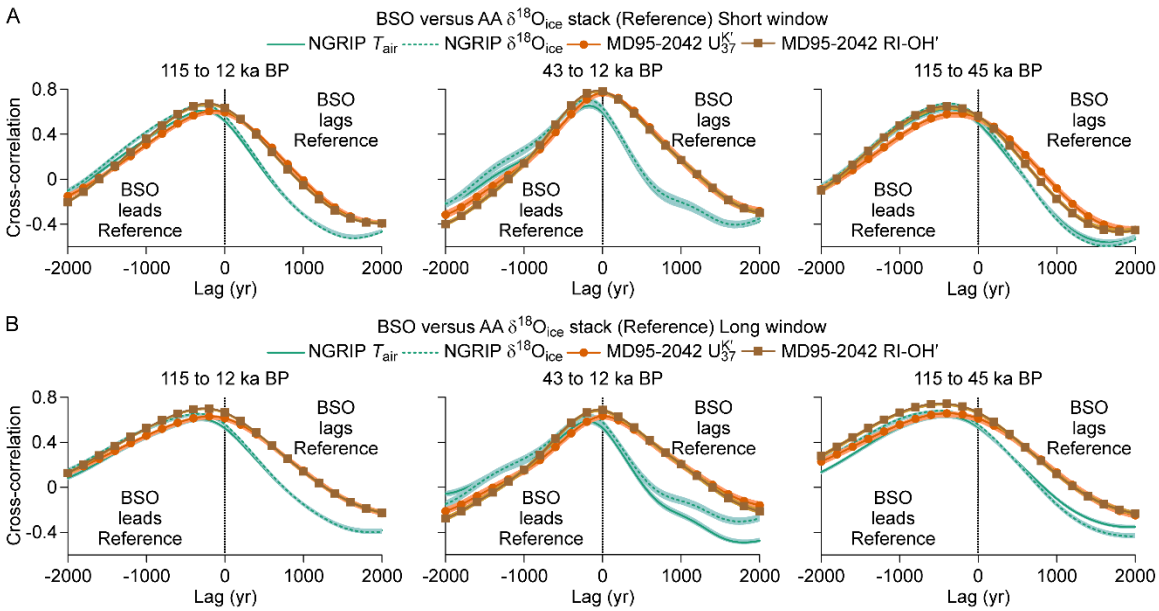

Fig. S16. Bipolar seesaw model output versus reference comparisons. (*A*) Bipolar seesaw output (BSO) record versus a Southern Hemisphere reference record using a band-pass filter with a 500- to 10,000-y window. (*B*) As *A*, but using a band-pass filter with a 500- to 16,000-y window. Shading represents 95% confidence intervals from 1,000 Monte Carlo iterations (*Materials and Methods*). The Southern Hemisphere reference record is an Antarctic stack of the $\delta^{18}O_{ice}$ records from EDC (98, 133), EDML (81, 98), and WD (100, 134, 135) over the 140 to 0 ka BP period (*Materials and Methods*).

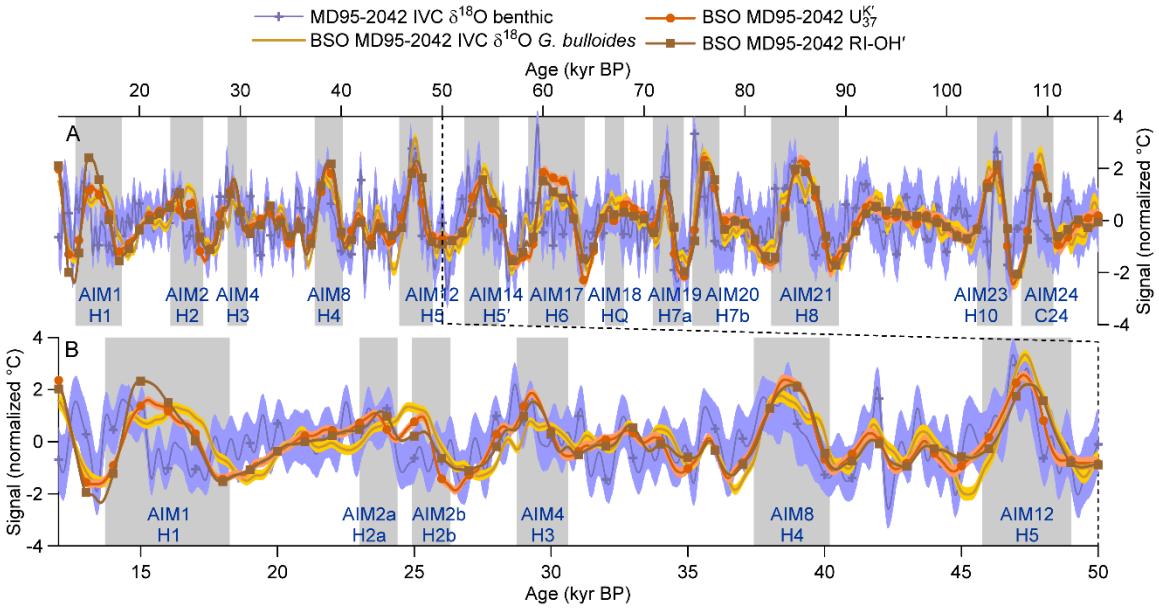

Fig. S17. Comparison between bipolar seesaw model outputs from several Iberian Margin SST records and an alternative Southern Hemisphere reference record. (*A*) 115 to 12 ka BP period using a band-pass filter with a 500- to 10,000-y window. (*B*) Close up of the 50 to 12 ka BP period. The opposite values of the ice-volume–corrected (IVC) foraminiferal $\delta^{18}O$ records are plotted and each bipolar seesaw output (BSO) and reference record has been centered to zero means and normalized to unit standard deviations over the 115 to 12 ka BP period in *A* and over the 50 to 12 ka BP period in *B* to facilitate the comparison (*Materials and Methods*). Shading around BSO and reference records in both *A* and *B* represents their 95% confidence intervals from 1,000 Monte Carlo iterations (*Materials and Methods*). The Southern Hemisphere reference record is the IVC benthic foraminiferal $\delta^{18}O$ record from core MD95-2042 as a surrogate of Antarctic temperatures (15). Grey bars with labels indicate Antarctic Isotope Maximum events with Heinrich and Heinrich-like stadials.

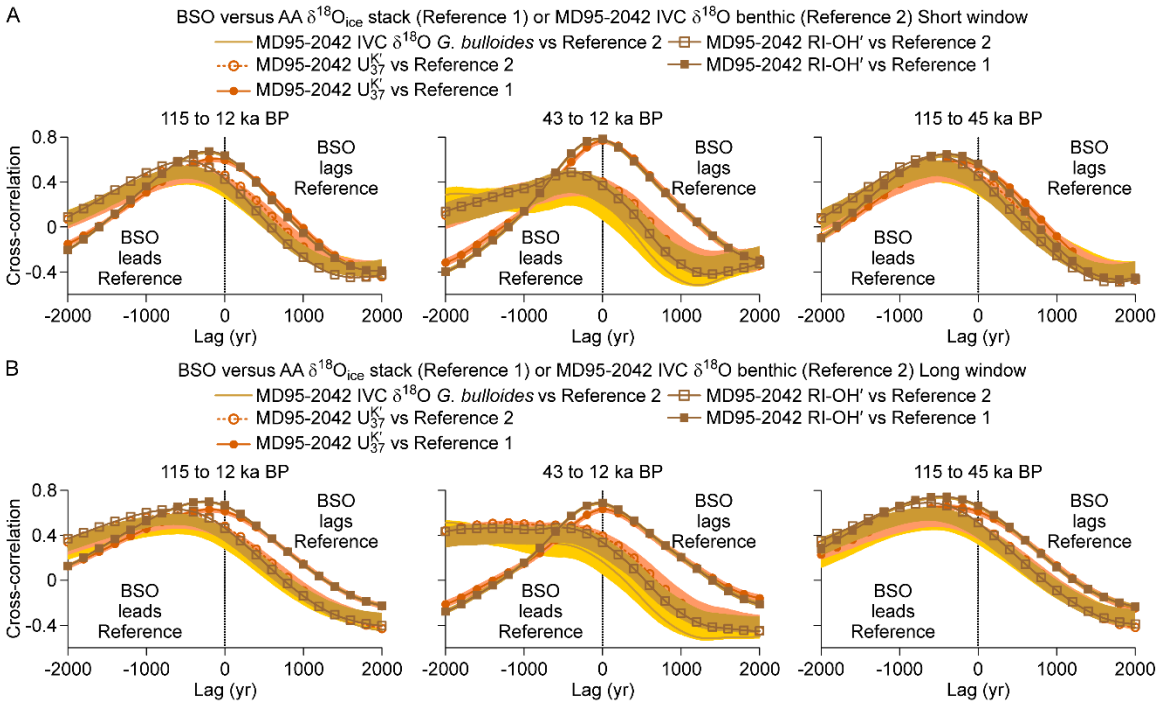

Fig. S18. Bipolar seesaw model output versus reference comparisons with the consideration of two independent Southern Hemisphere reference records. (*A*) Bipolar seesaw output (BSO) record versus two Southern Hemisphere reference records using a band-pass filter with a 500- to 10,000-y window. (*B*) As *A*, but using a band-pass filter with a 500- to 16,000-y window. Shading represents 95% confidence intervals from 1,000 Monte Carlo iterations (*Materials and Methods*). The Southern Hemisphere reference records are an Antarctic stack of the $\delta^{18}O_{ice}$ records from EDC (98, 133), EDML (81, 98), and WD (100, 134, 135) over the 140 to 0 ka BP period (*Materials and Methods*) and the ice-volume–corrected (IVC) benthic foraminiferal $\delta^{18}O$ record from core MD95-2042 as a surrogate of Antarctic temperatures (15). Opposite values of the IVC benthic foraminiferal $\delta^{18}O$ record are used when comparing with BSOs from biomarker-based SST records.

Table S1. Raw and calibrated (cal) ^{14}C ages and additional tie-points from the Iberian Margin core MD95-2042 used as inputs. All raw ^{14}C ages with their 1σ uncertainties were obtained during previous studies (109–111, 136, 137) and recalibrated with the Marine20 calibration curve (66) using the OxCal 4.4.2 software (138, 139). Assumed regional and temporal corrections of the marine reservoir age (ΔR) with their 1σ uncertainties are also provided. Given their relatively large uncertainties, ^{14}C ages indicated in italics are deemed imprecise. Cmbsf, centimeters below sea floor; SD, standard deviation; YD/PB, Younger Dryas/Preboreal transition; H6, Heinrich event 6; and N/A, not applicable.

Sample code	Depth (cmbsf)	^{14}C age (yr BP)	$\pm^{14}$C age (yr BP)	ΔR (y)	$\pm\Delta$R (y)	Median cal age (yr BP)	Mean cal age (yr BP)	SD cal age (yr BP)
Core top	0.0	N/A	N/A	N/A	N/A	0	0	100
YD/PB	305.0	N/A	N/A	N/A	N/A	11,650	11,650	100
OS-40272	458.5	13,550	60	350	200	15,003	14,977	339
OS-39555	459.5	13,500	55	350	200	14,925	14,898	340
OS-48338	481.0	13,820	70	350	200	15,389	15,383	307
OS-39556	538.5	14,700	55	350	200	16,532	16,526	282
OS-40273	539.5	14,650	65	350	200	16,470	16,465	288
OS-48339	560.5	15,110	80	350	200	17,041	17,038	295
OS-48340	640.5	16,380	90	–50	100	18,947	18,956	178
OS-40268	658.5	16,850	100	–50	100	19,495	19,496	212
OS-48341	740.5	18,820	100	–50	100	21,936	21,922	201
GifA100547	800.0	20,120	210	–50	100	23,331	23,332	271
OS-39557	841.5	20,900	110	–50	100	24,176	24,186	213
OS-40270	918.5	22,300	110	–50	100	25,729	25,719	168
OS-39558	921.5	22,300	130	–50	100	25,728	25,718	182
GifA100548	1,012.0	24,950	270	–50	100	28,331	28,330	321
OS-39559	1,019.5	24,900	120	–50	100	28,279	28,271	216
GifA100549	1,048.0	25,760	290	–50	100	29,203	29,214	334
OS-40271	1,078.5	26,200	120	–50	100	29,634	29,617	200
OS-39560	1,079.5	26,000	110	–50	100	29,433	29,438	197
GifA100550	1,175.0	29,030	390	–50	100	32,523	32,535	537
OS-39305	1,199.5	29,600	240	–50	100	33,308	33,292	351
OS-62137	1,203.0	29,660	140	–50	100	33,385	33,384	235
GifA100551	1,216.0	29,950	360	–50	100	33,669	33,646	414
GifA100552	1,267.0	32,410	420	–50	100	36,115	36,140	492
OS-39306	1,279.5	31,800	360	–50	100	35,486	35,485	401
OS-62133	1,283.0	32,270	190	–50	100	35,937	35,927	241
KIA14285	1,336.0	34,320	720	–50	100	38,423	38,400	846
OS-48342	1,340.5	33,740	430	–50	100	37,766	37,783	612
OS-62138	1,351.0	33,740	230	–50	100	37,726	37,749	413
OS-39307	1,361.5	35,300	460	–50	100	39,562	39,568	459
OS-39308	1,378.5	35,700	490	–50	100	39,915	39,926	445
KIA15625	1,404.0	36,010	600	–50	100	40,171	40,176	515
KIA14284	1,416.0	36,640	970	–50	100	40,661	40,648	742
GifA100554	1,439.0	37,700	680	–50	100	41,430	41,411	438
OS-62095	1,474.0	40,450	430	–50	100	42,884	42,940	341
OS-48343	*1,481.5*	*41,370*	*1120*	*–50*	*100*	*43,744*	*43,853*	*917*
GifA100555	*1,483.0*	*42,200*	*1100*	*–50*	*100*	*44,343*	*44,445*	*1,006*
OS-62102	*1,535.0*	*46,940*	*960*	*–50*	*100*	*49,000*	*49,224*	*1,496*
OS-48344	*1,540.5*	*45,200*	*1700*	*–50*	*100*	*47,538*	*47,979*	*2,279*
OS-62132	*1,546.0*	*45,200*	*770*	*–50*	*100*	*46,895*	*46,965*	*845*
GifA100556	*1,548.0*	*46,900*	*1800*	*–50*	*100*	*49,491*	*49,769*	*2,312*
OS-39309	*1,581.5*	*46,100*	>	N/A	N/A	N/A	N/A	N/A
OS-62103	*1,598.0*	*48,130*	*1400*	*–50*	*100*	*50,772*	*50,941*	*1,923*
End H6	1,783.0	N/A	N/A	N/A	N/A	59,800	59,800	100

Table S2. Outline of statistical result tables. GL, Greenland; IM, Iberian Margin; SH, Southern Hemisphere; NH, Northern Hemisphere; and N/A, not applicable.

Type of statistical analysis	Observed temperature records with and without normalization	Filtered and simulated temperature records 500- to 10,000-y window	Filtered and simulated temperature records 500- to 16,000-y window
Pearson and Kendall correlations for all events	Table S3	Table S7	Table S11
Monte Carlo comparisons of GL vs IM records	Table S4	Table S8	Table S12
Bootstrap comparisons of GL vs IM records	Table S5	Table S9	Table S13
Pearson and Kendall correlations for groups of events	Table S6	Table S10	Table S14
Comparisons of classical SH vs NH diagrams	Table S15	N/A	N/A
Bipolar seesaw goodness-of-fit	N/A	Table S16	Table S16
Monte Carlo comparisons of goodness-of-fit	N/A	Table S17	Table S17
Bipolar seesaw cross-correlations	N/A	Table S18	Table S18
Monte Carlo comparisons of cross-correlations	N/A	Table S19	Table S19

Table S3. Correlation results for Southern versus Northern Hemisphere diagrams using observed paleothermometric records. All *r* and τ values are reported above their associated *p*-values. $\Delta T_s \cdot \Delta t_n$ versus $\Delta T_n \cdot \Delta t_n$ diagrams consider temperature amplitudes for both hemispheres (ΔT_s and ΔT_n) and Northern Hemisphere (NH) cold event durations (Δt_n). ΔT_s versus Δt_n diagrams represent Southern Hemisphere (SH) temperature amplitudes versus NH cold event durations as shown in refs. 81, 82, 83, and 84. Both Scenarios 1 and 2 are considered (see *Materials and Methods* and Text S8, above). Correlations with the main Southern Hemisphere record are shown with bold text and numbers. Non-significant correlations are shown with grey numbers in italics. AA, Antarctic stack of EDC, EDML, and WD; ATS, Antarctic Temperature Stack (71); and IVC, ice-volume–corrected.

		Correlation coefficients and *p*-values for all DO-AIM pairs (*n* = 25)									
		$\Delta T_s \cdot \Delta t_n$ vs $\Delta T_n \cdot \Delta t_n$				ΔT_s vs $\Delta T_n \cdot \Delta t_n$				ΔT_s vs Δt_n	
		Pearson *r*		Kendall τ		Pearson *r*		Kendall τ		Pearson *r*	Kendall τ
SH record	NH record	1	2	1	2	1	2	1	2		
AA $\delta^{18}O_{ice}$ stack	**NGRIP**	**–0.81**	**–0.82**	**–0.60**	**–0.57**	**–0.45**	**–0.51**	**–0.43**	**–0.46**	**0.61**	**0.51**
	T_{air}	**< 0.001**	**< 0.001**	**< 0.001**	**< 0.001**	**0.023**	**0.009**	**0.002**	**< 0.001**	**0.001**	**< 0.001**
	MD95-2042	**–0.79**	**–0.86**	**–0.73**	**–0.72**	**–0.56**	**–0.66**	**–0.55**	**–0.55**	**0.70**	**0.51**
	$U^{K'}_{37}$	**< 0.001**	**< 0.001**	**< 0.001**	**< 0.001**	**0.004**	**< 0.001**	**< 0.001**	**< 0.001**	**< 0.001**	**< 0.001**
	MD95-2042	**–0.93**	**–0.93**	**–0.66**	**–0.71**	**–0.81**	**–0.80**	**–0.51**	**–0.52**	**0.70**	**0.51**
	RI-OH′	**< 0.001**	**< 0.001**	**< 0.001**	**< 0.001**	**< 0.001**	**< 0.001**	**< 0.001**	**< 0.001**	**< 0.001**	**< 0.001**
AA T_{air} stack	NGRIP	–0.80	–0.81	–0.61	–0.57	–0.45	–0.50	–0.42	–0.45	0.60	0.51
	T_{air}	< 0.001	< 0.001	< 0.001	< 0.001	0.024	0.011	0.003	0.001	0.001	< 0.001
	MD95-2042	–0.78	–0.86	–0.74	–0.71	–0.56	–0.66	–0.55	–0.55	0.70	0.50
	$U^{K'}_{37}$	< 0.001	< 0.001	< 0.001	< 0.001	0.004	< 0.001	< 0.001	< 0.001	< 0.001	< 0.001
	MD95-2042	–0.92	–0.92	–0.65	–0.69	–0.80	–0.79	–0.50	–0.51	0.70	0.50
	RI-OH′	< 0.001	< 0.001	< 0.001	< 0.001	< 0.001	< 0.001	< 0.001	< 0.001	< 0.001	< 0.001
ATS	NGRIP	–0.75	–0.75	–0.64	–0.62	–0.43	–0.45	–0.45	–0.40	0.60	0.51
	T_{air}	< 0.001	< 0.001	< 0.001	< 0.001	0.030	0.023	0.001	0.005	0.002	< 0.001
	MD95-2042	–0.70	–0.80	–0.80	–0.80	–0.54	–0.66	–0.52	–0.53	0.73	0.48
	$U^{K'}_{37}$	< 0.001	< 0.001	< 0.001	< 0.001	0.005	< 0.001	< 0.001	< 0.001	< 0.001	< 0.001
	MD95-2042	–0.90	–0.88	–0.75	–0.78	–0.83	–0.80	–0.58	–0.57	0.73	0.48
	RI-OH′	< 0.001	< 0.001	< 0.001	< 0.001	< 0.001	< 0.001	< 0.001	< 0.001	< 0.001	< 0.001
MD95-2042 IVC $\delta^{18}O$ benthic	NGRIP	–0.81	–0.79	–0.57	–0.55	*–0.32*	*–0.37*	*–0.19*	*–0.22*	0.49	0.30
	T_{air}	< 0.001	< 0.001	< 0.001	< 0.001	*0.118*	*0.066*	*0.201*	*0.130*	0.014	0.037
	MD95-2042	–0.84	–0.92	–0.69	–0.77	–0.55	–0.67	–0.41	–0.47	0.62	0.40
	$U^{K'}_{37}$	< 0.001	< 0.001	< 0.001	< 0.001	0.005	< 0.001	0.004	< 0.001	< 0.001	0.005
	MD95-2042	–0.92	–0.94	–0.74	–0.79	–0.72	–0.75	–0.43	–0.49	0.62	0.40
	RI-OH′	< 0.001	< 0.001	< 0.001	< 0.001	< 0.001	< 0.001	0.002	< 0.001	< 0.001	0.005
	MD95-2042	–0.79	–0.88	–0.76	–0.69	–0.52	–0.61	–0.41	–0.39	0.62	0.40
	IVC $\delta^{18}O$ *G. bulloides*	< 0.001	< 0.001	< 0.001	< 0.001	0.007	0.001	0.004	0.005	< 0.001	0.005

Table S4. Monte Carlo results for correlation comparisons between different observed Northern Hemisphere paleothermometric records. Each column indicates the 2.5th and 97.5th percentiles that define 95% confidence intervals. Negative differences indicate weaker correlations when using Greenland paleothermometric records than when using Iberian Margin paleothermometric records. Correlations with the main Southern Hemisphere record are shown with bold text and numbers. Non-significant correlation differences are shown with grey numbers in italics. "NGRIP T_{air} bis" refers to Monte Carlo results based on the published uncertainty in ΔT_n values for NGRIP T_{air} (1σ = 1.5 °C; ref. 95) rather than on 1,000 perturbed NGRIP T_{air} records (*Materials and Methods*). AA, Antarctic stack of EDC, EDML, and WD; and IVC, ice-volume–corrected.

			95% confidence intervals of changes in absolute coefficient correlation values for all DO-AIM pairs											
			$\Delta T_s \cdot \Delta t_n$ vs $\Delta T_n \cdot \Delta t_n$				ΔT_s vs $\Delta T_n \cdot \Delta t_n$				ΔT_s vs Δt_n			
SH record	NH records	Scenario	Pearson *r*		Kendall τ		Pearson *r*		Kendall τ		Pearson *r*		Kendall τ	
AA $\delta^{18}O_{ice}$ stack	**From MD95-2042 $U^{K'}_{37}$**	**1**	***–0.11***	***0.11***	***–0.26***	***0.03***	***–0.24***	***0.03***	***–0.27***	***0.07***	**–0.15**	**–0.01**	***–0.13***	***0.10***
	to NGRIP T_{air}	**2**	***–0.17***	***0.03***	***–0.27***	***< 0.01***	**–0.28**	**–0.01**	***–0.23***	***0.05***	**–0.15**	**–0.01**	***–0.13***	***0.10***
	From MD95-2042 $U^{K'}_{37}$	**1**	***–0.13***	***0.12***	***–0.27***	***0.02***	***–0.25***	***0.05***	***–0.28***	***0.07***	**–0.15**	**–0.01**	***–0.13***	***0.10***
	to NGRIP T_{air} bis	**2**	***–0.18***	***0.03***	**–0.27**	**–0.01**	**–0.28**	**< –0.01**	***–0.25***	***0.05***	**–0.15**	**–0.01**	***–0.13***	***0.10***
	From MD95-2042 RI-OH′	**1**	**–0.25**	**–0.03**	***–0.24***	***0.07***	**–0.47**	**–0.18**	***–0.27***	***0.07***	**–0.15**	**–0.01**	***–0.13***	***0.10***
	to NGRIP T_{air}	**2**	**–0.22**	**–0.05**	***–0.27***	***0.01***	**–0.41**	**–0.13**	***–0.27***	***0.05***	**–0.15**	**–0.01**	***–0.13***	***0.10***
	From MD95-2042 RI-OH′	**1**	**–0.27**	**–0.03**	***–0.25***	***0.05***	**–0.48**	**–0.16**	***–0.30***	***0.07***	**–0.15**	**–0.01**	***–0.13***	***0.10***
	to NGRIP T_{air} bis	**2**	**–0.25**	**–0.05**	***–0.27***	***0.01***	**–0.41**	**–0.12**	***–0.26***	***0.05***	**–0.15**	**–0.01**	***–0.13***	***0.10***
AA T_{air} stack	From MD95-2042 $U^{K'}_{37}$	1	*–0.11*	*0.12*	*–0.26*	*0.04*	*–0.23*	*0.03*	*–0.26*	*0.08*	–0.16	–0.02	*–0.13*	*0.10*
	to NGRIP T_{air}	2	*–0.17*	*0.03*	–0.27	0.00	–0.29	–0.02	*–0.23*	*0.05*	–0.16	–0.02	*–0.13*	*0.10*
	From MD95-2042 $U^{K'}_{37}$	1	*–0.13*	*0.13*	*–0.27*	*0.03*	*–0.25*	*0.05*	*–0.27*	*0.07*	–0.16	–0.02	*–0.13*	*0.10*
	to NGRIP T_{air} bis	2	*–0.18*	*0.03*	–0.27	–0.01	–0.29	–0.01	*–0.25*	*0.05*	–0.16	–0.02	*–0.13*	*0.10*
	From MD95-2042 RI-OH′	1	–0.25	–0.03	*–0.23*	*0.07*	–0.47	–0.19	*–0.27*	*0.07*	–0.16	–0.02	*–0.13*	*0.10*
	to NGRIP T_{air}	2	–0.22	–0.06	*–0.27*	*0.01*	–0.42	–0.14	*–0.25*	*0.06*	–0.16	–0.02	*–0.13*	*0.10*
	From MD95-2042 RI-OH′	1	–0.28	–0.03	*–0.25*	*0.05*	–0.48	–0.17	*–0.29*	*0.07*	–0.16	–0.02	*–0.13*	*0.10*
	to NGRIP T_{air} bis	2	–0.25	–0.05	*–0.27*	*0.01*	–0.41	–0.13	*–0.26*	*0.06*	–0.16	–0.02	*–0.13*	*0.10*
MD95-2042 IVC $\delta^{18}O$ benthic	From MD95-2042 $U^{K'}_{37}$	1	*–0.17*	*0.07*	–0.29	–0.03	–0.32	–0.05	–0.31	–0.01	–0.19	–0.03	*–0.17*	*0.02*
	to NGRIP T_{air}	2	–0.26	–0.04	–0.33	–0.07	–0.38	–0.10	–0.31	–0.04	–0.19	–0.03	*–0.17*	*0.02*
	From MD95-2042 $U^{K'}_{37}$	1	*–0.22*	*0.08*	–0.31	–0.02	–0.33	–0.04	–0.32	–0.01	–0.19	–0.03	*–0.17*	*0.02*
	to NGRIP T_{air} bis	2	–0.30	–0.03	–0.35	–0.06	–0.39	–0.08	–0.31	–0.03	–0.19	–0.03	*–0.17*	*0.02*
	From MD95-2042 RI-OH′	1	*–0.27*	*0.01*	–0.32	–0.03	–0.48	–0.15	–0.35	–0.02	–0.19	–0.03	*–0.17*	*0.02*
	to NGRIP T_{air}	2	–0.27	–0.06	–0.37	–0.07	–0.46	–0.16	–0.35	–0.06	–0.19	–0.03	*–0.17*	*0.02*
	From MD95-2042 RI-OH′	1	*–0.30*	*0.02*	–0.34	–0.03	–0.49	–0.14	–0.37	–0.03	–0.19	–0.03	*–0.17*	*0.02*
	to NGRIP T_{air} bis	2	–0.32	–0.05	–0.37	–0.07	–0.48	–0.14	–0.35	–0.05	–0.19	–0.03	*–0.17*	*0.02*
	From MD95-2042 IVC $\delta^{18}O$ *G. bulloides*	1	*–0.14*	*0.15*	–0.31	–0.03	–0.32	–0.01	–0.32	–0.01	–0.19	–0.03	*–0.17*	*0.02*
	to NGRIP T_{air}	2	*–0.21*	*< 0.01*	–0.28	–0.05	–0.35	–0.05	*–0.25*	*0.01*	–0.19	–0.03	*–0.17*	*0.02*
	From MD95-2042 IVC $\delta^{18}O$ *G. bulloides*	1	*–0.18*	*0.15*	–0.33	–0.03	*–0.34*	*< 0.01*	–0.33	–0.02	–0.19	–0.03	*–0.17*	*0.02*
	to NGRIP T_{air} bis	2	*–0.27*	*< 0.01*	–0.29	–0.03	–0.35	–0.03	*–0.26*	*0.01*	–0.19	–0.03	*–0.17*	*0.02*

Table S5. Bootstrap results for correlation comparisons between different observed Northern Hemisphere paleothermometric records. Each column indicates the 2.5th and 97.5th percentiles that define 95% confidence intervals. Negative differences indicate weaker correlations when using Greenland paleothermometric records than when using Iberian Margin paleothermometric records. Correlations with the main Southern Hemisphere record are shown with bold text and numbers. Non-significant correlation differences are shown with grey numbers in italics. AA, Antarctic stack of EDC, EDML, and WD; ATS, Antarctic Temperature Stack (71); and IVC, ice-volume–corrected.

			95% confidence intervals of changes in absolute coefficient correlation values for all DO-AIM pairs											
			$\Delta T_s \cdot \Delta t_n$ vs $\Delta T_n \cdot \Delta t_n$				ΔT_s vs $\Delta T_n \cdot \Delta t_n$				ΔT_s vs Δt_n			
SH record	NH records	Scenario	Pearson *r*		Kendall τ		Pearson *r*		Kendall τ		Pearson *r*		Kendall τ	
AA $\delta^{18}O_{ice}$ stack	**From MD95-2042 $U^{K'}_{37}$**	**1**	***–0.16***	***0.09***	***–0.29***	***0.02***	***–0.43***	***0.03***	***–0.31***	***0.12***	***–0.27***	***0.10***	***–0.15***	***0.18***
	to NGRIP T_{air}	**2**	***–0.47***	***0.07***	***–0.34***	***0.01***	***–0.56***	***0.09***	***–0.33***	***0.14***	***–0.27***	***0.10***	***–0.15***	***0.18***
	From MD95-2042 RI-OH′	**1**	**–0.43**	**< –0.01**	***–0.26***	***0.17***	**–0.66**	**–0.08**	***–0.32***	***0.24***	***–0.27***	***0.10***	***–0.15***	***0.18***
	to NGRIP T_{air}	**2**	***–0.56***	***< 0.01***	***–0.37***	***0.06***	**–0.67**	**–0.01**	***–0.32***	***0.19***	***–0.27***	***0.10***	***–0.15***	***0.18***
AA T_{air} stack	From MD95-2042 $U^{K'}_{37}$	1	*–0.16*	*0.09*	*–0.28*	*0.02*	*–0.42*	*0.03*	*–0.31*	*0.12*	*–0.27*	*0.10*	*–0.15*	*0.18*
	to NGRIP T_{air}	2	*–0.48*	*0.07*	*–0.33*	*0.02*	*–0.57*	*0.09*	*–0.33*	*0.14*	*–0.27*	*0.10*	*–0.15*	*0.18*
	From MD95-2042 RI-OH′	1	*–0.44*	*< 0.01*	*–0.24*	*0.17*	–0.67	–0.07	*–0.32*	*0.24*	*–0.27*	*0.10*	*–0.15*	*0.18*
	to NGRIP T_{air}	2	*–0.57*	*< 0.01*	*–0.34*	*0.08*	–0.68	–0.01	*–0.32*	*0.19*	*–0.27*	*0.10*	*–0.15*	*0.18*
ATS	From MD95-2042 $U^{K'}_{37}$	1	*–0.18*	*0.10*	*–0.36*	*0.03*	*–0.39*	*0.02*	*–0.27*	*0.17*	*–0.29*	*0.10*	*–0.13*	*0.22*
	to NGRIP T_{air}	2	*–0.55*	*0.06*	*–0.43*	*0.04*	*–0.65*	*0.09*	*–0.37*	*0.10*	*–0.29*	*0.10*	*–0.13*	*0.22*
	From MD95-2042 RI-OH′	1	–0.50	–0.01	*–0.30*	*0.08*	–0.69	–0.11	*–0.36*	*0.13*	*–0.29*	*0.10*	*–0.13*	*0.22*
	to NGRIP T_{air}	2	*–0.63*	*< 0.01*	*–0.39*	*0.04*	–0.74	–0.03	*–0.41*	*0.08*	*–0.29*	*0.10*	*–0.13*	*0.22*
MD95-2042 IVC $\delta^{18}O$ benthic	From MD95-2042 $U^{K'}_{37}$	1	*–0.28*	*0.06*	*–0.29*	*0.04*	*–0.47*	*0.07*	*–0.38*	*0.08*	*–0.32*	*0.06*	*–0.26*	*0.08*
	to NGRIP T_{air}	2	–0.58	–0.03	–0.44	–0.02	–0.64	–0.03	*–0.44*	*0.02*	*–0.32*	*0.06*	*–0.26*	*0.08*
	From MD95-2042 RI-OH′	1	*–0.55*	*0.03*	*–0.36*	*0.03*	–0.70	–0.07	*–0.41*	*0.07*	*–0.32*	*0.06*	*–0.26*	*0.08*
	to NGRIP T_{air}	2	–0.65	–0.02	–0.45	–0.04	–0.71	–0.08	–0.46	–0.01	*–0.32*	*0.06*	*–0.26*	*0.08*
	From MD95-2042 IVC $\delta^{18}O$ *G. bulloides*	1	*–0.30*	*0.14*	–0.39	–0.01	*–0.55*	*0.11*	*–0.41*	*0.06*	*–0.32*	*0.06*	*–0.26*	*0.08*
	to NGRIP T_{air}	2	*–0.54*	*0.03*	*–0.35*	*0.06*	*–0.56*	*0.07*	*–0.35*	*0.10*	*–0.32*	*0.06*	*–0.26*	*0.08*

Table S6. Correlation results for Southern versus Northern Hemisphere diagrams restricted to Heinrich and Heinrich-like stadials and to other Dansgaard–Oeschger stadials using observed paleothermometric records. As Table S3, but considering only Heinrich and Heinrich-like stadials (H) and only other Dansgaard–Oeschger stadials (DO). Correlations with the main Southern Hemisphere record are shown with bold text and numbers. Non-significant correlations are shown with grey numbers in italics. AA, Antarctic stack of EDC, EDML, and WD; ATS, Antarctic Temperature Stack (71); and IVC, ice-volume–corrected.

		Correlation coefficients and *p*-values for only H and H-like stadials (n = 14) and for only other DO stadials (n = 11)																			
		$\Delta T_s \cdot \Delta t_n$ vs $\Delta T_n \cdot \Delta t_n$								ΔT_s vs $\Delta T_n \cdot \Delta t_n$								ΔT_s vs Δt_n			
		Pearson r				Kendall τ				Pearson r				Kendall τ				Pearson r		Kendall τ	
		1	2	1	2	1	2	1	2			1	2	1	2	1	2				
SH record	NH record	H	DO	H	DO	H	DO	H	DO	H	DO	H	DO	H	DO	H	DO	H	DO	H	DO
AA $\delta^{18}O_{ice}$ stack	**NGRIP**	**–0.75**	**–0.77**	**–0.76**	**–0.86**	**–0.47**	**–0.49**	**–0.43**	**–0.67**	*–0.23*	*–0.24*	*–0.31*	*–0.41*	*–0.25*	*–0.16*	*–0.34*	*–0.27*	*0.42*	*0.04*	**0.41**	*0.13*
	T_{air}	**0.002**	**0.006**	**0.001**	**< 0.001**	**0.019**	**0.041**	**0.036**	**0.003**	*0.421*	*0.469*	*0.277*	*0.209*	*0.233*	*0.542*	*0.101*	*0.283*	*0.132*	*0.918*	**0.047**	*0.648*
	MD95-2042	**–0.70**	**–0.82**	**–0.81**	**–0.83**	**–0.60**	**–0.67**	**–0.56**	**–0.67**	*–0.35*	*–0.55*	*–0.48*	*–0.57*	**–0.45**	**–0.49**	**–0.45**	**–0.49**	**0.55**	*0.36*	**0.45**	*0.29*
	$U^{K'}_{37}$	**0.005**	**0.002**	**< 0.001**	**0.002**	**0.002**	**0.003**	**0.005**	**0.003**	*0.224*	*0.078*	*0.082*	*0.068*	**0.026**	**0.041**	**0.026**	**0.041**	**0.041**	*0.280*	**0.026**	*0.212*
	MD95-2042	**–0.92**	*–0.38*	**–0.91**	*–0.59*	**–0.63**	*–0.31*	**–0.60**	**–0.56**	**–0.72**	*–0.05*	**–0.70**	*–0.20*	**–0.60**	*–0.05*	**–0.54**	*–0.24*	**0.55**	*0.36*	**0.45**	*0.29*
	RI-OH′	**< 0.001**	*0.254*	**< 0.001**	*0.056*	**0.001**	*0.218*	**0.002**	**0.017**	**0.004**	*0.880*	**0.005**	*0.563*	**0.002**	*0.879*	**0.007**	*0.359*	**0.041**	*0.280*	**0.026**	*0.212*
AA T_{air} stack	NGRIP	–0.74	–0.77	–0.75	–0.86	–0.47	–0.53	–0.43	–0.71	*–0.23*	*–0.21*	*–0.30*	*–0.38*	*–0.25*	*–0.13*	*–0.34*	*–0.24*	*0.42*	*–0.01*	0.41	*0.09*
	T_{air}	0.003	0.006	0.002	< 0.001	0.019	0.026	0.036	0.002	*0.421*	*0.527*	*0.291*	*0.247*	*0.233*	*0.648*	*0.101*	*0.359*	*0.131*	*0.980*	0.047	*0.761*
	MD95-2042	–0.68	–0.82	–0.80	–0.83	–0.63	–0.71	–0.54	–0.71	*–0.35*	*–0.54*	*–0.48*	*–0.56*	–0.45	*–0.45*	–0.45	*–0.45*	0.56	*0.33*	0.45	*0.26*
	$U^{K'}_{37}$	0.007	0.002	< 0.001	0.001	0.001	0.002	0.007	0.002	*0.226*	*0.088*	*0.083*	*0.075*	0.026	*0.060*	0.026	*0.060*	0.038	*0.321*	0.026	*0.274*
	MD95-2042	–0.91	*–0.37*	–0.90	*–0.59*	–0.60	*–0.35*	–0.58	–0.53	–0.72	*–0.02*	–0.70	*–0.18*	–0.60	*–0.02*	–0.54	*–0.20*	0.56	*0.33*	0.45	*0.26*
	RI-OH′	< 0.001	*0.263*	< 0.001	*0.057*	0.002	*0.165*	0.003	0.026	0.004	*0.944*	0.005	*0.606*	0.002	*1.000*	0.007	*0.445*	0.038	*0.321*	0.026	*0.274*
ATS	NGRIP	–0.66	*–0.59*	–0.67	–0.62	–0.47	*–0.24*	–0.47	*–0.42*	*–0.20*	*0.02*	*–0.24*	*0.01*	*–0.25*	*0.02*	*–0.30*	*0.05*	*0.39*	*–0.03*	0.41	*–0.13*
	T_{air}	0.010	*0.057*	0.009	0.044	0.019	*0.359*	0.019	*0.087*	*0.493*	*0.951*	*0.411*	*0.977*	*0.233*	*1.000*	*0.157*	*0.879*	*0.168*	*0.919*	0.047	*0.648*
	MD95-2042	–0.58	–0.81	–0.72	–0.89	–0.63	–0.71	–0.58	–0.78	*–0.31*	*–0.19*	*–0.47*	*–0.27*	–0.45	*–0.09*	–0.45	*–0.16*	0.59	*–0.07*	0.45	*–0.04*
	$U^{K'}_{37}$	0.030	0.003	0.004	< 0.001	0.001	0.002	0.003	< 0.001	*0.274*	*0.579*	*0.088*	*0.415*	0.026	*0.761*	0.026	*0.542*	0.025	*0.827*	0.026	*0.876*
	MD95-2042	–0.88	–0.67	–0.85	–0.85	–0.69	–0.49	–0.67	–0.60	–0.73	*–0.30*	–0.68	*–0.26*	–0.60	*–0.24*	–0.54	*–0.20*	0.59	*–0.07*	0.45	*–0.04*
	RI-OH′	< 0.001	0.023	< 0.001	< 0.001	< 0.001	0.041	< 0.001	0.010	0.003	*0.372*	0.007	*0.432*	0.002	*0.359*	0.007	*0.445*	0.025	*0.827*	0.026	*0.876*
MD95-2042 IVC $\delta^{18}O$ benthic	NGRIP	–0.75	*–0.34*	–0.74	*–0.54*	*–0.32*	*–0.31*	*–0.36*	*–0.35*	*–0.12*	*0.17*	*–0.18*	*–0.11*	*0.05*	*–0.05*	*–0.08*	*–0.16*	*0.31*	*0.11*	*0.14*	*0.09*
	T_{air}	0.002	*0.299*	0.003	*0.088*	*0.127*	*0.218*	*0.079*	*0.165*	*0.674*	*0.626*	*0.536*	*0.745*	*0.830*	*0.879*	*0.747*	*0.542*	*0.287*	*0.747*	*0.518*	*0.761*
	MD95-2042	–0.78	–0.70	–0.90	–0.74	–0.47	–0.53	–0.69	–0.60	*–0.39*	*–0.50*	–0.57	*–0.54*	*–0.23*	*–0.31*	–0.45	*–0.31*	*0.49*	*0.49*	*0.23*	*0.33*
	$U^{K'}_{37}$	< 0.001	0.018	< 0.001	0.009	0.019	0.026	< 0.001	0.010	*0.165*	*0.120*	0.034	*0.084*	*0.279*	*0.218*	0.026	*0.218*	*0.077*	*0.125*	*0.279*	*0.160*
	MD95-2042	–0.90	*–0.47*	–0.93	*–0.75*	–0.71	*–0.38*	–0.82	–0.49	–0.67	*–0.32*	–0.71	*–0.58*	–0.43	*–0.16*	–0.58	*–0.27*	*0.49*	*0.49*	*0.23*	*0.33*
	RI-OH′	< 0.001	*0.142*	< 0.001	*0.007*	< 0.001	*0.121*	< 0.001	0.041	0.009	*0.344*	0.004	*0.062*	0.036	*0.542*	0.003	*0.283*	*0.077*	*0.125*	*0.279*	*0.160*
	MD95-2042	–0.70	–0.84	–0.84	–0.63	–0.67	–0.71	–0.54	–0.56	*–0.34*	*–0.55*	*–0.49*	*–0.31*	*–0.38*	*–0.27*	*–0.34*	*–0.27*	*0.49*	*0.49*	*0.23*	*0.33*
	IVC $\delta^{18}O$ *G. bulloides*	0.006	0.001	< 0.001	0.037	< 0.001	0.002	0.007	0.017	*0.235*	*0.077*	*0.075*	*0.359*	*0.062*	*0.283*	*0.101*	*0.283*	*0.077*	*0.125*	*0.279*	*0.160*

Table S7. Correlation results for Southern versus Northern Hemisphere diagrams using filtered and simulated paleothermometric records after a band-pass filtering with a 500- to 10,000-y window. All *r* and τ values are reported above their associated *p*-values. $\Delta T_s \cdot \Delta t_n$ versus $\Delta T_n \cdot \Delta t_n$ diagrams consider temperature amplitudes for both hemispheres (ΔT_s and ΔT_n) and Northern Hemisphere (NH) cold event durations (Δt_n). ΔT_s versus Δt_n diagrams represent Southern Hemisphere (SH) temperature amplitudes versus NH cold event durations as shown in refs. 81, 82, 83, and 84. Both Scenarios 1 and 2 are considered (see *Materials and Methods* and Text S8, above). Non-significant correlations are shown with grey numbers in italics. AA, Antarctic stack of EDC, EDML, and WD; and BSO, bipolar seesaw output.

		Correlation coefficients and *p*-values for all DO-AIM pairs (*n* = 25, except for Iberian Margin BSOs where *n* = 24)									
		$\Delta T_s \cdot \Delta t_n$ vs $\Delta T_n \cdot \Delta t_n$				ΔT_s vs $\Delta T_n \cdot \Delta t_n$				ΔT_s vs Δt_n	
		Pearson *r*		Kendall τ		Pearson *r*		Kendall τ		Pearson *r*	Kendall τ
SH record	NH record	1	2	1	2	1	2	1	2		
Filtered AA $\delta^{18}O_{ice}$ stack	NGRIP	–0.73	–0.75	–0.59	–0.63	*–0.09*	*–0.16*	*–0.17*	–0.29	*0.18*	0.31
	T_{air}	< 0.001	< 0.001	< 0.001	< 0.001	*0.674*	*0.439*	*0.255*	0.046	*0.386*	0.033
	MD95-2042	–0.79	–0.83	–0.75	–0.75	*–0.25*	*–0.30*	–0.37	–0.35	*0.23*	*0.28*
	$U^{K'}_{37}$	< 0.001	< 0.001	< 0.001	< 0.001	*0.222*	*0.149*	0.010	0.015	*0.275*	*0.053*
	MD95-2042	–0.90	–0.88	–0.71	–0.73	–0.41	–0.43	–0.31	–0.33	*0.23*	*0.28*
	RI-OH′	< 0.001	< 0.001	< 0.001	< 0.001	0.041	0.033	0.029	0.022	*0.275*	*0.053*
Filtered AA T_{air} stack	NGRIP	–0.72	–0.75	–0.59	–0.63	*–0.09*	*–0.16*	*–0.18*	–0.29	*0.18*	0.31
	T_{air}	< 0.001	< 0.001	< 0.001	< 0.001	*0.679*	*0.442*	*0.218*	0.046	*0.385*	0.033
	MD95-2042	–0.79	–0.83	–0.75	–0.75	*–0.25*	*–0.30*	–0.37	–0.35	*0.23*	0.29
	$U^{K'}_{37}$	< 0.001	< 0.001	< 0.001	< 0.001	*0.222*	*0.150*	0.010	0.015	*0.276*	0.042
	MD95-2042	–0.90	–0.88	–0.71	–0.73	–0.41	–0.42	–0.31	–0.33	*0.23*	0.29
	RI-OH′	< 0.001	< 0.001	< 0.001	< 0.001	0.043	0.035	0.029	0.022	*0.276*	0.042
BSO NGRIP T_{air}	NGRIP	–0.72	–0.79	–0.49	–0.73	*–0.16*	*–0.32*	*–0.18*	–0.46	*0.11*	*0.24*
	T_{air}	< 0.001	< 0.001	< 0.001	< 0.001	*0.431*	*0.122*	*0.218*	< 0.001	*0.596*	*0.098*
	MD95-2042	–0.80	–0.82	–0.60	–0.63	*–0.27*	*–0.30*	–0.29	–0.29	*0.20*	*0.22*
	$U^{K'}_{37}$	< 0.001	< 0.001	< 0.001	< 0.001	*0.192*	*0.146*	0.046	0.041	*0.336*	*0.118*
	MD95-2042	–0.84	–0.83	–0.55	–0.59	*–0.30*	*–0.33*	*–0.22*	*–0.25*	*0.20*	*0.22*
	RI-OH′	< 0.001	< 0.001	< 0.001	< 0.001	*0.144*	*0.105*	*0.130*	*0.088*	*0.336*	*0.118*
BSO NGRIP $\delta^{18}O_{ice}$	NGRIP	–0.78	–0.85	–0.47	–0.67	*–0.20*	*–0.36*	*–0.19*	–0.43	*0.18*	*0.27*
	T_{air}	< 0.001	< 0.001	< 0.001	< 0.001	*0.327*	*0.080*	*0.185*	0.002	*0.382*	*0.065*
	MD95-2042	–0.85	–0.89	–0.59	–0.61	*–0.36*	–0.42	–0.29	–0.31	*0.28*	*0.25*
	$U^{K'}_{37}$	< 0.001	< 0.001	< 0.001	< 0.001	*0.081*	0.038	0.046	0.033	*0.167*	*0.080*
	MD95-2042	–0.87	–0.89	–0.56	–0.61	–0.42	–0.48	*–0.26*	–0.31	*0.28*	*0.25*
	RI-OH′	< 0.001	< 0.001	< 0.001	< 0.001	0.038	0.015	*0.072*	0.029	*0.167*	*0.080*
BSO MD95-2042 $U^{K'}_{37}$	NGRIP	–0.90	–0.93	–0.54	–0.62	–0.60	–0.67	–0.36	–0.49	0.59	0.47
	T_{air}	< 0.001	< 0.001	< 0.001	< 0.001	0.002	< 0.001	0.013	< 0.001	0.002	< 0.001
	MD95-2042	–0.95	–0.97	–0.84	–0.88	–0.74	–0.80	–0.59	–0.62	0.65	0.47
	$U^{K'}_{37}$	< 0.001	< 0.001	< 0.001	< 0.001	< 0.001	< 0.001	< 0.001	< 0.001	< 0.001	0.001
	MD95-2042	–0.91	–0.93	–0.72	–0.81	–0.80	–0.84	–0.55	–0.64	0.65	0.47
	RI-OH′	< 0.001	< 0.001	< 0.001	< 0.001	< 0.001	< 0.001	< 0.001	< 0.001	< 0.001	0.001
BSO MD95-2042 RI-OH′	NGRIP	–0.83	–0.85	–0.46	–0.51	–0.44	–0.49	*–0.28*	–0.35	0.48	0.38
	T_{air}	< 0.001	< 0.001	0.001	< 0.001	0.030	0.016	*0.062*	0.017	0.017	0.008
	MD95-2042	–0.86	–0.91	–0.73	–0.74	–0.61	–0.68	–0.51	–0.53	0.58	0.40
	$U^{K'}_{37}$	< 0.001	< 0.001	< 0.001	< 0.001	0.002	< 0.001	< 0.001	< 0.001	0.003	0.007
	MD95-2042	–0.97	–0.97	–0.79	–0.85	–0.80	–0.83	–0.59	–0.62	0.58	0.58
	RI-OH′	< 0.001	< 0.001	< 0.001	< 0.001	< 0.001	< 0.001	< 0.001	< 0.001	0.003	0.003

Table S8. Monte Carlo results for correlation comparisons between different filtered and simulated Northern Hemisphere paleothermometric records after a band-pass filtering with a 500- to 10,000-y window. Each column indicates the 2.5th and 97.5th percentiles that define 95% confidence intervals. Negative differences indicate weaker correlations when using Greenland paleothermometric records than when using Iberian Margin paleothermometric records. Non-significant correlation differences are shown with grey numbers in italics. AA, Antarctic stack of EDC, EDML, and WD; and BSO, bipolar seesaw output.

			95% confidence intervals of changes in absolute coefficient correlation values for all DO-AIM pairs											
			$\Delta T_s \cdot \Delta t_n$ vs $\Delta T_n \cdot \Delta t_n$				ΔT_s vs $\Delta T_n \cdot \Delta t_n$				ΔT_s vs Δt_n			
SH record	NH records	Scenario	Pearson *r*		Kendall τ		Pearson *r*		Kendall τ		Pearson *r*		Kendall τ	
Filtered AA $\delta^{18}O_{ice}$ stack	From MD95-2042 $U^{K'}_{37}$	1	–0.11	–0.01	–0.27	–0.11	–0.22	–0.11	–0.27	–0.13	–0.07	–0.02	*–0.02*	*0.07*
	to NGRIP T_{air}	2	–0.11	–0.03	–0.19	–0.06	–0.19	–0.08	–0.15	–0.02	–0.07	–0.02	*–0.02*	*0.07*
	From MD95-2042 RI-OH′	1	–0.23	–0.13	–0.19	–0.05	–0.37	–0.26	–0.21	–0.08	–0.07	–0.02	*–0.02*	*0.07*
	to NGRIP T_{air}	2	–0.18	–0.09	–0.17	–0.05	–0.31	–0.20	–0.12	0.00	–0.07	–0.02	*–0.02*	*0.07*
Filtered AA T_{air} stack	From MD95-2042 $U^{K'}_{37}$	1	–0.12	–0.01	–0.26	–0.11	–0.22	–0.11	–0.27	–0.13	–0.07	–0.02	*–0.02*	*0.07*
	to NGRIP T_{air}	2	–0.12	–0.03	–0.19	–0.06	–0.19	–0.08	–0.15	–0.02	–0.07	–0.02	*–0.02*	*0.07*
	From MD95-2042 RI-OH′	1	–0.23	–0.13	–0.19	–0.05	–0.37	–0.26	–0.21	–0.08	–0.07	–0.02	*–0.02*	*0.07*
	to NGRIP T_{air}	2	–0.17	–0.09	–0.17	–0.05	–0.31	–0.20	–0.12	0.00	–0.07	–0.02	*–0.02*	*0.07*
BSO NGRIP T_{air}	From MD95-2042 $U^{K'}_{37}$	1	–0.13	–0.02	–0.19	–0.08	–0.15	–0.05	–0.17	–0.07	–0.10	–0.08	*–0.01*	*0.03*
	to NGRIP T_{air}	2	*–0.07*	*0.02*	0.01	0.11	*–0.03*	*0.07*	0.08	0.19	–0.10	–0.08	*–0.01*	*0.03*
	From MD95-2042 RI-OH′	1	–0.16	–0.09	–0.14	–0.03	–0.17	–0.10	–0.11	–0.01	–0.10	–0.08	*–0.01*	*0.03*
	to NGRIP T_{air}	2	–0.07	< –0.01	0.06	0.15	*–0.05*	*0.02*	0.13	0.23	–0.10	–0.08	*–0.01*	*0.03*
BSO NGRIP $\delta^{18}O_{ice}$	From MD95-2042 $U^{K'}_{37}$	1	–0.11	–0.03	–0.21	–0.09	–0.20	–0.10	–0.18	–0.06	–0.11	–0.09	< 0.01	0.03
	to NGRIP T_{air}	2	*–0.07*	*< 0.01*	*–0.03*	*0.09*	–0.11	–0.01	0.06	0.17	–0.11	–0.09	< 0.01	0.03
	From MD95-2042 RI-OH′	1	–0.13	–0.05	–0.17	–0.06	–0.25	–0.17	–0.15	–0.03	–0.11	–0.09	< 0.01	0.03
	to NGRIP T_{air}	2	–0.07	< –0.01	*–0.03*	*0.08*	–0.17	–0.08	0.05	0.16	–0.11	–0.09	< 0.01	0.03
BSO MD95-2042 $U^{K'}_{37}$	From MD95-2042 $U^{K'}_{37}$	1	–0.08	–0.03	–0.34	–0.22	–0.19	–0.10	–0.30	–0.17	–0.07	–0.04	*–0.04*	*0.06*
	to NGRIP T_{air}	2	–0.07	–0.03	–0.30	–0.17	–0.17	–0.09	–0.22	–0.07	–0.07	–0.04	*–0.04*	*0.06*
	From MD95-2042 RI-OH′	1	*–0.05*	*0.03*	–0.26	–0.12	–0.23	–0.15	–0.27	–0.12	–0.07	–0.04	*–0.04*	*0.06*
	to NGRIP T_{air}	2	*–0.03*	*0.03*	–0.24	–0.11	–0.20	–0.13	–0.21	–0.07	–0.07	–0.04	*–0.04*	*0.06*
BSO MD95-2042 RI-OH′	From MD95-2042 $U^{K'}_{37}$	1	*–0.07*	*0.01*	–0.33	–0.21	–0.21	–0.11	–0.29	–0.17	–0.10	–0.09	*–0.06*	*0.02*
	to NGRIP T_{air}	2	–0.09	–0.03	–0.30	–0.20	–0.24	–0.15	–0.25	–0.12	–0.10	–0.09	*–0.06*	*0.02*
	From MD95-2042 RI-OH′	1	–0.16	–0.11	–0.40	–0.29	–0.40	–0.33	–0.38	–0.28	–0.10	–0.09	*–0.06*	*0.02*
	to NGRIP T_{air}	2	–0.14	–0.10	–0.40	–0.30	–0.37	–0.31	–0.34	–0.22	–0.10	–0.09	*–0.06*	*0.02*

Table S9. Bootstrap results for correlation comparisons between different filtered and simulated Northern Hemisphere paleothermometric records after a band-pass filtering with a 500- to 10,000-y window. Each column indicates the 2.5th and 97.5th percentiles that define 95% confidence intervals. Negative differences indicate weaker correlations when using Greenland paleothermometric records than when using Iberian Margin paleothermometric records. Non-significant correlation differences are shown with grey numbers in italics. AA, Antarctic stack of EDC, EDML, and WD; and BSO, bipolar seesaw output.

			95% confidence intervals of changes in absolute coefficient correlation values for all DO-AIM pairs											
			$\Delta T_s \cdot \Delta t_n$ vs $\Delta T_n \cdot \Delta t_n$				ΔT_s vs $\Delta T_n \cdot \Delta t_n$				ΔT_s vs Δt_n			
SH record	NH records	Scenario	Pearson *r*		Kendall τ		Pearson *r*		Kendall τ		Pearson *r*		Kendall τ	
Filtered AA $\delta^{18}O_{ice}$ stack	From MD95-2042 $U^{K'}_{37}$	1	*–0.22*	*0.05*	*–0.37*	*0.05*	*–0.43*	*0.13*	*–0.45*	*0.10*	*–0.19*	*0.13*	*–0.12*	*0.18*
	to NGRIP T_{air}	2	–0.26	< –0.01	*–0.34*	*0.10*	*–0.29*	*0.07*	*–0.27*	*0.13*	*–0.19*	*0.13*	*–0.12*	*0.18*
	From MD95-2042 RI-OH′	1	–0.32	–0.04	*–0.33*	*0.14*	*–0.47*	*0.02*	*–0.42*	*0.17*	*–0.19*	*0.13*	*–0.12*	*0.18*
	to NGRIP T_{air}	2	–0.34	–0.01	*–0.31*	*0.11*	*–0.41*	*< 0.01*	*–0.27*	*0.18*	*–0.19*	*0.13*	*–0.12*	*0.18*
Filtered AA T_{air} stack	From MD95-2042 $U^{K'}_{37}$	1	*–0.22*	*0.05*	*–0.38*	*0.06*	*–0.42*	*0.13*	*–0.45*	*0.10*	*–0.19*	*0.13*	*–0.15*	*0.17*
	to NGRIP T_{air}	2	–0.26	< –0.01	*–0.33*	*0.09*	*–0.29*	*0.07*	*–0.27*	*0.13*	*–0.19*	*0.13*	*–0.15*	*0.17*
	From MD95-2042 RI-OH′	1	–0.32	–0.03	*–0.34*	*0.15*	*–0.47*	*0.03*	*–0.41*	*0.20*	*–0.19*	*0.13*	*–0.15*	*0.17*
	to NGRIP T_{air}	2	–0.34	–0.01	*–0.30*	*0.10*	*–0.41*	*0.01*	*–0.27*	*0.18*	*–0.19*	*0.13*	*–0.15*	*0.17*
BSO NGRIP T_{air}	From MD95-2042 $U^{K'}_{37}$	1	*–0.25*	*0.05*	*–0.39*	*0.13*	*–0.28*	*0.07*	*–0.35*	*0.16*	*–0.19*	*0.22*	*–0.14*	*0.19*
	to NGRIP T_{air}	2	*–0.10*	*0.08*	*–0.11*	*0.30*	*–0.14*	*0.27*	*–0.08*	*0.39*	*–0.19*	*0.22*	*–0.14*	*0.19*
	From MD95-2042 RI-OH′	1	*–0.26*	*0.07*	*–0.35*	*0.19*	*–0.35*	*0.17*	*–0.28*	*0.24*	*–0.19*	*0.22*	*–0.14*	*0.19*
	to NGRIP T_{air}	2	*–0.12*	*0.15*	*–0.08*	*0.38*	*–0.23*	*0.36*	*–0.04*	*0.45*	*–0.19*	*0.22*	*–0.14*	*0.19*
BSO NGRIP $\delta^{18}O_{ice}$	From MD95-2042 $U^{K'}_{37}$	1	*–0.34*	*0.02*	*–0.38*	*0.12*	*–0.36*	*0.01*	*–0.30*	*0.17*	*–0.22*	*0.20*	*–0.14*	*0.17*
	to NGRIP T_{air}	2	*–0.17*	*0.02*	*–0.12*	*0.24*	*–0.20*	*0.13*	*–0.07*	*0.32*	*–0.22*	*0.20*	*–0.14*	*0.17*
	From MD95-2042 RI-OH′	1	*–0.35*	*0.03*	*–0.37*	*0.16*	*–0.39*	*0.04*	*–0.28*	*0.20*	*–0.22*	*0.20*	*–0.14*	*0.17*
	to NGRIP T_{air}	2	*–0.20*	*0.06*	*–0.13*	*0.24*	*–0.30*	*0.16*	*–0.11*	*0.33*	*–0.22*	*0.20*	*–0.14*	*0.17*
BSO MD95-2042 $U^{K'}_{37}$	From MD95-2042 $U^{K'}_{37}$	1	–0.24	< –0.01	–0.60	–0.05	–0.40	–0.02	*–0.52*	*0.02*	*–0.25*	*0.09*	*–0.18*	*0.21*
	to NGRIP T_{air}	2	–0.22	–0.02	–0.49	–0.06	–0.28	–0.02	*–0.37*	*0.10*	*–0.25*	*0.09*	*–0.18*	*0.21*
	From MD95-2042 RI-OH′	1	*–0.29*	*0.08*	*–0.44*	*0.01*	–0.45	–0.02	*–0.46*	*0.07*	*–0.25*	*0.09*	*–0.18*	*0.21*
	to NGRIP T_{air}	2	*–0.24*	*0.04*	–0.42	–0.01	–0.33	–0.02	*–0.41*	*0.06*	*–0.25*	*0.09*	*–0.18*	*0.21*
BSO MD95-2042 RI-OH′	From MD95-2042 $U^{K'}_{37}$	1	*–0.25*	*0.07*	–0.50	–0.04	–0.42	–0.02	–0.47	< –0.01	*–0.27*	*0.06*	*–0.19*	*0.16*
	to NGRIP T_{air}	2	–0.30	–0.01	–0.44	–0.02	–0.38	–0.03	–0.39	0.00	*–0.27*	*0.06*	*–0.19*	*0.16*
	From MD95-2042 RI-OH′	1	–0.42	–0.04	–0.58	–0.10	–0.60	–0.18	–0.53	–0.10	*–0.27*	*0.06*	*–0.19*	*0.16*
	to NGRIP T_{air}	2	–0.44	–0.04	–0.56	–0.11	–0.53	–0.17	–0.53	–0.07	*–0.27*	*0.06*	*–0.19*	*0.16*

Table S10. Correlation results for Southern versus Northern Hemisphere diagrams restricted to Heinrich and Heinrich-like stadials and to other Dansgaard–Oeschger stadials using filtered and simulated paleothermometric records after a band-pass filtering with a 500- to 10,000-y window. As Table S7, but considering only Heinrich and Heinrich-like stadials (H) and only other Dansgaard–Oeschger stadials (DO). Non-significant correlation differences are shown with grey numbers in italics. AA, Antarctic stack of EDC, EDML, and WD; and BSO, bipolar seesaw output.

		Correlation coefficients and *p*-values for only H and H-like stadials (n = 14) and for only other DO stadials (n = 11, except for Iberian Margin BSOs where n = 10)																			
		$\Delta T_s \cdot \Delta t_n$ vs $\Delta T_n \cdot \Delta t_n$								ΔT_s vs $\Delta T_n \cdot \Delta t_n$								ΔT_s vs Δt_n			
		Pearson r				Kendall τ				Pearson r				Kendall τ				Pearson r		Kendall τ	
		1		2		1		2		1		2		1		2		1		1	
SH record	NH record	H	DO	H	DO	H	DO	H	DO	H	DO	H	DO	H	DO	H	DO	H	DO	H	DO
Filtered AA $\delta^{18}O_{ice}$ stack	NGRIP	–0.64	*–0.43*	–0.68	–0.72	*–0.49*	*–0.24*	*–0.52*	*–0.53*	*0.28*	*–0.02*	*0.19*	*–0.34*	*0.21*	*0.09*	*–0.03*	*–0.20*	*–0.31*	*0.22*	*–0.14*	*0.20*
	T_{air}	0.014	*0.189*	0.007	0.013	*0.014*	*0.359*	*0.010*	*0.026*	*0.335*	*0.947*	*0.522*	*0.313*	*0.331*	*0.761*	*0.914*	*0.445*	*0.282*	*0.517*	*0.518*	*0.445*
	MD95-2042	–0.66	–0.77	–0.69	–0.76	*–0.60*	*–0.53*	*–0.60*	*–0.53*	*0.18*	*–0.50*	*0.16*	*–0.51*	*–0.01*	*–0.45*	*0.08*	*–0.45*	*–0.28*	*0.29*	*–0.19*	*0.29*
	$U^{K'}_{37}$	0.011	0.005	0.006	0.007	*0.002*	*0.026*	*0.002*	*0.026*	*0.532*	*0.119*	*0.595*	*0.111*	*1.000*	*0.060*	*0.747*	*0.060*	*0.341*	*0.387*	*0.388*	*0.212*
	MD95-2042	–0.83	*–0.31*	–0.78	–0.65	*–0.69*	*–0.24*	*–0.60*	*–0.53*	*0.00*	*–0.26*	*–0.02*	*–0.41*	*–0.05*	*–0.16*	*0.03*	*–0.38*	*–0.28*	*0.29*	*–0.19*	*0.29*
	RI-OH′	< 0.001	*0.358*	< 0.001	0.030	*< 0.001*	*0.359*	*0.002*	*0.026*	*0.999*	*0.439*	*0.935*	*0.209*	*0.830*	*0.542*	*0.914*	*0.121*	*0.341*	*0.387*	*0.388*	*0.212*
Filtered AA T_{air} stack	NGRIP	–0.64	*–0.43*	–0.68	–0.72	*–0.47*	*–0.27*	*–0.54*	*–0.49*	*0.28*	*–0.03*	*0.19*	*–0.33*	*0.19*	*0.05*	*–0.05*	*–0.16*	*–0.31*	*0.22*	*–0.12*	*0.16*
	T_{air}	0.014	*0.182*	0.007	0.013	*0.019*	*0.283*	*0.007*	*0.041*	*0.334*	*0.940*	*0.522*	*0.315*	*0.388*	*0.879*	*0.830*	*0.542*	*0.287*	*0.521*	*0.591*	*0.542*
	MD95-2042	–0.66	–0.77	–0.69	–0.76	*–0.60*	*–0.53*	*–0.60*	*–0.53*	*0.18*	*–0.49*	*0.16*	*–0.51*	*–0.03*	*–0.42*	*0.05*	*–0.42*	*–0.27*	*0.29*	*–0.16*	*0.33*
	$U^{K'}_{37}$	0.011	0.005	0.006	0.007	*0.002*	*0.026*	*0.002*	*0.026*	*0.538*	*0.122*	*0.594*	*0.111*	*0.914*	*0.087*	*0.830*	*0.087*	*0.342*	*0.382*	*0.451*	*0.160*
	MD95-2042	–0.82	*–0.30*	–0.77	–0.65	*–0.69*	*–0.24*	*–0.60*	*–0.53*	*0.00*	*–0.25*	*–0.02*	*–0.41*	*–0.08*	*–0.13*	*0.01*	*–0.35*	*–0.27*	*0.29*	*–0.16*	*0.33*
	RI-OH′	< 0.001	*0.365*	0.001	0.031	*< 0.001*	*0.359*	*0.002*	*0.026*	*0.990*	*0.453*	*0.952*	*0.213*	*0.747*	*0.648*	*1.000*	*0.165*	*0.342*	*0.382*	*0.451*	*0.160*
BSO NGRIP T_{air}	NGRIP	–0.65	*–0.34*	–0.73	–0.79	*–0.47*	*–0.09*	*–0.76*	*–0.53*	*–0.13*	*–0.22*	*–0.27*	–0.66	*–0.12*	*–0.02*	*–0.45*	*–0.38*	*0.01*	*0.20*	*0.10*	*0.31*
	T_{air}	0.012	*0.307*	0.003	0.004	*0.019*	*0.761*	*< 0.001*	*0.026*	*0.669*	*0.508*	*0.351*	0.027	*0.591*	*1.000*	*0.026*	*0.121*	*0.973*	*0.552*	*0.667*	*0.218*
	MD95-2042	–0.73	–0.69	–0.76	*–0.58*	*–0.54*	*–0.53*	*–0.63*	*–0.53*	*–0.25*	*–0.58*	*–0.31*	*–0.47*	*–0.21*	*–0.42*	*–0.25*	*–0.35*	*0.14*	*0.31*	*0.19*	*0.11*
	$U^{K'}_{37}$	0.003	0.019	0.001	*0.061*	*0.007*	*0.026*	*0.001*	*0.026*	*0.388*	*0.059*	*0.287*	*0.140*	*0.331*	*0.087*	*0.233*	*0.165*	*0.639*	*0.360*	*0.388*	*0.639*
	MD95-2042	–0.82	*–0.09*	–0.79	*–0.34*	*–0.58*	*–0.31*	*–0.63*	*–0.38*	*–0.37*	*–0.11*	*–0.40*	*–0.24*	*–0.25*	*–0.13*	*–0.25*	*–0.20*	*0.14*	*0.31*	*0.19*	*0.11*
	RI-OH′	< 0.001	*0.802*	< 0.001	*0.313*	*0.003*	*0.218*	*0.001*	*0.121*	*0.196*	*0.759*	*0.153*	*0.480*	*0.233*	*0.648*	*0.233*	*0.445*	*0.639*	*0.360*	*0.388*	*0.639*
BSO NGRIP $\delta^{18}O_{ice}$	NGRIP	–0.72	*–0.34*	–0.82	–0.72	*–0.38*	*–0.13*	*–0.71*	*–0.42*	*–0.08*	*–0.11*	*–0.25*	*–0.50*	*–0.05*	*–0.02*	*–0.38*	*–0.31*	*–0.03*	*0.39*	*0.03*	*0.31*
	T_{air}	0.004	*0.312*	< 0.001	0.013	*0.062*	*0.648*	*< 0.001*	*0.087*	*0.775*	*0.742*	*0.391*	*0.120*	*0.830*	*1.000*	*0.062*	*0.218*	*0.921*	*0.233*	*0.914*	*0.218*
	MD95-2042	–0.78	–0.70	–0.84	*–0.57*	*–0.49*	*–0.45*	*–0.58*	*–0.38*	*–0.24*	*–0.40*	*–0.33*	*–0.29*	*–0.19*	*–0.27*	*–0.27*	*–0.20*	*0.13*	*0.18*	*0.12*	*0.18*
	$U^{K'}_{37}$	< 0.001	0.016	< 0.001	*0.067*	*0.014*	*0.060*	*0.003*	*0.121*	*0.404*	*0.225*	*0.245*	*0.390*	*0.388*	*0.283*	*0.193*	*0.445*	*0.648*	*0.602*	*0.591*	*0.435*
	MD95-2042	–0.82	*–0.36*	–0.84	*–0.55*	*–0.54*	*–0.31*	*–0.58*	*–0.45*	*–0.33*	*–0.36*	*–0.43*	*–0.34*	*–0.19*	*–0.20*	*–0.27*	*–0.27*	*0.13*	*0.18*	*0.12*	*0.18*
	RI-OH′	< 0.001	*0.280*	< 0.001	*0.077*	*0.007*	*0.218*	*0.003*	*0.060*	*0.257*	*0.279*	*0.125*	*0.303*	*0.388*	*0.445*	*0.193*	*0.283*	*0.648*	*0.602*	*0.591*	*0.435*
BSO MD95-2042 $U^{K'}_{37}$	NGRIP	–0.89	*0.21*	–0.93	*–0.32*	*–0.52*	*0.29*	*–0.67*	*–0.11*	*–0.50*	*0.38*	–0.62	*–0.07*	*–0.25*	*0.51*	*–0.49*	*0.11*	*0.34*	*–0.08*	*0.27*	*–0.16*
	T_{air}	< 0.001	*0.551*	< 0.001	*0.367*	*0.010*	*0.291*	*< 0.001*	*0.727*	*0.066*	*0.283*	0.018	*0.846*	*0.233*	*0.047*	*0.014*	*0.727*	*0.230*	*0.831*	*0.193*	*0.601*
	MD95-2042	–0.93	–0.87	–0.96	–0.92	*–0.71*	*–0.82*	*–0.80*	*–0.82*	–0.61	*–0.45*	–0.68	*–0.52*	*–0.43*	*–0.42*	*–0.47*	*–0.42*	*0.43*	*–0.06*	*0.32*	*–0.04*
	$U^{K'}_{37}$	< 0.001	0.001	< 0.001	< 0.001	*< 0.001*	*< 0.001*	*< 0.001*	*< 0.001*	0.020	*0.191*	0.007	*0.122*	*0.036*	*0.108*	*0.019*	*0.108*	*0.126*	*0.862*	*0.127*	*0.857*
	MD95-2042	–0.87	*–0.34*	–0.89	–0.76	*–0.76*	*–0.20*	*–0.80*	*–0.56*	–0.65	*–0.24*	–0.74	*–0.42*	*–0.43*	*–0.24*	*–0.56*	*–0.42*	*0.43*	*–0.06*	*0.32*	*–0.04*
	RI-OH′	< 0.001	*0.340*	< 0.001	0.011	*< 0.001*	*0.484*	*< 0.001*	*0.029*	0.012	*0.506*	0.002	*0.223*	*0.036*	*0.381*	*0.005*	*0.108*	*0.126*	*0.862*	*0.127*	*0.857*
BSO MD95-2042 RI-OH′	NGRIP	–0.79	*0.27*	–0.83	*–0.09*	*–0.41*	*0.33*	*–0.52*	*0.02*	*–0.24*	*0.41*	*–0.32*	*0.14*	*–0.12*	*0.47*	*–0.27*	*0.24*	*0.15*	*–0.13*	*0.14*	*–0.20*
	T_{air}	< 0.001	*0.453*	< 0.001	*0.798*	*0.047*	*0.216*	*0.010*	*1.000*	*0.411*	*0.243*	*0.258*	*0.693*	*0.591*	*0.073*	*0.193*	*0.381*	*0.615*	*0.716*	*0.518*	*0.484*
	MD95-2042	–0.79	–0.66	–0.86	–0.65	*–0.63*	*–0.42*	*–0.71*	*–0.33*	*–0.38*	*–0.15*	*–0.48*	*–0.16*	*–0.30*	*–0.20*	*–0.38*	*–0.20*	*0.32*	*–0.30*	*0.23*	*–0.18*
	$U^{K'}_{37}$	< 0.001	0.037	< 0.001	0.042	*0.001*	*0.108*	*< 0.001*	*0.216*	*0.185*	*0.680*	*0.083*	*0.653*	*0.157*	*0.484*	*0.062*	*0.484*	*0.262*	*0.396*	*0.279*	*0.472*
	MD95-2042	–0.96	–0.72	–0.95	–0.85	*–0.76*	*–0.51*	*–0.85*	*–0.60*	–0.66	*–0.43*	–0.73	*–0.34*	*–0.43*	*–0.38*	*–0.52*	*–0.38*	*0.32*	*–0.30*	*0.23*	*–0.18*
	RI-OH′	< 0.001	0.019	< 0.001	0.002	*< 0.001*	*0.047*	*< 0.001*	*0.017*	0.010	*0.211*	0.003	*0.336*	*0.036*	*0.156*	*0.010*	*0.156*	*0.262*	*0.396*	*0.279*	*0.472*

Table S11. Correlation results for Southern versus Northern Hemisphere diagrams using filtered and simulated paleothermometric records after a band-pass filtering with a 500- to 16,000-y window. All *r* and τ values are reported above their associated *p*-values. $\Delta T_s \cdot \Delta t_n$ versus $\Delta T_n \cdot \Delta t_n$ diagrams consider temperature amplitudes for both hemispheres (ΔT_s and ΔT_n) and Northern Hemisphere (NH) cold event durations (Δt_n). ΔT_s versus Δt_n diagrams represent Southern Hemisphere (SH) temperature amplitudes versus NH cold event durations as shown in refs. 81, 82, 83, and 84. Both Scenarios 1 and 2 are considered (see *Materials and Methods* and Text S8, above). Non-significant correlations are shown with grey numbers in italics. AA, Antarctic stack of EDC, EDML, and WD; and BSO, bipolar seesaw output.

		Correlation coefficients and *p*-values for all DO-AIM pairs (*n* = 25, except for Iberian Margin BSOs where *n* = 24)									
		$\Delta T_s \cdot \Delta t_n$ vs $\Delta T_n \cdot \Delta t_n$				ΔT_s vs $\Delta T_n \cdot \Delta t_n$				ΔT_s vs Δt_n	
		Pearson *r*		Kendall τ		Pearson *r*		Kendall τ		Pearson *r*	Kendall τ
SH record	NH record	1	2	1	2	1	2	1	2		
Filtered AA $\delta^{18}O_{ice}$ stack	NGRIP	–0.73	–0.80	–0.59	–0.60	*–0.25*	*–0.37*	*–0.26*	–0.31	*0.39*	0.39
	T_{air}	< 0.001	< 0.001	< 0.001	< 0.001	*0.219*	*0.066*	*0.072*	0.029	*0.056*	0.006
	MD95-2042 $U^{K'}_{37}$	–0.79	–0.82	–0.79	–0.79	–0.40	–0.46	–0.44	–0.46	0.43	0.40
		< 0.001	< 0.001	< 0.001	< 0.001	0.047	0.021	0.002	< 0.001	0.033	0.005
	MD95-2042 RI-OH′	–0.91	–0.88	–0.70	–0.75	–0.59	–0.56	–0.41	–0.42	0.43	0.40
		< 0.001	< 0.001	< 0.001	< 0.001	0.002	0.003	0.003	0.003	0.033	0.005
Filtered AA T_{air} stack	NGRIP	–0.73	–0.80	–0.59	–0.60	*–0.25*	*–0.37*	*–0.25*	–0.31	*0.39*	0.39
	T_{air}	< 0.001	< 0.001	< 0.001	< 0.001	*0.220*	*0.065*	*0.080*	0.033	*0.056*	0.005
	MD95-2042 $U^{K'}_{37}$	–0.79	–0.82	–0.79	–0.78	–0.40	–0.45	–0.45	–0.45	0.43	0.39
		< 0.001	< 0.001	< 0.001	< 0.001	0.047	0.022	0.001	0.001	0.034	0.006
	MD95-2042 RI-OH′	–0.91	–0.87	–0.69	–0.74	–0.58	–0.56	–0.41	–0.41	0.43	0.39
		< 0.001	< 0.001	< 0.001	< 0.001	0.002	0.004	0.004	0.003	0.034	0.006
BSO NGRIP T_{air}	NGRIP	–0.61	–0.74	–0.49	–0.67	*–0.12*	*–0.32*	*–0.11*	–0.35	*0.10*	*0.16*
	T_{air}	0.001	< 0.001	< 0.001	< 0.001	*0.564*	*0.120*	*0.445*	0.013	*0.651*	*0.275*
	MD95-2042 $U^{K'}_{37}$	–0.65	–0.68	–0.66	–0.68	*–0.17*	*–0.21*	*–0.23*	*–0.25*	*0.17*	*0.16*
		< 0.001	< 0.001	< 0.001	< 0.001	*0.404*	*0.318*	*0.118*	*0.088*	*0.427*	*0.272*
	MD95-2042 RI-OH′	–0.76	–0.72	–0.58	–0.61	*–0.25*	*–0.24*	*–0.16*	*–0.19*	*0.17*	*0.16*
		< 0.001	< 0.001	< 0.001	< 0.001	*0.235*	*0.255*	*0.275*	*0.185*	*0.427*	*0.272*
BSO NGRIP $\delta^{18}O_{ice}$	NGRIP	–0.69	–0.79	–0.49	–0.61	*–0.16*	*–0.33*	*–0.18*	–0.39	*0.19*	*0.25*
	T_{air}	< 0.001	< 0.001	< 0.001	< 0.001	*0.446*	*0.103*	*0.218*	0.005	*0.364*	*0.080*
	MD95-2042 $U^{K'}_{37}$	–0.73	–0.80	–0.63	–0.64	*–0.28*	*–0.38*	–0.29	–0.33	*0.30*	*0.25*
		< 0.001	< 0.001	< 0.001	< 0.001	*0.175*	*0.063*	0.041	0.022	*0.141*	*0.080*
	MD95-2042 RI-OH′	–0.87	–0.86	–0.58	–0.63	–0.44	–0.46	–0.29	–0.33	*0.30*	*0.25*
		< 0.001	< 0.001	< 0.001	< 0.001	0.029	0.020	0.041	0.022	*0.141*	*0.080*
BSO MD95-2042 $U^{K'}_{37}$	NGRIP	–0.90	–0.91	–0.52	–0.54	–0.63	–0.69	–0.38	–0.44	0.65	0.52
	T_{air}	< 0.001	< 0.001	< 0.001	< 0.001	0.001	< 0.001	0.010	0.002	< 0.001	< 0.001
	MD95-2042 $U^{K'}_{37}$	–0.94	–0.98	–0.81	–0.88	–0.75	–0.84	–0.67	–0.72	0.74	0.55
		< 0.001	< 0.001	< 0.001	< 0.001	< 0.001	< 0.001	< 0.001	< 0.001	< 0.001	< 0.001
	MD95-2042 RI-OH′	–0.93	–0.96	–0.71	–0.82	–0.85	–0.89	–0.61	–0.70	0.74	0.55
		< 0.001	< 0.001	< 0.001	< 0.001	< 0.001	< 0.001	< 0.001	< 0.001	< 0.001	< 0.001
BSO MD95-2042 RI-OH′	NGRIP	–0.82	–0.84	–0.48	–0.47	–0.49	–0.54	–0.33	–0.35	0.58	0.44
	T_{air}	< 0.001	< 0.001	< 0.001	< 0.001	0.015	0.007	0.026	0.017	0.003	0.002
	MD95-2042 $U^{K'}_{37}$	–0.86	–0.92	–0.74	–0.79	–0.66	–0.76	–0.60	–0.65	0.68	0.50
		< 0.001	< 0.001	< 0.001	< 0.001	< 0.001	< 0.001	< 0.001	< 0.001	< 0.001	< 0.001
	MD95-2042 RI-OH′	–0.97	–0.97	–0.80	–0.86	–0.87	–0.88	–0.69	–0.74	0.68	0.50
		< 0.001	< 0.001	< 0.001	< 0.001	< 0.001	< 0.001	< 0.001	< 0.001	< 0.001	< 0.001

Table S12. Monte Carlo results for correlation comparisons between different filtered and simulated Northern Hemisphere paleothermometric records after a band-pass filtering with a 500- to 16,000-y window. Each column indicates the 2.5th and 97.5th percentiles that define 95% confidence intervals. Negative differences indicate weaker correlations when using Greenland paleothermometric records than when using Iberian Margin paleothermometric records. Non-significant correlation differences are shown with grey numbers in italics. AA, Antarctic stack of EDC, EDML, and WD; and BSO, bipolar seesaw output.

			95% confidence intervals of changes in absolute coefficient correlation values for all DO-AIM pairs											
			$\Delta T_s \cdot \Delta t_n$ vs $\Delta T_n \cdot \Delta t_n$				ΔT_s vs $\Delta T_n \cdot \Delta t_n$				ΔT_s vs Δt_n			
SH record	NH records	Scenario	Pearson *r*		Kendall τ		Pearson *r*		Kendall τ		Pearson *r*		Kendall τ	
Filtered AA $\delta^{18}O_{ice}$ stack	From MD95-2042 $U^{K'}_{37}$	1	–0.11	< –0.01	–0.25	–0.10	–0.20	–0.08	–0.25	–0.10	–0.06	–0.02	*–0.05*	*0.04*
	to NGRIP T_{air}	2	*–0.07*	*0.02*	–0.23	–0.09	–0.15	–0.02	–0.18	–0.07	–0.06	–0.02	*–0.05*	*0.04*
	From MD95-2042 RI-OH′	1	–0.23	–0.13	–0.19	–0.05	–0.38	–0.27	–0.23	–0.09	–0.06	–0.02	*–0.05*	*0.04*
	to NGRIP T_{air}	2	–0.11	–0.04	–0.18	–0.07	–0.24	–0.13	–0.16	–0.03	–0.06	–0.02	*–0.05*	*0.04*
Filtered AA T_{air} stack	From MD95-2042 $U^{K'}_{37}$	1	–0.11	< –0.01	–0.25	–0.10	–0.21	–0.08	–0.25	–0.10	–0.06	–0.02	*–0.05*	*0.04*
	to NGRIP T_{air}	2	*–0.07*	*0.03*	–0.22	–0.09	–0.14	–0.02	–0.18	–0.07	–0.06	–0.02	*–0.05*	*0.04*
	From MD95-2042 RI-OH′	1	–0.22	–0.13	–0.19	–0.05	–0.38	–0.27	–0.23	–0.09	–0.06	–0.02	*–0.05*	*0.04*
	to NGRIP T_{air}	2	–0.11	–0.04	–0.18	–0.06	–0.23	–0.12	–0.16	–0.03	–0.06	–0.02	*–0.05*	*0.04*
BSO NGRIP T_{air}	From MD95-2042 $U^{K'}_{37}$	1	*–0.11*	*0.02*	–0.19	–0.07	*–0.11*	*< 0.01*	–0.17	–0.05	–0.08	–0.06	*–0.02*	*0.02*
	to NGRIP T_{air}	2	< 0.01	0.12	*–0.03*	*0.08*	0.06	0.16	0.06	0.16	–0.08	–0.06	*–0.02*	*0.02*
	From MD95-2042 RI-OH′	1	–0.20	–0.11	–0.14	–0.03	–0.17	–0.09	–0.12	–0.01	–0.08	–0.06	*–0.02*	*0.02*
	to NGRIP T_{air}	2	*–0.02*	*0.06*	0.04	0.13	0.04	0.12	0.12	0.21	–0.08	–0.06	*–0.02*	*0.02*
BSO NGRIP $\delta^{18}O_{ice}$	From MD95-2042 $U^{K'}_{37}$	1	*–0.10*	*0.01*	–0.19	–0.06	–0.18	–0.06	–0.15	–0.03	–0.12	–0.10	*–0.01*	*0.03*
	to NGRIP T_{air}	2	*–0.05*	*0.04*	*–0.09*	*0.03*	*–0.10*	*0.01*	0.03	0.13	–0.12	–0.10	*–0.01*	*0.03*
	From MD95-2042 RI-OH′	1	–0.23	–0.14	–0.16	–0.05	–0.32	–0.23	–0.16	–0.05	–0.12	–0.10	*–0.01*	*0.03*
	to NGRIP T_{air}	2	–0.10	–0.03	*–0.08*	*0.03*	–0.17	–0.09	0.03	0.13	–0.12	–0.10	*–0.01*	*0.03*
BSO MD95-2042 $U^{K'}_{37}$	From MD95-2042 $U^{K'}_{37}$	1	–0.07	–0.02	–0.33	–0.20	–0.17	–0.09	–0.32	–0.20	–0.10	–0.07	*–0.07*	*< 0.01*
	to NGRIP T_{air}	2	–0.08	–0.05	*–0.36*	*–0.25*	–0.19	–0.12	–0.30	–0.19	–0.10	–0.07	*–0.07*	*< 0.01*
	From MD95-2042 RI-OH′	1	*–0.06*	*< 0.01*	–0.25	–0.13	–0.25	–0.19	–0.28	–0.16	–0.10	–0.07	*–0.07*	*< 0.01*
	to NGRIP T_{air}	2	–0.07	–0.03	–0.30	–0.19	–0.23	–0.18	–0.28	–0.17	–0.10	–0.07	*–0.07*	*< 0.01*
BSO MD95-2042 RI-OH′	From MD95-2042 $U^{K'}_{37}$	1	*–0.07*	*0.01*	–0.29	–0.17	–0.21	–0.11	–0.30	–0.17	–0.11	–0.10	*–0.07*	*< 0.01*
	to NGRIP T_{air}	2	–0.10	–0.04	–0.33	–0.22	–0.26	–0.18	–0.32	–0.21	–0.11	–0.10	*–0.07*	*< 0.01*
	From MD95-2042 RI-OH′	1	–0.18	–0.13	–0.38	–0.28	–0.41	–0.35	–0.41	–0.30	–0.11	–0.10	*–0.07*	*< 0.01*
	to NGRIP T_{air}	2	–0.15	–0.11	–0.42	–0.33	–0.37	–0.31	–0.43	–0.32	–0.11	–0.10	*–0.07*	*< 0.01*

Table S13. Bootstrap results for correlation comparisons between different filtered and simulated Northern Hemisphere paleothermometric records after a band-pass filtering with a 500- to 16,000-y window. Each column indicates the 2.5th and 97.5th percentiles that define 95% confidence intervals. Negative differences indicate weaker correlations when using Greenland paleothermometric records than when using Iberian Margin paleothermometric records. Non-significant correlation differences are shown with grey numbers in italics. AA, Antarctic stack of EDC, EDML, and WD; and BSO, bipolar seesaw output.

			95% confidence intervals of changes in absolute coefficient correlation values for all DO-AIM pairs											
			$\Delta T_s \cdot \Delta t_n$ vs $\Delta T_n \cdot \Delta t_n$				ΔT_s vs $\Delta T_n \cdot \Delta t_n$				ΔT_s vs Δt_n			
SH record	NH records	Scenario	Pearson *r*		Kendall τ		Pearson *r*		Kendall τ		Pearson *r*		Kendall τ	
Filtered AA $\delta^{18}O_{ice}$ stack	From MD95-2042 $U^{K'}_{37}$	1	*–0.24*	*0.03*	–0.41	–0.01	–0.42	< –0.01	*–0.43*	*0.10*	*–0.20*	*0.12*	*–0.18*	*0.16*
	to NGRIP T_{air}	2	*–0.33*	*0.04*	*–0.41*	*0.01*	*–0.31*	*0.04*	*–0.38*	*0.07*	*–0.20*	*0.12*	*–0.18*	*0.16*
	From MD95-2042 RI-OH′	1	–0.36	–0.03	*–0.34*	*0.14*	–0.50	–0.08	*–0.40*	*0.13*	*–0.20*	*0.12*	*–0.18*	*0.16*
	to NGRIP T_{air}	2	*–0.38*	*0.03*	*–0.38*	*0.08*	*–0.42*	*< 0.01*	*–0.37*	*0.13*	*–0.20*	*0.12*	*–0.18*	*0.16*
Filtered AA T_{air} stack	From MD95-2042 $U^{K'}_{37}$	1	*–0.24*	*0.03*	–0.40	–0.01	–0.42	–0.01	*–0.44*	*0.09*	*–0.19*	*0.12*	*–0.17*	*0.17*
	to NGRIP T_{air}	2	*–0.32*	*0.04*	*–0.41*	*0.01*	*–0.31*	*0.04*	*–0.38*	*0.07*	*–0.19*	*0.12*	*–0.17*	*0.17*
	From MD95-2042 RI-OH′	1	–0.36	–0.03	*–0.33*	*0.16*	–0.50	–0.07	*–0.40*	*0.13*	*–0.19*	*0.12*	*–0.17*	*0.17*
	to NGRIP T_{air}	2	*–0.38*	*0.03*	*–0.38*	*0.08*	*–0.42*	*0.02*	*–0.37*	*0.13*	*–0.19*	*0.12*	*–0.17*	*0.17*
BSO NGRIP T_{air}	From MD95-2042 $U^{K'}_{37}$	1	*–0.26*	*0.08*	*–0.46*	*0.08*	*–0.24*	*0.13*	*–0.31*	*0.18*	*–0.19*	*0.20*	*–0.14*	*0.17*
	to NGRIP T_{air}	2	*–0.10*	*0.14*	*–0.26*	*0.21*	*–0.09*	*0.35*	*–0.12*	*0.34*	*–0.19*	*0.20*	*–0.14*	*0.17*
	From MD95-2042 RI-OH′	1	*–0.28*	*0.09*	*–0.40*	*0.21*	*–0.32*	*0.19*	*–0.25*	*0.23*	*–0.19*	*0.20*	*–0.14*	*0.17*
	to NGRIP T_{air}	2	*–0.12*	*0.21*	*–0.24*	*0.33*	*–0.15*	*0.44*	*–0.10*	*0.42*	*–0.19*	*0.20*	*–0.14*	*0.17*
BSO NGRIP $\delta^{18}O_{ice}$	From MD95-2042 $U^{K'}_{37}$	1	*–0.32*	*0.05*	*–0.36*	*0.07*	*–0.33*	*0.07*	*–0.32*	*0.15*	*–0.25*	*0.17*	*–0.15*	*0.16*
	to NGRIP T_{air}	2	*–0.29*	*0.07*	*–0.23*	*0.18*	*–0.22*	*0.12*	*–0.15*	*0.28*	*–0.25*	*0.17*	*–0.15*	*0.16*
	From MD95-2042 RI-OH′	1	–0.44	–0.01	*–0.36*	*0.18*	–0.42	–0.01	*–0.32*	*0.16*	*–0.25*	*0.17*	*–0.15*	*0.16*
	to NGRIP T_{air}	2	*–0.34*	*0.05*	*–0.26*	*0.21*	*–0.31*	*0.11*	*–0.19*	*0.32*	*–0.25*	*0.17*	*–0.15*	*0.16*
BSO MD95-2042 $U^{K'}_{37}$	From MD95-2042 $U^{K'}_{37}$	1	–0.27	–0.01	–0.54	–0.07	–0.41	–0.03	–0.56	–0.07	*–0.26*	*0.04*	*–0.21*	*0.19*
	to NGRIP T_{air}	2	–0.40	–0.02	–0.59	–0.12	–0.39	–0.02	–0.52	–0.05	*–0.26*	*0.04*	*–0.21*	*0.19*
	From MD95-2042 RI-OH′	1	*–0.40*	*0.04*	*–0.43*	*0.03*	–0.51	–0.10	*–0.47*	*0.01*	*–0.26*	*0.04*	*–0.21*	*0.19*
	to NGRIP T_{air}	2	*–0.43*	*< 0.01*	–0.57	–0.04	–0.41	–0.08	–0.56	–0.01	*–0.26*	*0.04*	*–0.21*	*0.19*
BSO MD95-2042 RI-OH′	From MD95-2042 $U^{K'}_{37}$	1	*–0.31*	*0.02*	–0.46	–0.06	–0.46	–0.04	–0.50	–0.07	*–0.28*	*0.05*	*–0.23*	*0.12*
	to NGRIP T_{air}	2	–0.51	< –0.01	–0.57	–0.10	–0.53	–0.02	–0.55	–0.06	*–0.28*	*0.05*	*–0.23*	*0.12*
	From MD95-2042 RI-OH′	1	–0.53	–0.04	–0.54	–0.11	–0.64	–0.19	–0.56	–0.16	*–0.28*	*0.05*	*–0.23*	*0.12*
	to NGRIP T_{air}	2	–0.60	–0.03	–0.67	–0.15	–0.62	–0.12	–0.65	–0.14	*–0.28*	*0.05*	*–0.23*	*0.12*

Table S14. Correlation results for Southern versus Northern Hemisphere diagrams restricted to Heinrich and Heinrich-like stadials and to other Dansgaard–Oeschger stadials using filtered and simulated paleothermometric records after a band-pass filtering with a 500- to 16,000-y window. As Table S11, but considering only Heinrich and Heinrich-like stadials (H) and only other Dansgaard–Oeschger stadials (DO). Non-significant correlation differences are shown with grey numbers in italics. AA, Antarctic stack of EDC, EDML, and WD; and BSO, bipolar seesaw output.

		Correlation coefficients and *p*-values for only H and H-like stadials (n = 14) and for only other DO stadials (n = 11, except for Iberian Margin BSOs where n = 10)																			
		$\Delta T_s \cdot \Delta t_n$ vs $\Delta T_n \cdot \Delta t_n$								ΔT_s vs $\Delta T_n \cdot \Delta t_n$								ΔT_s vs Δt_n			
		Pearson r				Kendall τ				Pearson r				Kendall τ				Pearson r		Kendall τ	
		1	2	1	2	1	2	1	2	1	2	1	2	1	2	1	2				
SH record	NH record	H	DO	H	DO	H	DO	H	DO	H	DO	H	DO	H	DO	H	DO	H	DO	H	DO
Filtered AA $\delta^{18}O_{ice}$ stack	NGRIP	–0.64	*–0.55*	–0.74	–0.77	–0.45	*–0.31*	–0.45	–0.56	*0.09*	*–0.16*	*–0.10*	*–0.42*	*0.08*	*0.05*	*–0.10*	*–0.13*	*–0.01*	*0.31*	*–0.01*	*0.13*
	T_{air}	0.014	*0.081*	0.002	0.006	0.026	*0.218*	0.026	0.017	*0.772*	*0.645*	*0.743*	*0.193*	*0.747*	*0.879*	*0.667*	*0.648*	*0.962*	*0.355*	*1.000*	*0.648*
	MD95-2042	–0.67	–0.78	–0.71	–0.77	–0.67	–0.64	–0.67	–0.60	*–0.03*	*–0.49*	*–0.09*	*–0.50*	*–0.10*	*–0.38*	*–0.14*	*–0.42*	*0.02*	*0.39*	*0.03*	*0.29*
	$U^{K'}_{37}$	0.008	0.005	0.004	0.005	< 0.001	0.006	< 0.001	0.010	*0.908*	*0.129*	*0.760*	*0.120*	*0.667*	*0.121*	*0.518*	*0.087*	*0.948*	*0.234*	*0.914*	*0.212*
	MD95-2042	–0.86	*–0.31*	–0.80	–0.60	–0.71	*–0.24*	–0.69	*–0.45*	*–0.29*	*–0.25*	*–0.26*	*–0.35*	*–0.23*	*–0.13*	*–0.21*	*–0.20*	*0.02*	*0.39*	*0.03*	*0.29*
	RI-OH′	< 0.001	*0.353*	< 0.001	0.049	< 0.001	*0.359*	< 0.001	*0.060*	*0.310*	*0.456*	*0.374*	*0.290*	*0.279*	*0.648*	*0.331*	*0.445*	*0.948*	*0.234*	*0.914*	*0.212*
Filtered AA T_{air} stack	NGRIP	–0.64	*–0.55*	–0.74	–0.77	–0.45	*–0.31*	–0.45	–0.56	*0.09*	*–0.16*	*–0.10*	*–0.42*	*0.10*	*0.05*	*–0.08*	*–0.13*	*–0.01*	*0.31*	*0.01*	*0.13*
	T_{air}	0.014	*0.077*	0.002	0.006	0.026	*0.218*	0.026	0.017	*0.773*	*0.641*	*0.735*	*0.197*	*0.667*	*0.879*	*0.747*	*0.648*	*0.965*	*0.362*	*1.000*	*0.648*
	MD95-2042	–0.67	–0.78	–0.71	–0.77	–0.65	–0.64	–0.65	–0.60	*–0.04*	*–0.48*	*–0.09*	*–0.50*	*–0.12*	*–0.38*	*–0.12*	*–0.42*	*0.02*	*0.39*	*0.01*	*0.29*
	$U^{K'}_{37}$	0.008	0.005	0.005	0.005	< 0.001	0.006	< 0.001	0.010	*0.904*	*0.132*	*0.772*	*0.120*	*0.591*	*0.121*	*0.591*	*0.087*	*0.955*	*0.233*	*1.000*	*0.212*
	MD95-2042	–0.85	*–0.31*	–0.79	–0.60	–0.69	*–0.24*	–0.67	*–0.45*	*–0.28*	*–0.24*	*–0.25*	*–0.35*	*–0.21*	*–0.13*	*–0.19*	*–0.20*	*0.02*	*0.39*	*0.01*	*0.29*
	RI-OH′	< 0.001	*0.359*	< 0.001	0.050	< 0.001	*0.359*	< 0.001	*0.060*	*0.328*	*0.471*	*0.399*	*0.295*	*0.331*	*0.648*	*0.388*	*0.445*	*0.955*	*0.233*	*1.000*	*0.212*
BSO NGRIP T_{air}	NGRIP	*–0.51*	*–0.39*	–0.67	–0.81	–0.41	*–0.05*	–0.63	*–0.38*	*–0.08*	*–0.27*	*–0.29*	–0.69	*–0.05*	*–0.02*	*–0.27*	*–0.35*	*0.03*	*0.20*	*0.03*	*0.27*
	T_{air}	0.062	*0.235*	0.009	0.002	0.047	*0.879*	0.001	*0.121*	*0.783*	*0.424*	*0.323*	0.020	*0.830*	*1.000*	*0.193*	*0.165*	*0.913*	*0.548*	*0.914*	*0.283*
	MD95-2042	–0.54	–0.67	–0.57	*–0.56*	–0.60	–0.67	–0.69	–0.64	*–0.14*	*–0.55*	*–0.20*	*–0.43*	*–0.19*	*–0.38*	*–0.27*	*–0.35*	*0.12*	*0.34*	*0.12*	*0.15*
	$U^{K'}_{37}$	0.047	0.026	0.032	*0.075*	0.002	0.003	< 0.001	0.006	*0.630*	*0.082*	*0.491*	*0.190*	*0.388*	*0.121*	*0.193*	*0.165*	*0.678*	*0.305*	*0.591*	*0.532*
	MD95-2042	–0.72	*–0.02*	–0.64	*–0.17*	–0.65	*–0.35*	–0.67	*–0.42*	*–0.31*	*–0.02*	*–0.29*	*–0.05*	*–0.23*	*–0.13*	*–0.30*	*–0.13*	*0.12*	*0.34*	*0.12*	*0.15*
	RI-OH′	0.004	*0.946*	0.013	*0.623*	< 0.001	*0.165*	< 0.001	*0.087*	*0.277*	*0.962*	*0.313*	*0.892*	*0.279*	*0.648*	*0.157*	*0.648*	*0.678*	*0.305*	*0.591*	*0.532*
BSO NGRIP $\delta^{18}O_{ice}$	NGRIP	–0.59	*–0.44*	–0.74	*–0.68*	*–0.32*	*–0.27*	–0.54	*–0.45*	*0.00*	*–0.22*	*–0.21*	*–0.50*	*–0.05*	*–0.05*	*–0.27*	*–0.31*	*–0.03*	*0.47*	*0.03*	*0.31*
	T_{air}	0.027	*0.181*	0.003	*0.020*	*0.127*	*0.283*	0.007	*0.060*	*0.988*	*0.514*	*0.478*	*0.117*	*0.830*	*0.879*	*0.193*	*0.218*	*0.922*	*0.146*	*0.914*	*0.218*
	MD95-2042	–0.61	–0.62	–0.71	*–0.49*	–0.54	–0.49	–0.63	*–0.38*	*–0.13*	*–0.30*	*–0.27*	*–0.17*	*–0.23*	*–0.27*	*–0.36*	*–0.24*	*0.14*	*0.26*	*0.16*	*0.18*
	$U^{K'}_{37}$	0.020	0.043	0.005	*0.129*	0.007	0.041	0.001	*0.121*	*0.656*	*0.370*	*0.356*	*0.614*	*0.279*	*0.283*	*0.079*	*0.359*	*0.629*	*0.435*	*0.451*	*0.435*
	MD95-2042	–0.82	*–0.31*	–0.80	*–0.42*	–0.58	*–0.24*	–0.65	*–0.31*	*–0.35*	*–0.29*	*–0.39*	*–0.20*	*–0.32*	*–0.24*	–0.43	*–0.16*	*0.14*	*0.26*	*0.16*	*0.18*
	RI-OH′	< 0.001	*0.356*	< 0.001	*0.196*	0.003	*0.359*	< 0.001	*0.218*	*0.223*	*0.392*	*0.166*	*0.560*	*0.127*	*0.359*	0.036	*0.542*	*0.629*	*0.435*	*0.451*	*0.435*
BSO MD95-2042 $U^{K'}_{37}$	NGRIP	–0.87	*0.15*	–0.91	*–0.38*	–0.49	*0.24*	–0.49	*–0.16*	*–0.50*	*0.29*	–0.61	*–0.18*	*–0.25*	*0.42*	*–0.38*	*0.02*	*0.43*	*–0.01*	*0.36*	*–0.07*
	T_{air}	< 0.001	*0.675*	< 0.001	*0.284*	0.014	*0.381*	0.014	*0.601*	*0.068*	*0.420*	0.021	*0.621*	*0.233*	*0.108*	*0.062*	*1.000*	*0.122*	*0.979*	*0.079*	*0.862*
	MD95-2042	–0.91	–0.87	–0.97	–0.94	–0.69	–0.64	–0.82	–0.78	–0.62	–0.64	–0.75	–0.71	–0.52	–0.51	–0.65	–0.56	0.56	*0.21*	0.41	*0.13*
	$U^{K'}_{37}$	< 0.001	< 0.001	< 0.001	< 0.001	< 0.001	0.009	< 0.001	< 0.001	0.019	0.047	0.002	0.020	0.010	0.047	< 0.001	0.029	0.037	*0.565*	0.047	*0.590*
	MD95-2042	–0.90	*–0.34*	–0.95	–0.75	–0.74	*–0.24*	–0.85	–0.51	–0.74	*–0.33*	–0.82	*–0.58*	–0.56	*–0.29*	–0.71	*–0.47*	0.56	*0.21*	0.41	*0.13*
	RI-OH′	< 0.001	*0.343*	< 0.001	0.012	< 0.001	*0.381*	< 0.001	0.047	0.003	*0.354*	< 0.001	*0.076*	0.005	*0.291*	< 0.001	*0.073*	0.037	*0.565*	0.047	*0.590*
BSO MD95-2042 RI-OH′	NGRIP	–0.77	*0.27*	–0.82	*0.03*	*–0.38*	*0.24*	–0.43	*0.11*	*–0.29*	*0.38*	*–0.39*	*0.19*	*–0.16*	*0.38*	*–0.25*	*0.16*	*0.32*	*–0.11*	*0.27*	*–0.20*
	T_{air}	0.001	*0.447*	< 0.001	*0.938*	*0.062*	*0.381*	0.036	*0.727*	*0.312*	*0.273*	*0.166*	*0.591*	*0.451*	*0.156*	*0.233*	*0.601*	*0.268*	*0.770*	*0.193*	*0.484*
	MD95-2042	–0.79	*–0.54*	–0.88	*–0.56*	–0.67	*–0.42*	–0.80	*–0.47*	*–0.46*	*–0.15*	–0.61	*–0.17*	–0.47	*–0.29*	–0.60	*–0.33*	*0.49*	*–0.20*	*0.36*	*0.00*
	$U^{K'}_{37}$	< 0.001	*0.108*	< 0.001	*0.089*	< 0.001	*0.108*	< 0.001	*0.073*	*0.096*	*0.677*	0.019	*0.633*	0.019	*0.291*	0.002	*0.216*	*0.074*	*0.579*	*0.079*	*1.000*
	MD95-2042	–0.97	–0.73	–0.97	–0.87	–0.80	*–0.47*	–0.91	–0.64	–0.78	*–0.53*	–0.81	*–0.46*	–0.65	*–0.33*	–0.71	–0.51	*0.49*	*–0.20*	*0.36*	*0.00*
	RI-OH′	< 0.001	0.016	< 0.001	0.001	< 0.001	*0.073*	< 0.001	0.009	< 0.001	*0.118*	< 0.001	*0.181*	< 0.001	*0.216*	< 0.001	0.047	*0.074*	*0.579*	*0.079*	*1.000*

Table S15. Pearson correlation results for Southern versus Northern Hemisphere diagrams using Antarctic temperature amplitudes and Greenland event durations. Correlations with the main Southern Hemisphere record used in this study and correlations previously published are shown with bold text and numbers. The Southern versus Northern Hemisphere diagrams are Antarctic temperature amplitudes (ΔT_s) versus Greenland cold event durations (Δt_n) diagrams, i.e. classical ΔT_s versus Δt_n diagrams such as those presented in refs. 81, 82, 83, and 84. Pearson correlation results for only DO12 to DO3 as in ref. 81, all Marine Isotope Stage 3 (MIS3) events (DO16 to DO3), only early MIS 3 events (DO16 to DO10) and only late MIS 3 events (DO9 to DO3) as in ref. 84 are shown. "GICC05" and "GICC05modelext*1.0063" refer to the Greenland chronologies used by refs. 81 and 84, respectively. AA, Antarctic stack of EDC, EDML, and WD (this study) and five-core Antarctic average (89); ATS, Antarctic Temperature Stack (71) and N/A, not applicable.

		Pearson *r*			
Antarctic record	Greenland chronology	DO12 to DO3 (*n* = 11)	DO16 to DO3 (*n* = 14)	DO16 to DO10 (*n* = 6)	DO9 to DO3 (*n* = 8)
AA $\delta^{18}O_{ice}$ stack This study	**This study**	**0.61**	**0.60**	**0.94**	**0.63**
	GICC05modelext*1.0063	**0.67**	**0.64**	**0.95**	**0.65**
	GICC05	**0.72**	**N/A**	**N/A**	**N/A**
AA T_{air} stack This study	This study	0.60	0.59	0.94	0.61
	GICC05modelext*1.0063	0.66	0.62	0.95	0.64
	GICC05	0.71	N/A	N/A	N/A
ATS Parrenin et al. (2013)	This study	0.67	0.66	0.86	0.62
	GICC05modelext*1.0063	0.71	0.68	0.87	0.63
	GICC05modelext	0.75	N/A	N/A	N/A
AA $\delta^{18}O_{ice}$ stack Buizert et al. (2018)	This study	0.59	0.53	0.88	0.61
	GICC05modelext*1.0063	0.65	**0.59**	**0.95**	**0.63**
	GICC05	0.71	N/A	N/A	N/A
EDML T_{air} EPICA Community Members (2006)	This study	0.80	0.80	0.88	0.81
	GICC05modelext*1.0063	0.85	0.85	0.90	0.85
	GICC05modelext	**0.92**	N/A	N/A	N/A

Table S16. Goodness-of-fit results with 95% confidence intervals for bipolar seesaw model output versus reference record comparisons for lag = 0 y. The 95% confidence intervals (CI) with the 2.5th and 97.5th percentiles are derived from 1,000 Monte Carlo iterations (*Materials and Methods*). "Short window" and "Long window" refer to band-pass filtering with a 500- to 10,000-y window and 500- to 16,000-y window, respectively. Each mean squared error (MSE) expressed in squared normalized °C was calculated from the records normalized to zero means and unit standard deviations over the 115 to 12 ka BP period shown in Figs. 4*A* and S17*A*. Opposite values of the IVC benthic foraminiferal $\delta^{18}O$ record are used when comparing with bipolar seesaw model outputs from biomarker-based SST records. AA, Antarctic stack of EDC, EDML, and WD; and BSO, bipolar seesaw output.

		Short window									Long window								
		Pearson *r*			Kendall τ			MSE			Pearson *r*			Kendall τ			MSE		
Comparison	Period	Value	95% CI		Value	95% CI		Value	95% CI		Value	95% CI		Value	95% CI		Value	95% CI	
BSO NGRIP T_{air}	115 to 12 ka BP	0.52	0.50	0.53	0.33	0.32	0.34	0.96	0.95	1.00	0.53	0.51	0.53	0.34	0.33	0.35	0.95	0.93	0.98
vs	43 to 12 ka BP	0.59	0.56	0.61	0.38	0.36	0.40	0.88	0.83	0.93	0.53	0.50	0.55	0.34	0.32	0.36	0.79	0.75	0.83
AA $\delta^{18}O_{ice}$ stack	115 to 45 ka BP	0.50	0.48	0.51	0.31	0.29	0.32	0.99	0.97	1.05	0.53	0.51	0.54	0.34	0.33	0.35	1.01	0.99	1.06
BSO NGRIP $\delta^{18}O_{ice}$	115 to 12 ka BP	0.56	0.54	0.57	0.37	0.35	0.37	0.87	0.86	0.92	0.56	0.54	0.57	0.36	0.34	0.36	0.88	0.86	0.92
vs	43 to 12 ka BP	0.63	0.60	0.66	0.44	0.41	0.46	0.78	0.73	0.85	0.58	0.55	0.60	0.37	0.34	0.40	0.67	0.63	0.73
AA $\delta^{18}O_{ice}$ stack	115 to 45 ka BP	0.55	0.52	0.56	0.34	0.31	0.35	0.93	0.91	0.99	0.56	0.53	0.57	0.35	0.33	0.36	0.99	0.97	1.04
BSO MD95-2042 $U^{K'}_{37}$	115 to 12 ka BP	0.59	0.56	0.61	0.42	0.40	0.43	0.81	0.79	0.87	0.61	0.59	0.63	0.42	0.40	0.44	0.77	0.75	0.83
vs	43 to 12 ka BP	0.77	0.74	0.78	0.57	0.54	0.58	0.53	0.50	0.59	0.63	0.60	0.65	0.42	0.39	0.44	0.60	0.56	0.65
AA $\delta^{18}O_{ice}$ stack	115 to 45 ka BP	0.54	0.51	0.56	0.37	0.34	0.39	0.95	0.91	1.03	0.61	0.58	0.63	0.43	0.40	0.45	0.86	0.82	0.94
BSO MD95-2042 RI-OH′	115 to 12 ka BP	0.63	0.61	0.64	0.44	0.42	0.44	0.73	0.72	0.77	0.67	0.65	0.67	0.47	0.46	0.48	0.67	0.66	0.70
vs	43 to 12 ka BP	0.78	0.76	0.79	0.56	0.54	0.57	0.52	0.50	0.56	0.69	0.67	0.70	0.48	0.46	0.49	0.59	0.56	0.62
AA $\delta^{18}O_{ice}$ stack	115 to 45 ka BP	0.56	0.53	0.57	0.38	0.36	0.40	0.82	0.80	0.88	0.66	0.64	0.67	0.48	0.46	0.49	0.71	0.69	0.75
BSO MD95-2042 $U^{K'}_{37}$	115 to 12 ka BP	0.46	0.31	0.45	0.30	0.19	0.29	1.08	1.10	1.38	0.48	0.35	0.48	0.32	0.23	0.32	1.04	1.05	1.30
vs	43 to 12 ka BP	0.40	0.21	0.43	0.25	0.13	0.27	0.84	0.78	1.13	0.39	0.24	0.43	0.28	0.17	0.30	0.98	0.88	1.20
MD95-2042 IVC $\delta^{18}O$ benthic	115 to 45 ka BP	0.47	0.31	0.48	0.31	0.19	0.32	1.20	1.19	1.58	0.51	0.36	0.51	0.34	0.23	0.34	1.09	1.09	1.42
BSO MD95-2042 RI-OH′	115 to 12 ka BP	0.43	0.29	0.42	0.27	0.18	0.27	1.15	1.16	1.41	0.46	0.34	0.46	0.30	0.22	0.31	1.07	1.08	1.31
vs	43 to 12 ka BP	0.37	0.19	0.42	0.25	0.13	0.28	1.15	1.07	1.46	0.34	0.21	0.38	0.26	0.17	0.29	1.22	1.12	1.45
MD95-2042 IVC $\delta^{18}O$ benthic	115 to 45 ka BP	0.45	0.30	0.45	0.28	0.18	0.29	1.16	1.15	1.49	0.51	0.37	0.51	0.32	0.22	0.34	1.02	1.02	1.34
BSO MD95-2042 IVC $\delta^{18}O$ *G. bulloides*	115 to 12 ka BP	0.40	0.26	0.40	0.25	0.16	0.26	1.21	1.20	1.48	0.40	0.28	0.41	0.25	0.17	0.27	1.21	1.18	1.45
vs	43 to 12 ka BP	0.21	0.05	0.28	0.12	0.02	0.17	1.09	0.95	1.34	0.16	0.04	0.24	0.11	0.03	0.16	1.31	1.13	1.53
MD95-2042 IVC $\delta^{18}O$ benthic	115 to 45 ka BP	0.44	0.28	0.45	0.29	0.18	0.30	1.29	1.27	1.66	0.47	0.32	0.48	0.31	0.20	0.32	1.19	1.16	1.53

Table S17. Monte Carlo results for goodness-of-fit comparisons between different bipolar seesaw model outputs for lag = 0 y. Each column indicates the 2.5th and 97.5th percentiles that define 95% confidence intervals. Negative differences in correlation coefficients and positive differences in mean squared error (MSE) indicate improved goodness-of-fit when switching from Greenland T_{air} to Greenland $\delta^{18}O_{ice}$, when switching from Iberian Margin $U^{K'}_{37}$ to Iberian Margin RI-OH′, when switching from Greenland to Iberian Margin paleothermometric records, and when switching from the Iberian Margin ice-volume–corrected (IVC) foraminiferal-based record to Iberian Margin biomarker-based paleothermometric records as bipolar seesaw inputs. "Short window" and "Long window" refer to band-pass filtering with a 500- to 10,000-y window and 500- to 16,000-y window, respectively. Each MSE expressed in squared normalized °C was calculated from the records normalized to zero means and unit standard deviations over the 115 to 12 ka BP period shown in Figs. 4*A* and S17*A*. Opposite values of the IVC benthic foraminiferal $\delta^{18}O$ record are used when comparing with bipolar seesaw model outputs from biomarker-based SST records. Non-significant goodness-of-fit differences are shown with grey numbers in italics. AA, Antarctic stack of EDC, EDML, and WD; and BSO, bipolar seesaw output.

		Short window						Long window					
Reference	Comparison	Period	Pearson *r*		Kendall τ		MSE		Pearson *r*		Kendall τ		MSE	
AA $\delta^{18}O_{ice}$ stack	BSO NGRIP T_{air}	115 to 12 ka BP	–0.06	–0.03	–0.05	–0.02	0.05	0.12	–0.05	–0.02	–0.03	< –0.01	0.04	0.10
	vs	43 to 12 ka BP	–0.08	–0.01	–0.09	–0.02	0.02	0.15	–0.08	–0.02	–0.07	< –0.01	0.05	0.17
	BSO NGRIP $\delta^{18}O_{ice}$	115 to 45 ka BP	–0.06	–0.03	–0.04	–0.01	0.02	0.10	–0.04	< –0.01	*–0.02*	*0.01*	*–0.02*	*0.06*
	BSO MD95-2042 $U^{K'}_{37}$	115 to 12 ka BP	–0.06	–0.02	–0.04	< –0.01	0.04	0.13	–0.07	–0.03	–0.07	–0.03	0.07	0.15
	vs	43 to 12 ka BP	–0.03	< –0.01	*–0.01*	*0.02*	*–0.02*	*0.04*	–0.07	–0.04	–0.07	–0.04	*–0.02*	*0.04*
	BSO MD95-2042 RI-OH′	115 to 45 ka BP	*–0.05*	*0.01*	*–0.04*	*0.01*	0.06	0.19	–0.08	–0.03	–0.08	–0.03	0.10	0.22
	BSO NGRIP T_{air}	115 to 12 ka BP	–0.09	–0.05	–0.10	–0.07	0.10	0.19	–0.11	–0.06	–0.10	–0.06	0.12	0.21
	vs	43 to 12 ka BP	–0.20	–0.15	–0.20	–0.15	0.29	0.39	–0.13	–0.07	–0.11	–0.05	0.13	0.24
	BSO MD95-2042 $U^{K'}_{37}$	115 to 45 ka BP	–0.07	–0.01	–0.08	–0.03	*–0.02*	*0.10*	–0.10	–0.05	–0.11	–0.06	0.08	0.20
	BSO NGRIP T_{air}	115 to 12 ka BP	–0.13	–0.10	–0.12	–0.09	0.20	0.26	–0.15	–0.13	–0.14	–0.12	0.25	0.31
	vs	43 to 12 ka BP	–0.21	–0.17	–0.20	–0.15	0.30	0.39	–0.18	–0.13	–0.16	–0.11	0.15	0.24
	BSO MD95-2042 RI-OH′	115 to 45 ka BP	–0.08	–0.04	–0.09	–0.06	0.13	0.21	–0.15	–0.11	–0.16	–0.12	0.27	0.34
	BSO NGRIP $\delta^{18}O_{ice}$	115 to 12 ka BP	–0.05	< –0.01	–0.07	–0.03	0.01	0.11	–0.07	–0.03	–0.09	–0.04	0.06	0.15
	vs	43 to 12 ka BP	–0.17	–0.10	–0.16	–0.09	0.18	0.31	–0.09	–0.02	–0.08	–0.01	0.02	0.13
	BSO MD95-2042 $U^{K'}_{37}$	115 to 45 ka BP	*–0.02*	*0.03*	–0.05	< –0.01	*–0.08*	*0.04*	–0.08	–0.02	–0.10	–0.05	0.06	0.19
	BSO NGRIP $\delta^{18}O_{ice}$	115 to 12 ka BP	–0.09	–0.05	–0.09	–0.06	0.11	0.18	–0.12	–0.09	–0.13	–0.10	0.18	0.25
	vs	43 to 12 ka BP	–0.18	–0.12	–0.15	–0.09	0.20	0.32	–0.14	–0.08	–0.13	–0.07	0.04	0.14
	BSO MD95-2042 RI-OH′	115 to 45 ka BP	*–0.04*	*0.01*	–0.06	–0.03	0.06	0.15	–0.13	–0.09	–0.15	–0.11	0.24	0.33
MD95-2042 IVC $\delta^{18}O$ benthic	BSO MD95-2042 $U^{K'}_{37}$	115 to 12 ka BP	*< –0.01*	*0.06*	*< –0.01*	*0.04*	*–0.12*	*0.01*	*–0.01*	*0.04*	*–0.01*	*0.04*	*–0.07*	*0.03*
	vs	43 to 12 ka BP	*–0.02*	*0.06*	*–0.02*	*0.02*	–0.39	–0.23	0.01	0.08	*–0.02*	*0.04*	–0.30	–0.18
	BSO MD95-2042 RI-OH′	115 to 45 ka BP	*–0.02*	*0.05*	*–0.01*	*0.05*	*–0.02*	*0.15*	*–0.04*	*0.02*	*–0.02*	*0.04*	< 0.01	0.15
	BSO MD95-2042 IVC $\delta^{18}O$ *G. bulloides*	115 to 12 ka BP	–0.10	–0.01	–0.07	–0.01	0.02	0.20	–0.11	–0.03	–0.09	–0.03	0.06	0.23
	vs	43 to 12 ka BP	–0.22	–0.09	–0.15	–0.06	0.07	0.32	–0.25	–0.14	–0.19	–0.09	0.17	0.41
	BSO MD95-2042 $U^{K'}_{37}$	115 to 45 ka BP	*–0.08*	*0.02*	*–0.06*	*0.02*	*–0.06*	*0.20*	*–0.09*	*0.02*	*–0.07*	*0.01*	*–0.04*	*0.20*
	BSO MD95-2042 IVC $\delta^{18}O$ *G. bulloides*	115 to 12 ka BP	*–0.07*	*0.01*	*–0.05*	*< 0.01*	*–0.02*	*0.13*	–0.10	–0.02	–0.07	–0.01	0.05	0.20
	vs	43 to 12 ka BP	–0.20	–0.07	–0.15	–0.07	*–0.26*	*0.03*	–0.21	–0.09	–0.17	–0.09	*–0.07*	*0.15*
	BSO MD95-2042 RI-OH′	115 to 45 ka BP	*–0.06*	*0.03*	*–0.03*	*0.04*	0.04	0.24	*–0.09*	*< 0.01*	*–0.05*	*0.02*	0.06	0.27

Table S18. Cross-correlation results with 95% confidence intervals for bipolar seesaw model output versus reference record comparisons. Optimal *r* values are given for the reported lags and lag values are rounded to the closest unit. The 95% confidence intervals (CI) with the 2.5th and 97.5th percentiles are derived from 1,000 Monte Carlo iterations (*Materials and Methods*). "Short window" and "Long window" refer to band-pass filtering with a 500- to 10,000-y window and 500- to 16,000-y window, respectively. Opposite values of the IVC benthic foraminiferal $\delta^{18}O$ record are used when comparing with bipolar seesaw model outputs from biomarker-based SST records. See Figs. S16 and S18 for the full curves. AA, Antarctic stack of EDC, EDML, and WD; and BSO, bipolar seesaw output.

		Short window						Long window					
		Optimal Pearson *r*			Lag (y)			Optimal Pearson *r*			Lag (y)		
Comparison	Period	Value	95% CI		Value	95% CI		Value	95% CI		Value	95% CI	
BSO NGRIP T_{air}	115 to 12 ka BP	0.61	0.59	0.62	–270	–290	–260	0.60	0.59	0.61	–300	–310	–290
vs	43 to 12 ka BP	0.65	0.63	0.67	–170	–190	–160	0.59	0.56	0.60	–180	–200	–170
AA $\delta^{18}O_{ice}$ stack	115 to 45 ka BP	0.62	0.60	0.63	–380	–400	–360	0.63	0.61	0.64	–420	–440	–400
BSO NGRIP $\delta^{18}O_{ice}$	115 to 12 ka BP	0.66	0.64	0.67	–290	–310	–280	0.65	0.63	0.66	–340	–360	–320
vs	43 to 12 ka BP	0.71	0.67	0.73	–200	–210	–180	0.63	0.60	0.65	–190	–200	–170
AA $\delta^{18}O_{ice}$ stack	115 to 45 ka BP	0.67	0.64	0.68	–380	–400	–350	0.68	0.66	0.69	–490	–520	–450
BSO MD95-2042 $U^{K'}_{37}$	115 to 12 ka BP	0.61	0.58	0.62	–140	–160	–110	0.63	0.60	0.64	–190	–220	–160
vs	43 to 12 ka BP	0.77	0.74	0.78	0	0	20	0.63	0.60	0.65	0	0	0
AA $\delta^{18}O_{ice}$ stack	115 to 45 ka BP	0.58	0.55	0.60	–290	–340	–240	0.66	0.62	0.67	–380	–430	–330
BSO MD95-2042 RI-OH′	115 to 12 ka BP	0.67	0.65	0.68	–220	–230	–200	0.70	0.69	0.71	–260	–280	–250
vs	43 to 12 ka BP	0.79	0.77	0.79	–60	–70	–40	0.69	0.67	0.70	–30	–50	–20
AA $\delta^{18}O_{ice}$ stack	115 to 45 ka BP	0.65	0.62	0.66	–390	–420	–360	0.75	0.73	0.75	–480	–510	–450
BSO MD95-2042 $U^{K'}_{37}$	115 to 12 ka BP	0.55	0.39	0.52	–410	–540	–300	0.60	0.46	0.57	–590	–770	–440
vs	43 to 12 ka BP	0.46	0.29	0.49	–310	–1,120	–120	0.51	0.38	0.54	–1,240	–1,770	–320
MD95-2042 IVC $\delta^{18}O$ benthic	115 to 45 ka BP	0.58	0.40	0.56	–440	–580	–310	0.63	0.48	0.60	–560	–740	–420
BSO MD95-2042 RI-OH′	115 to 12 ka BP	0.59	0.43	0.55	–500	–610	–410	0.63	0.49	0.59	–640	–790	–530
vs	43 to 12 ka BP	0.49	0.31	0.51	–390	–590	–260	0.47	0.37	0.51	–540	–1,960	–380
MD95-2042 IVC $\delta^{18}O$ benthic	115 to 45 ka BP	0.63	0.46	0.59	–530	–650	–420	0.69	0.53	0.65	–640	–790	–520
BSO MD95-2042 IVC $\delta^{18}O$ *G. bulloides*	115 to 12 ka BP	0.54	0.38	0.50	–490	–610	–380	0.55	0.42	0.53	–610	–800	–470
vs	43 to 12 ka BP	0.34	0.24	0.40	–410	–1,990	–270	0.51	0.37	0.53	–1,970	–2,000	–1,620
MD95-2042 IVC $\delta^{18}O$ benthic	115 to 45 ka BP	0.58	0.40	0.55	–500	–660	–370	0.61	0.45	0.59	–580	–750	–440

Table S19. Monte Carlo results for cross-correlation comparisons between different bipolar seesaw model outputs. Each column indicates the 2.5th and 97.5th percentiles that define 95% confidence intervals—lag differences are rounded to the closest unit. Negative differences in optimal *r* values and lags indicate stronger optimal cross-correlations and reduced lags or increased leads relative to the Southern Hemisphere reference record when switching from T_{air} to $\delta^{18}O_{ice}$ for Greenland, when switching from $U^{K'}_{37}$ to RI-OH′ and from the ice-volume–corrected (IVC) foraminiferal-based record to biomarker-based paleothermometric records for the Iberian Margin, and when switching from Greenland paleothermometric records to Iberian Margin paleothermometric records as bipolar seesaw inputs. "Short window" and "Long window" refer to band-pass filtering with a 500- to 10,000-y window and 500- to 16,000-y window, respectively. Opposite values of the IVC benthic foraminiferal $\delta^{18}O$ record are used when comparing with bipolar seesaw model outputs from biomarker-based SST records. Non-significant differences are shown with grey numbers in italics. AA, Antarctic stack of EDC, EDML, and WD; and BSO, bipolar seesaw output.

			Short window				Long window			
Reference	Comparison	Period	Optimal Pearson *r*		Lag (y)		Optimal Pearson *r*		Lag (y)	
AA $\delta^{18}O_{ice}$ stack	BSO NGRIP T_{air}	115 to 12 ka BP	–0.07	–0.04	0	30	–0.06	–0.03	20	60
	vs	43 to 12 ka BP	–0.09	–0.02	10	40	–0.08	–0.01	*–10*	*20*
	BSO NGRIP $\delta^{18}O_{ice}$	115 to 45 ka BP	–0.06	–0.03	*–20*	*20*	–0.06	–0.03	40	100
	BSO MD95-2042 $U^{K'}_{37}$	115 to 12 ka BP	–0.09	–0.05	50	110	–0.09	–0.06	40	100
	vs	43 to 12 ka BP	–0.04	–0.01	40	80	–0.07	–0.04	20	50
	BSO MD95-2042 RI-OH′	115 to 45 ka BP	–0.09	–0.04	50	150	–0.12	–0.07	40	140
	BSO NGRIP T_{air}	115 to 12 ka BP	*–0.01*	*0.03*	–170	–110	–0.04	< –0.01	–140	–80
	vs	43 to 12 ka BP	–0.14	–0.09	–190	–160	–0.07	–0.02	–200	–170
	BSO MD95-2042 $U^{K'}_{37}$	115 to 45 ka BP	0.02	0.07	–140	–40	*–0.05*	*< 0.01*	*–90*	*20*
	BSO NGRIP T_{air}	115 to 12 ka BP	–0.08	–0.05	–70	–40	–0.11	–0.08	–50	–20
	vs	43 to 12 ka BP	–0.15	–0.11	–130	–100	–0.12	–0.08	–170	–130
	BSO MD95-2042 RI-OH′	115 to 45 ka BP	–0.04	–0.01	*–20*	*40*	–0.13	–0.10	30	90
	BSO NGRIP $\delta^{18}O_{ice}$	115 to 12 ka BP	0.04	0.08	–180	–130	< 0.01	0.05	–180	–120
	vs	43 to 12 ka BP	–0.09	–0.03	–220	–180	–0.03	0.03	–210	–170
	BSO MD95-2042 $U^{K'}_{37}$	115 to 45 ka BP	0.06	0.12	–140	–40	*< –0.01*	*0.05*	–160	–50
	BSO NGRIP $\delta^{18}O_{ice}$	115 to 12 ka BP	*–0.03*	*0.01*	–90	–50	–0.06	–0.03	–100	–50
	vs	43 to 12 ka BP	–0.11	–0.05	–160	–120	–0.08	–0.03	–170	–130
	BSO MD95-2042 RI-OH′	115 to 45 ka BP	0.01	0.04	*–20*	*40*	–0.08	–0.05	*–50*	*30*
MD95-2042 IVC $\delta^{18}O$ benthic	BSO MD95-2042 $U^{K'}_{37}$	115 to 12 ka BP	–0.06	< –0.01	20	150	–0.05	–0.01	*–30*	*140*
	vs	43 to 12 ka BP	*–0.06*	*0.02*	*–530*	*180*	*–0.01*	*0.05*	*–960*	*640*
	BSO MD95-2042 RI-OH′	115 to 45 ka BP	–0.07	–0.01	10	160	–0.08	–0.03	*–10*	*150*
	BSO MD95-2042 IVC $\delta^{18}O$ *G. bulloides*	115 to 12 ka BP	*–0.05*	*0.03*	*–180*	*20*	*–0.07*	*< 0.01*	*–170*	*120*
	vs	43 to 12 ka BP	*–0.14*	*0.02*	*–1,720*	*40*	*–0.09*	*0.06*	–1,660	–200
	BSO MD95-2042 $U^{K'}_{37}$	115 to 45 ka BP	*–0.05*	*0.05*	*–170*	*40*	*–0.06*	*0.04*	*–140*	*110*
	BSO MD95-2042 IVC $\delta^{18}O$ *G. bulloides*	115 to 12 ka BP	–0.08	< –0.01	*–80*	*90*	–0.10	–0.04	*–100*	*130*
	vs	43 to 12 ka BP	*–0.17*	*< 0.01*	*–1,610*	*80*	*–0.08*	*0.08*	–1,600	–30
	BSO MD95-2042 RI-OH′	115 to 45 ka BP	–0.09	< –0.01	*–70*	*120*	–0.11	–0.02	*–40*	*160*

SI References

1. W. Dansgaard, *et al.*, Evidence for general instability of past climate from a 250-kyr ice-core record. *Nature* **364**, 218–220 (1993).
2. W. Dansgaard, J. W. C. White, S. J. Johnsen, The abrupt termination of the Younger Dryas climate event. *Nature* **339**, 532–534 (1989).
3. S. J. Johnsen, *et al.*, Irregular glacial interstadials recorded in a new Greenland ice core. *Nature* **359**, 311–313 (1992).
4. P. M. Grootes, M. Stuiver, J. W. C. White, S. Johnsen, J. Jouzel, Comparison of oxygen isotope records from the GISP2 and GRIP Greenland ice cores. *Nature* **366**, 552–554 (1993).
5. G. C. Bond, *et al.*, Correlations between climate records from North Atlantic sediments and Greenland ice. *Nature* **365**, 143–147 (1993).
6. H. Heinrich, Origin and consequences of cyclic ice rafting in the Northeast Atlantic Ocean during the past 130,000 years. *Quaternary Research* **29**, 142–152 (1988).
7. E. Bard, *et al.*, Retreat velocity of the North Atlantic polar front during the last deglaciation determined by ^{14}C accelerator mass spectrometry. *Nature* **328**, 791–794 (1987).
8. W. F. Ruddiman, A. McIntyre, The North Atlantic Ocean during the last deglaciation. *Palaeogeography, Palaeoclimatology, Palaeoecology* **35**, 145–214 (1981).
9. E. Bard, *et al.*, Sea-level estimates during the last deglaciation based on $\delta^{18}O$ and accelerator mass spectrometry ^{14}C ages measured in *Globigerina bulloides*. *Quaternary Research* **31**, 381–391 (1989).
10. O. Cayre, Y. Lancelot, E. Vincent, M. A. Hall, Paleoceanographic reconstructions from planktonic foraminifera off the Iberian Margin: temperature, salinity, and Heinrich events. *Paleoceanography* **14**, 384–396 (1999).
11. E. Bard, F. Rostek, J.-L. Turon, S. Gendreau, Hydrological impact of Heinrich events in the subtropical northeast Atlantic. *Science* **289**, 1321–1324 (2000).
12. E. Bard, Comparison of alkenone estimates with other paleotemperature proxies. *Geochemistry, Geophysics, Geosystems* **2**, 2000GC000050 (2001).
13. M. F. Sánchez Goñi, E. Bard, A. Landais, L. Rossignol, F. d'Errico, Air–sea temperature decoupling in western Europe during the last interglacial–glacial transition. *Nature Geosci* **6**, 837–841 (2013).
14. G. H. Denton, S. Toucanne, A. E. Putnam, D. J. A. Barrell, J. L. Russell, Heinrich summers. *Quaternary Science Reviews* **295**, 107750 (2022).
15. N. J. Shackleton, M. A. Hall, E. Vincent, Phase relationships between millennial-scale events 64,000–24,000 years ago. *Paleoceanography* **15**, 565–569 (2000).
16. D. Pailler, E. Bard, High frequency palaeoceanographic changes during the past 140 000 yr recorded by the organic matter in sediments of the Iberian Margin. *Palaeogeography, Palaeoclimatology, Palaeoecology* **181**, 431–452 (2002).
17. B. Martrat, *et al.*, Four climate cycles of recurring deep and surface water destabilizations on the Iberian Margin. *Science* **317**, 502–507 (2007).
18. G. M. Patton, P. A. Martin, A. Voelker, E. Salgueiro, Multiproxy comparison of oceanographic temperature during Heinrich Events in the eastern subtropical Atlantic. *Earth and Planetary Science Letters* **310**, 45–58 (2011).
19. S. Darfeuil, *et al.*, Sea surface temperature reconstructions over the last 70 kyr off Portugal: biomarker data and regional modeling. *Paleoceanography* **31**, 40–65 (2016).
20. D. A. Hodell, *et al.*, The "Shackleton Site" (IODP Site U1385) on the Iberian Margin. *Scientific Drilling* **16**, 13–19 (2013).
21. N. Davtian, E. Bard, S. Darfeuil, G. Ménot, F. Rostek, The novel hydroxylated tetraether index RI-OH′ as a sea surface temperature proxy for the 160-45 ka BP period off the Iberian Margin. *Paleoceanography and Paleoclimatology* **36**, e2020PA004077 (2021).
22. J. C. Duplessy, E. Bard, L. Labeyrie, J. Duprat, J. Moyes, Oxygen isotope records and salinity changes in the northeastern Atlantic Ocean during the last 18,000 years. *Paleoceanography* **8**, 341–350 (1993).
23. S. Fietz, S. L. Ho, C. Huguet, Archaeal membrane lipid-based paleothermometry for applications in polar oceans. *Oceanog* **33**, 104–114 (2020).
24. X. Lü, *et al.*, Hydroxylated isoprenoid GDGTs in Chinese coastal seas and their potential as a paleotemperature proxy for mid-to-low latitude marginal seas. *Organic Geochemistry* **89–90**, 31–43 (2015).

25. J. E. Tierney, M. P. Tingley, A Bayesian, spatially-varying calibration model for the TEX_{86} proxy. *Geochimica et Cosmochimica Acta* **127**, 83–106 (2014).
26. J. E. Tierney, M. P. Tingley, A TEX_{86} surface sediment database and extended Bayesian calibration. *Scientific Data* **2**, 150029 (2015).
27. M. H. Conte, *et al.*, Global temperature calibration of the alkenone unsaturation index ($U^{K'}_{37}$) in surface waters and comparison with surface sediments. *Geochemistry, Geophysics, Geosystems* **7**, Q02005 (2006).
28. J. E. Tierney, M. P. Tingley, BAYSPLINE: a new calibration for the alkenone paleothermometer. *Paleoceanography and Paleoclimatology* **33**, 281–301 (2018).
29. F. Eynaud, J. L. Turon, M. F. Sánchez-Goñi, S. Gendreau, Dinoflagellate cyst evidence of 'Heinrich-like events' off Portugal during the Marine Isotopic Stage 5. *Marine Micropaleontology* **40**, 9–21 (2000).
30. L. Morcillo-Montalbá, *et al.*, Rapid climate changes in the westernmost Mediterranean (Alboran Sea) over the last 35 kyr: new insights from four lipid paleothermometers ($U^{K'}_{37}$, TEX_{86}^{H}, RI-OH′, and LDI). *Paleoceanography and Paleoclimatology* **36**, e2020PA004171 (2021).
31. T. F. Stocker, S. J. Johnsen, A minimum thermodynamic model for the bipolar seesaw. *Paleoceanography* **18**, 1087 (2003).
32. F. G. Prahl, S. G. Wakeham, Calibration of unsaturation patterns in long-chain ketone compositions for palaeotemperature assessment. *Nature* **330**, 367–369 (1987).
33. I. T. Marlowe, S. C. Brassell, G. Eglinton, J. C. Green, Long chain unsaturated ketones and esters in living algae and marine sediments. *Organic Geochemistry* **6**, 135–141 (1984).
34. J. K. Volkman, G. Eglinton, E. D. S. Corner, T. E. V. Forsberg, Long-chain alkenes and alkenones in the marine coccolithophorid *Emiliania huxleyi*. *Phytochemistry* **19**, 2619–2622 (1980).
35. J. K. Volkman, S. M. Barrerr, S. I. Blackburn, E. L. Sikes, Alkenones in *Gephyrocapsa oceanica*: implications for studies of paleoclimate. *Geochimica et Cosmochimica Acta* **59**, 513–520 (1995).
36. P. J. Müller, G. Kirst, G. Ruhland, I. von Storch, A. Rosell-Melé, Calibration of the alkenone paleotemperature index $U^{K'}_{37}$ based on core-tops from the eastern South Atlantic and the global ocean (60°N-60°S). *Geochimica et Cosmochimica Acta* **62**, 1757–1772 (1998).
37. F. G. Prahl, L. A. Muehlhausen, D. L. Zahnle, Further evaluation of long-chain alkenones as indicators of paleoceanographic conditions. *Geochimica et Cosmochimica Acta* **52**, 2303–2310 (1988).
38. X.-L. Liu, *et al.*, Mono- and dihydroxyl glycerol dibiphytanyl glycerol tetraethers in marine sediments: identification of both core and intact polar lipid forms. *Geochimica et Cosmochimica Acta* **89**, 102–115 (2012).
39. J. S. Sinninghe Damsté, *et al.*, Intact polar and core glycerol dibiphytanyl glycerol tetraether lipids of Group I.1a and I.1b *Thaumarchaeota* in soil. *Applied and Environmental Microbiology* **78**, 6866–6874 (2012).
40. F. J. Elling, *et al.*, Effects of growth phase on the membrane lipid composition of the thaumarchaeon *Nitrosopumilus maritimus* and their implications for archaeal lipid distributions in the marine environment. *Geochimica et Cosmochimica Acta* **141**, 579–597 (2014).
41. F. J. Elling, M. Könneke, M. Mußmann, A. Greve, K.-U. Hinrichs, Influence of temperature, pH, and salinity on membrane lipid composition and TEX_{86} of marine planktonic thaumarchaeal isolates. *Geochimica et Cosmochimica Acta* **171**, 238–255 (2015).
42. F. J. Elling, *et al.*, Chemotaxonomic characterisation of the thaumarchaeal lipidome. *Environmental Microbiology* **19**, 2681–2700 (2017).
43. M. Sollai, L. Villanueva, E. C. Hopmans, G.-J. Reichart, J. S. Sinninghe Damsté, A combined lipidomic and 16S rRNA gene amplicon sequencing approach reveals archaeal sources of intact polar lipids in the stratified Black Sea water column. *Geobiology* **17**, 91–109 (2019).
44. Y. Xu, *et al.*, Intact ether lipids in trench sediments related to archaeal community and environmental conditions in the deepest ocean. *Journal of Geophysical Research: Biogeosciences* **125**, e2019JG005431 (2020).
45. J. S. Sinninghe Damsté, Y. Weber, J. Zopfi, M. F. Lehmann, H. Niemann, Distributions and sources of isoprenoidal GDGTs in Lake Lugano and other central European (peri-)alpine lakes: Lessons for their use as paleotemperature proxies. *Quaternary Science Reviews* **277**, 107352 (2022).
46. J. S. Sinninghe Damsté, L. A. Warden, C. Berg, K. Jürgens, M. Moros, Evaluation of the distributions of hydroxylated glycerol dibiphytanyl glycerol tetraethers (GDGTs) in Holocene Baltic Sea sediments for reconstruction of sea surface temperature: the effect of changing salinity. *Climate of the Past* **18**, 2271–2288 (2022).

47. N. Lamping, *et al.*, Evaluation of lipid biomarkers as proxies for sea ice and ocean temperatures along the Antarctic continental margin. *Climate of the Past* **17**, 2305–2326 (2021).
48. R. Liu, *et al.*, Distribution and source of glycerol dialkyl glycerol tetraethers (GDGTs) and the applicability of GDGT-based temperature proxies in surface sediments of Prydz Bay, East Antarctica. *Polar Research* **39**, 3557 (2020).
49. S. Schouten, E. C. Hopmans, E. Schefuß, J. S. Sinninghe Damsté, Distributional variations in marine crenarchaeotal membrane lipids: a new tool for reconstructing ancient sea water temperatures? *Earth and Planetary Science Letters* **204**, 265–274 (2002).
50. S. Schouten, E. C. Hopmans, J. S. Sinninghe Damsté, The organic geochemistry of glycerol dialkyl glycerol tetraether lipids: a review. *Organic Geochemistry* **54**, 19–61 (2013).
51. Z. Zeng, *et al.*, GDGT cyclization proteins identify the dominant archaeal sources of tetraether lipids in the ocean. *PNAS* **116**, 22505–22511 (2019).
52. M. A. Besseling, *et al.*, The absence of intact polar lipid-derived GDGTs in marine waters dominated by Marine Group II: implications for lipid biosynthesis in Archaea. *Sci Rep* **10**, 294 (2020).
53. J.-H. Kim, S. Schouten, E. C. Hopmans, B. Donner, J. S. Sinninghe Damsté, Global sediment core-top calibration of the TEX_{86} paleothermometer in the ocean. *Geochimica et Cosmochimica Acta* **72**, 1154–1173 (2008).
54. J.-H. Kim, *et al.*, New indices and calibrations derived from the distribution of crenarchaeal isoprenoid tetraether lipids: implications for past sea surface temperature reconstructions. *Geochimica et Cosmochimica Acta* **74**, 4639–4654 (2010).
55. S. Schouten, A. Forster, F. E. Panoto, J. S. Sinninghe Damsté, Towards calibration of the TEX_{86} palaeothermometer for tropical sea surface temperatures in ancient greenhouse worlds. *Organic Geochemistry* **38**, 1537–1546 (2007).
56. C. Wuchter, S. Schouten, M. J. L. Coolen, J. S. Sinninghe Damsté, Temperature-dependent variation in the distribution of tetraether membrane lipids of marine *Crenarchaeota*: implications for TEX_{86} paleothermometry. *Paleoceanography* **19**, PA4028 (2004).
57. M.-E. Vorrath, *et al.*, Sea ice dynamics in the Bransfield Strait, Antarctic Peninsula, during the past 240 years: a multi-proxy intercomparison study. *Climate of the Past* **16**, 2459–2483 (2020).
58. X. E. Ai, *et al.*, Southern Ocean upwelling, Earth's obliquity, and glacial-interglacial atmospheric CO_2 change. *Science* **370**, 1348–1352 (2020).
59. H. J. Anderson, J. B. Pedro, H. C. Bostock, Z. Chase, T. L. Noble, Compiled Southern Ocean sea surface temperatures correlate with Antarctic Isotope Maxima. *Quaternary Science Reviews* **255**, 106821 (2021).
60. T. A. Mashiotta, D. W. Lea, H. J. Spero, Glacial–interglacial changes in Subantarctic sea surface temperature and $\delta^{18}O$-water using foraminiferal Mg. *Earth and Planetary Science Letters* **170**, 417–432 (1999).
61. G. Cortese, A. Abelmann, Radiolarian-based paleotemperatures during the last 160 kyr at ODP Site 1089 (Southern Ocean, Atlantic Sector). *Palaeogeography, Palaeoclimatology, Palaeoecology* **182**, 259–286 (2002).
62. R. A. Lopes dos Santos, D. Wilkins, P. De Deckker, S. Schouten, Late Quaternary productivity changes from offshore Southeastern Australia: A biomarker approach. *Palaeogeography, Palaeoclimatology, Palaeoecology* **363–364**, 48–56 (2012).
63. X. Crosta, A. Sturm, L. Armand, J.-J. Pichon, Late Quaternary sea ice history in the Indian sector of the Southern Ocean as recorded by diatom assemblages. *Marine Micropaleontology* **50**, 209–223 (2004).
64. K. Pahnke, R. Zahn, H. Elderfield, M. Schulz, 340,000-year centennial-scale marine record of Southern Hemisphere climatic oscillation. *Science* **301**, 948–952 (2003).
65. K. Pahnke, J. P. Sachs, Sea surface temperatures of southern midlatitudes 0–160 kyr B.P. *Paleoceanography* **21** (2006).
66. T. J. Heaton, *et al.*, Marine20—The marine radiocarbon age calibration curve (0–55,000 cal BP). *Radiocarbon* **62**, 779–820 (2020).
67. T. J. Heaton, *et al.*, Marine radiocarbon calibration in polar regions: a simple approximate approach using Marine20 (2022) (October 19, 2022).
68. D. Veres, *et al.*, The Antarctic ice core chronology (AICC2012): an optimized multi-parameter and multi-site dating approach for the last 120 thousand years. *Climate of the Past* **9**, 1733–1748 (2013).
69. L. Bazin, *et al.*, An optimized multi-proxy, multi-site Antarctic ice and gas orbital chronology (AICC2012): 120–800 ka. *Climate of the Past* **9**, 1715–1731 (2013).

70. J. Jouzel, *et al.*, Orbital and millennial Antarctic climate variability over the past 800,000 years. *Science* **317**, 793–796 (2007).
71. F. Parrenin, *et al.*, Synchronous change of atmospheric CO_2 and Antarctic temperature during the last deglacial warming. *Science* **339**, 1060–1063 (2013).
72. E. L. Sikes, J. K. Volkman, Calibration of alkenone unsaturation ratios ($U^{K'}_{37}$) for paleotemperature estimation in cold polar waters. *Geochimica et Cosmochimica Acta* **57**, 1883–1889 (1993).
73. H. Elderfield, G. Ganssen, Past temperature and $\delta^{18}O$ of surface ocean waters inferred from foraminiferal Mg/Ca ratios. *Nature* **405**, 442–445 (2000).
74. J. E. Tierney, S. B. Malevich, W. Gray, L. Vetter, K. Thirumalai, Bayesian calibration of the Mg/Ca paleothermometer in planktic foraminifera. *Paleoceanography and Paleoclimatology* **34**, 2005–2030 (2019).
75. E. Park, *et al.*, Seasonality of archaeal lipid flux and GDGT-based thermometry in sinking particles of high-latitude oceans: Fram Strait (79° N) and Antarctic Polar Front (50° S). *Biogeosciences* **16**, 2247–2268 (2019).
76. A. Pearson, A. E. Ingalls, Assessing the use of archaeal lipids as marine environmental proxies. *Annual Review of Earth and Planetary Sciences* **41**, 359–384 (2013).
77. S. L. Ho, *et al.*, Appraisal of TEX_{86} and TEX_{86}^{L} thermometries in subpolar and polar regions. *Geochimica et Cosmochimica Acta* **131**, 213–226 (2014).
78. Y.-H. Park, *et al.*, Distribution, source and transportation of glycerol dialkyl glycerol tetraethers in surface sediments from the western Arctic Ocean and the northern Bering Sea. *Marine Chemistry* **165**, 10–24 (2014).
79. S. Fietz, S. L. Ho, C. Huguet, A. Rosell-Melé, A. Martínez-García, Appraising GDGT-based seawater temperature indices in the Southern Ocean. *Organic Geochemistry* **102**, 93–105 (2016).
80. D. Chandler, P. Langebroek, Southern Ocean sea surface temperature synthesis: Part 1. Evaluation of temperature proxies at glacial-interglacial time scales. *Quaternary Science Reviews* **271**, 107191 (2021).
81. EPICA Community Members, One-to-one coupling of glacial climate variability in Greenland and Antarctica. *Nature* **444**, 195–198 (2006).
82. E. Capron, *et al.*, Synchronising EDML and NorthGRIP ice cores using $\delta^{18}O$ of atmospheric oxygen ($\delta^{18}O_{atm}$) and CH_4 measurements over MIS 5 (80–123 kyr). *Quaternary Science Reviews* **29**, 222–234 (2010).
83. E. Capron, *et al.*, Millennial and sub-millennial scale climatic variations recorded in polar ice cores over the last glacial period. *Climate of the Past* **6**, 345–365 (2010).
84. P. Zheng, J. B. Pedro, M. Jochum, S. O. Rasmussen, Z. Lai, Different trends in Antarctic temperature and atmospheric CO_2 during the last glacial. *Geophysical Research Letters* **48**, e2021GL093868 (2021).
85. T. F. Stocker, *Introduction to Climate Modelling* (University of Bern, 2022), pp. 1–209, https://climatehomes.unibe.ch/~stocker/stocker22icm.pdf.
86. P. Braconnot, *et al.*, Evaluation of climate models using palaeoclimatic data. *Nature Climate Change* **2**, 417–424 (2012).
87. K. Izumi, P. J. Bartlein, S. P. Harrison, Consistent large-scale temperature responses in warm and cold climates. *Geophysical Research Letters* **40**, 1817–1823 (2013).
88. G. A. Schmidt, *et al.*, Using palaeo-climate comparisons to constrain future projections in CMIP5. *Clim. Past* **10**, 221–250 (2014).
89. S. P. Harrison, P. J. Bartlein, I. C. Prentice, What have we learnt from palaeoclimate simulations? *Journal of Quaternary Science* **31**, 363–385 (2016).
90. V. Masson-Delmotte, *et al.*, Past and future polar amplification of climate change: climate model intercomparisons and ice-core constraints. *Clim Dyn* **26**, 513–529 (2006).
91. V. Masson-Delmotte, *et al.*, Past and future polar amplification of climate change: climate model intercomparisons and ice-core constraints. *Clim Dyn* **27**, 437–440 (2006).
92. M. H. Conte, A. Thompson, D. Lesley, R. P. Harris, Genetic and physiological influences on the alkenone/alkenoate versus growth temperature relationship in *Emiliania huxleyi* and *Gephyrocapsa Oceanica*. *Geochimica et Cosmochimica Acta* **62**, 51–68 (1998).
93. M.-A. Sicre, E. Bard, U. Ezat, F. Rostek, Alkenone distributions in the North Atlantic and Nordic sea surface waters. *Geochemistry, Geophysics, Geosystems* **3**, 2001GC000159 (2002).
94. L. Sanchi, G. Ménot, E. Bard, An automated purification method for archaeal and bacterial tetraethers in soils and sediments. *Organic Geochemistry* **54**, 83–90 (2013).

95. P. Kindler, *et al.*, Temperature reconstruction from 10 to 120 kyr b2k from the NGRIP ice core. *Climate of the Past* **10**, 887–902 (2014).
96. C. Buizert, *et al.*, Antarctic surface temperature and elevation during the Last Glacial Maximum. *Science* **372**, 1097–1101 (2021).
97. B. R. Markle, E. J. Steig, Improving temperature reconstructions from ice-core water-isotope records. *Climate of the Past* **18**, 1321–1368 (2022).
98. B. Stenni, *et al.*, The deuterium excess records of EPICA Dome C and Dronning Maud Land ice cores (East Antarctica). *Quaternary Science Reviews* **29**, 146–159 (2010).
99. C. Buizert, *et al.*, The WAIS Divide deep ice core WD2014 chronology – Part 1: methane synchronization (68–31 ka BP) and the gas age–ice age difference. *Climate of the Past* **11**, 153–173 (2015).
100. WAIS Divide Project Members, Precise interpolar phasing of abrupt climate change during the last ice age. *Nature* **520**, 661–665 (2015).
101. A. Svensson, *et al.*, Bipolar volcanic synchronization of abrupt climate change in Greenland and Antarctic ice cores during the last glacial period. *Climate of the Past* **16**, 1565–1580 (2020).
102. M. Sigl, *et al.*, The WAIS Divide deep ice core WD2014 chronology – Part 2: annual-layer counting (0–31 ka BP). *Climate of the Past* **12**, 769–786 (2016).
103. K. K. Andersen, *et al.*, The Greenland Ice Core Chronology 2005, 15–42 ka. Part 1: constructing the time scale. *Quaternary Science Reviews* **25**, 3246–3257 (2006).
104. A. Svensson, *et al.*, A 60 000 year Greenland stratigraphic ice core chronology. *Clim. Past* **4**, 47–57 (2008).
105. S. O. Rasmussen, *et al.*, A new Greenland ice core chronology for the last glacial termination. *Journal of Geophysical Research: Atmospheres* **111**, D06102 (2006).
106. B. M. Vinther, *et al.*, A synchronized dating of three Greenland ice cores throughout the Holocene. *Journal of Geophysical Research: Atmospheres* **111** (2006).
107. H. Cheng, *et al.*, The Asian monsoon over the past 640,000 years and ice age terminations. *Nature* **534**, 640–646 (2016).
108. M. Groen, M. Storey, An astronomically calibrated $^{40}Ar/^{39}Ar$ age for the North Atlantic Z2 Ash: implications for the Greenland ice core timescale. *Quaternary Science Reviews* **293**, 107526 (2022).
109. E. Bard, G. Ménot-Combes, F. Rostek, Present status of radiocarbon calibration and comparison records based on Polynesian corals and Iberian margin sediments. *Radiocarbon* **46**, 1189–1202 (2004).
110. N. J. Shackleton, R. G. Fairbanks, T. Chiu, F. Parrenin, Absolute calibration of the Greenland time scale: implications for Antarctic time scales and for $\Delta^{14}C$. *Quaternary Science Reviews* **23**, 1513–1522 (2004).
111. E. Bard, *et al.*, Radiocarbon calibration/comparison records based on marine sediments from the Pakistan and Iberian Margins. *Radiocarbon* **55**, 1999–2019 (2013).
112. J. V. Stern, L. E. Lisiecki, North Atlantic circulation and reservoir age changes over the past 41,000 years. *Geophysical Research Letters* **40**, 3693–3697 (2013).
113. C. Waelbroeck, *et al.*, The timing of the last deglaciation in North Atlantic climate records. *Nature* **412**, 724–727 (2001).
114. L. C. Skinner, *et al.*, Atlantic Ocean ventilation changes across the last deglaciation and their carbon cycle implications. *Paleoceanography and Paleoclimatology* **36**, e2020PA004074 (2021).
115. A. Govin, *et al.*, Terrigenous input off northern South America driven by changes in Amazonian climate and the North Brazil Current retroflection during the last 250 ka. *Climate of the Past* **10**, 843–862 (2014).
116. A. Govin, *et al.*, Sequence of events from the onset to the demise of the Last Interglacial: evaluating strengths and limitations of chronologies used in climatic archives. *Quaternary Science Reviews* **129**, 1–36 (2015).
117. T. Extier, *et al.*, On the use of $\delta^{18}O_{atm}$ for ice core dating. *Quaternary Science Reviews* **185**, 244–257 (2018).
118. G. E. Moseley, *et al.*, NALPS19: sub-orbital-scale climate variability recorded in northern Alpine speleothems during the last glacial period. *Climate of the Past* **16**, 29–50 (2020).
119. M. J. Kelly, “Characterization of Asian Monsoon variability since the Penultimate Interglacial on orbital and sub-orbital timescales, Dongge Cave, China,” University of Minnesota, USA. (2010).
120. D. Yuan, *et al.*, Timing, duration, and transitions of the Last Interglacial Asian Monsoon. *Science* **304**, 575–578 (2004).

121. M. J. Kelly, *et al.*, High resolution characterization of the Asian Monsoon between 146,000 and 99,000 years B.P. from Dongge Cave, China and global correlation of events surrounding Termination II. *Palaeogeography, Palaeoclimatology, Palaeoecology* **236**, 20–38 (2006).
122. Y. Wang, *et al.*, Millennial- and orbital-scale changes in the East Asian monsoon over the past 224,000 years. *Nature* **451**, 1090–1093 (2008).
123. C. Buizert, *et al.*, Abrupt ice-age shifts in southern westerly winds and Antarctic climate forced from the north. *Nature* **563**, 681–685 (2018).
124. J. B. Pedro, *et al.*, Beyond the bipolar seesaw: toward a process understanding of interhemispheric coupling. *Quaternary Science Reviews* **192**, 27–46 (2018).
125. M. Rivoire, J.-L. Ferrier, *Cours d'automatique, Tome 1 : Traitement du signal - Systèmes* (Eyrolles, 1992).
126. North Greenland Ice Core Project members, High-resolution record of Northern Hemisphere climate extending into the last interglacial period. *Nature* **431**, 147–151 (2004).
127. M. Baumgartner, *et al.*, NGRIP CH_4 concentration from 120 to 10 kyr before present and its relation to a $\delta^{15}N$ temperature reconstruction from the same ice core. *Climate of the Past* **10**, 903–920 (2014).
128. J. Jouzel, *et al.*, Validity of the temperature reconstruction from water isotopes in ice cores. *Journal of Geophysical Research: Oceans* **102**, 26471–26487 (1997).
129. K. M. Cuffey, *et al.*, Large Arctic temperature change at the Wisconsin-Holocene glacial transition. *Science* **270**, 455–458 (1995).
130. D. Dahl-Jensen, *et al.*, Past temperatures directly from the Greenland ice sheet. *Science* **282**, 268–271 (1998).
131. T. Kobashi, *et al.*, Volcanic influence on centennial to millennial Holocene Greenland temperature change. *Scientific Reports* **7**, 1441 (2017).
132. W. Ebisuzaki, A method to estimate the statistical significance of a correlation when the data are serially correlated. *J. Climate* **10**, 2147–2153 (1997).
133. EPICA Community Members, Eight glacial cycles from an Antarctic ice core. *Nature* **429**, 623–628 (2004).
134. E. J. Steig, *et al.*, Recent climate and ice-sheet changes in West Antarctica compared with the past 2,000 years. *Nature Geosci* **6**, 372–375 (2013).
135. WAIS Divide Project Members, Onset of deglacial warming in West Antarctica driven by local orbital forcing. *Nature* **500**, 440–444 (2013).
136. E. Bard, F. Rostek, G. Ménot-Combes, Radiocarbon calibration beyond 20,000 ^{14}C yr B.P. by means of planktonic foraminifera of the Iberian Margin. *Quaternary Research* **61**, 204–214 (2004).
137. E. Bard, F. Rostek, G. Ménot-Combes, A better radiocarbon clock. *Science* **303**, 178–179 (2004).
138. C. Bronk Ramsey, Bayesian analysis of radiocarbon dates. *Radiocarbon* **51**, 337–360 (2009).
139. C. Bronk Ramsey, OxCal 4.4.2. https://c14.arch.ox.ac.uk/oxcal.html. Accessed 11 September 2020, (2020).